JGR Planets

RESEARCH ARTICLE
10.1029/2021JE007068

The Geophysical Environment of (486958) Arrokoth—A Small Kuiper Belt Object Explored by *New Horizons*

James T. Keane[1], Simon B. Porter[2], Ross A. Beyer[3,4], Orkan M. Umurhan[3,4], William B. McKinnon[5], Jeffrey M. Moore[4], John R. Spencer[2], S. Alan Stern[2], Carver J. Bierson[6], Richard P. Binzel[7], Douglas P. Hamilton[8], Carey M. Lisse[9], Xiaochen Mao[5], Silvia Protopapa[2], Paul M. Schenk[10], Mark R. Showalter[3], John A. Stansberry[11], Oliver L. White[3,4], Anne J. Verbiscer[12], Joel W. Parker[2], Catherine B. Olkin[2], Harold A. Weaver[9], and Kelsi N. Singer[2]

[1]NASA Jet Propulsion Laboratory, California Institute of Technology, Pasadena, CA, USA, [2]Southwest Research Institute, Boulder, CO, USA, [3]SETI Institute, Mountain View, CA, USA, [4]NASA Ames Research Center, Moffett Field, CA, USA, [5]Washington University in St. Louis, Saint Louis, MO, USA, [6]Arizona State University, Tempe, AZ, USA, [7]Massachusetts Institute of Technology, Cambridge, MA, USA, [8]University of Maryland, College Park, College Park, MD, USA, [9]Johns Hopkins University Applied Physics Laboratory, Laurel, MD, USA, [10]Lunar and Planetary Institute, Houston, TX, USA, [11]Space Telescope Science Institute, Baltimore, MD, USA, [12]University of Virginia, Charlottesville, VA, USA

Abstract NASA's *New Horizons* mission performed the first flyby of a small Kuiper Belt Object (KBO), (486958) Arrokoth on 1 January 2019. The fast flyby revealed a fascinating, flattened, contact binary replete with a variety of unexpected geologic terrains. However, the irregular shape and constraints imposed by the fast flyby makes it a challenge to understand these features. Here we use the latest *New Horizons* shape models of Arrokoth to investigate its geophysical environment, including its surface slopes, gravity field, and moments of inertia—which are critical context for understanding Arrokoth's formation, evolution, and peculiar geology. We find that Arrokoth's surface features have a complicated relationship to its geophysical environment. For example, bright material tends to be concentrated in geopotential lows (like the neck), consistent with mass wasting—however, this trend is not consistently observed across Arrokoth. Mass wasting may naturally explain some aspects of Arrokoth's geology, but the actual dynamics of material transport may be complicated owing to Arrokoth's unique shape, spin-rate, and inferred density. While *New Horizons*'s fast and distant flyby precluded directly measuring Arrokoth's mass, we used techniques previously pioneered for comets and asteroids to infer its density. We find that Arrokoth has a low bulk density of $\rho = 235$ kg/m^3 (1σ range: 155–600 kg/m^3). This density is low compared to previously explored small bodies, but is comparable to comets, select binary KBOs, and the ring-moons of Saturn. This low density may be a critical data-point for understanding the formation of planetesimals at the dawn of the Solar System.

Plain Language Summary NASA's *New Horizons* mission performed the first flyby of a small Kuiper Belt Object (KBO), (486958) Arrokoth on 1 January 2019. Arrokoth is a ~30-km long, peanut shaped, icy body in the Kuiper Belt—a reservoir of small bodies left over from the Solar System's formation. Arrokoth is the most distant, and likely the least evolved object, ever explored by a spacecraft. Arrokoth's unusual shape makes it challenging to determine how material moves across its surface. We use the latest shape models to calculate Arrokoth's gravity field. Bright material tends to collect in Arrokoth's lowest locations, perhaps indicating material can move downslope. While *New Horizons* was not able to measure the density of Arrokoth, we are able to infer it using techniques pioneered for studying asteroids and comets. We find that Arrokoth's density is extremely low—more akin to fluffy snow on Earth. If correct, this would be one of the lowest density objects ever explored, closer to the densities of some of the comets and small moons within Saturn's rings. Arrokoth's low density may suggests that the building blocks of planets were assembled very gently in the outer Solar System, in the first few million years of Solar System formation.

Key Points:

- We present new models for the geophysical environment of (486958) Arrokoth based on the latest *New Horizons* shape models
- Many (but not all) of Arrokoth's enigmatic surface markings are correlated with its geophysical environment
- Analysis of Arrokoth's shape suggests that it has a low density of 235 kg/m^3 (1σ range: 155–600 kg/m^3)

Supporting Information:

Supporting Information may be found in the online version of this article.

Correspondence to:

J. T. Keane,
james.t.keane@jpl.nasa.gov

Citation:

Keane, J. T., Porter, S. B., Beyer, R. A., Umurhan, O. M., McKinnon, W. B., Moore, J. M., et al. (2022). The geophysical environment of (486958) Arrokoth—A small Kuiper Belt Object explored by *New Horizons*. *Journal of Geophysical Research: Planets*, *127*, e2021JE007068. https://doi.org/10.1029/2021JE007068

Received 22 SEP 2021
Accepted 13 APR 2022

Author Contributions:

Writing – review & editing: Oliver L. White

1. Introduction

On 1 January 2019, NASA's *New Horizons* spacecraft performed the first flyby of a small Kuiper Belt Object (KBO), (486958) Arrokoth (formerly 2014 MU$_{69}$). Arrokoth is a 36-km long icy body orbiting the Sun at a heliocentric distance of 45 AU (6.6 billion km), making it the most distant, explored object in the Solar System

(Stern et al., 2019). Beyond its sheer distance, Arrokoth is important as it is a member of the so-called Cold Classical KBOs (CCKBOs), characterized by their large orbital distances, non-resonant orbits, low-eccentricities, and low-inclinations (Porter et al., 2018; Stern et al., 2019). CCKBOs are thought to have formed in situ at the dawn of the Solar System, and remained largely unperturbed by dynamical processes in the intervening 4.5 billion years—unlike its resonant compatriots, like Pluto, which migrated tens of AU early in Solar System history (Malhotra, 1993; Nesvorný, 2018). This dynamic stability, coupled with its small size (implying a comparative lack of endogenic activity compared to larger KBOs), makes Arrokoth a potentially pristine "fossil" of Solar System formation, unlike any object explored to date.

The *New Horizons* flyby revealed Arrokoth to be a fascinating contact binary, consisting of two lobes replete with a variety of unusual geologic terrains—including bright and dark terrains, pits, putative craters, lineations, and terrains possibly indicative of tectonics and sublimation (Grundy et al., 2020; McKinnon et al., 2020; Spencer et al., 2020; Stern et al., 2019). In order to understand these geologic features and phenomena, it is critical to understand Arrokoth's geophysical environment. Put simply, it is challenging to develop physically motivated hypotheses when it is not obvious "which way is up." Understanding Arrokoth's shape, moments of inertia, gravity field, rotation, and surface slopes are of primary importance.

In this work, we use the latest *New Horizons* shape models of Arrokoth to investigate its geophysical environment, including its shape, moments of inertia, gravity field, rotation, and surfaces slopes. These physical characteristics control a wide array of geologic phenomena, from mass wasting to tectonics, and promote the physical intuition necessary to understand Arrokoth. This work builds on previous work—including Stern et al. (2019), Spencer et al. (2020), Grundy et al. (2020), and McKinnon et al. (2020)—providing both new and expanded analyses. The paper is organized in eight parts: in Section 2 we present the current Arrokoth shape models and other available geophysical constraints; in Section 3 we summarize the mathematical models and tools used to determine Arrokoth's geophysical environment; in Section 4 we show our results and the derived geophysical model of Arrokoth—including providing tables of bulk properties, and figures of Arrokoth's principal axes of inertia, gravity field, surface slopes, etc.; in Section 5 we compare the derived geophysical model with the observed geology of Arrokoth; in Section 6 we examine how material would move across the surface of Arrokoth in more detail; in Section 7 we detail our methods for inferring Arrokoth's density; and we summarize results in Section 8.

2. The Shape and Spin of Arrokoth

Our knowledge of Arrokoth's shape has evolved significantly since its discovery by the *Hubble Space Telescope* in 2014 (Buie et al., 2018). Between discovery and encounter, Arrokoth was observed repeatedly by an impressive ground-based stellar occultation campaign (Buie et al., 2020), and continued observations by *Hubble* (Benecchi et al., 2019; Porter et al., 2018). The occultation campaign revealed the approximate size and bilobate shape of Arrokoth—although it was initially uncertain if Arrokoth was a contact binary, a pair of orbiting objects, or some other unusual shape (Buie et al., 2018, 2020). Monitoring by *Hubble* yielded an effectively flat light curve, hinting that Arrokoth's spin pole was likely pointed toward the Sun (Benecchi et al., 2019). It was not until the days leading up to encounter that the nature of Arrokoth came into focus (Figure 1).

Since the flyby, the *New Horizons* team has created over a dozen shape models of Arrokoth using a variety of methods of varying complexity and fidelity—ranging from fitting spheres to limb profiles (Bierson et al., 2019), to sculpting and digitizing clay models of the shape and then scanning the result (Kinczyk et al., 2019). Figure S1 in Supporting Information S1 shows this shape model menagerie. In this work, we focus on the three current shape models for Arrokoth: the global shape model (Figure 2a, Section 2.1), the stereo model (Figure 2b, Section 2.2), and the merged model (Figure 2c, Section 2.3). These three models are discussed in more detail in the subsequent sections. Of these three, the merged model is the most complete shape model at present, and it is what we use to calculate geophysical quantities throughout this paper.

The unusual shape of Arrokoth makes geography a challenge. Throughout this paper, we use the preliminary cartographic system defined for Arrokoth by Beyer, Weaver, et al. (2019). The z-axis is defined to be aligned with Arrokoth's spin axis, with the positive direction defined by the "right-hand rule." Following this convention, the *New Horizon*'s encounter hemisphere corresponds to the Arrokoth's southern hemisphere (Arrokoth's ventral side in nautical parlance). The x-axis is defined to be perpendicular to the z-axis and aligned with Arrokoth's

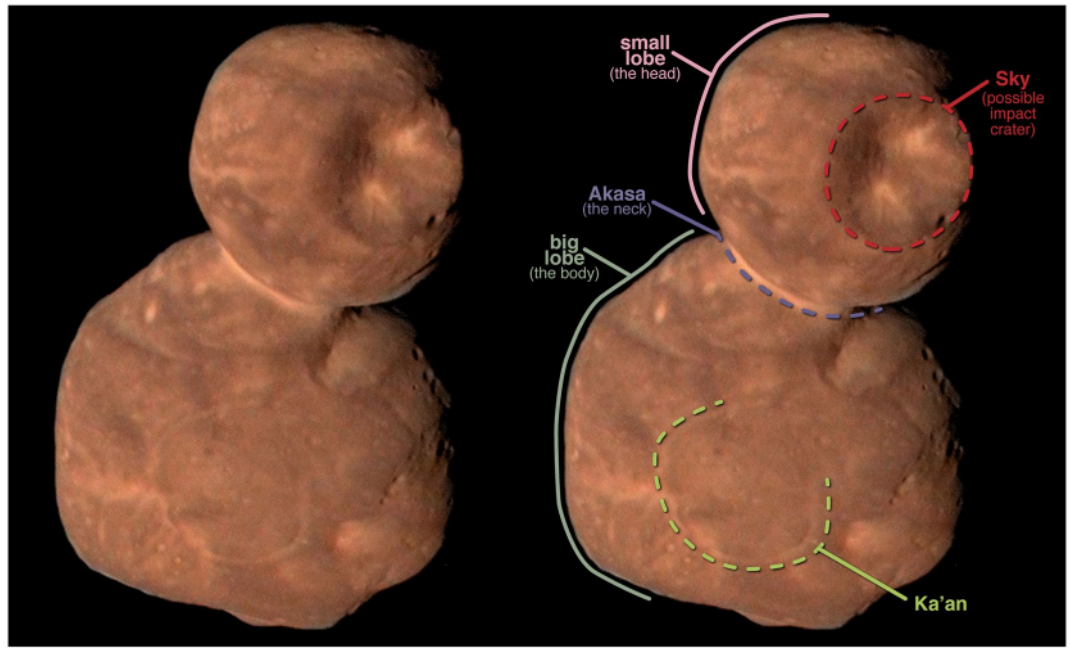

Figure 1. Highest resolution view of (486958) Arrokoth. The image combines low-resolution, enhanced color data (close to what the human eye would see) acquired by the *New Horizons* MVIC (Multispectral Visible Imaging Camera) instrument, with high-resolution panchromatic data acquired by the *New Horizons* LORRI (LOng-Range Reconnaissance Imager) instrument. The left-hand side of the figure shows the unannotated image, while the right-hand side has annotations labeling key features of Arrokoth, including the two lobes, the bright neck (named Akasa), the large crater on the small lobe (named Sky), and the annulus of bright material on the large lobe (named Ka'an). (Image credit: NASA, Johns Hopkins University Applied Physics Laboratory, Southwest Research Institute, Roman Tkachenko).

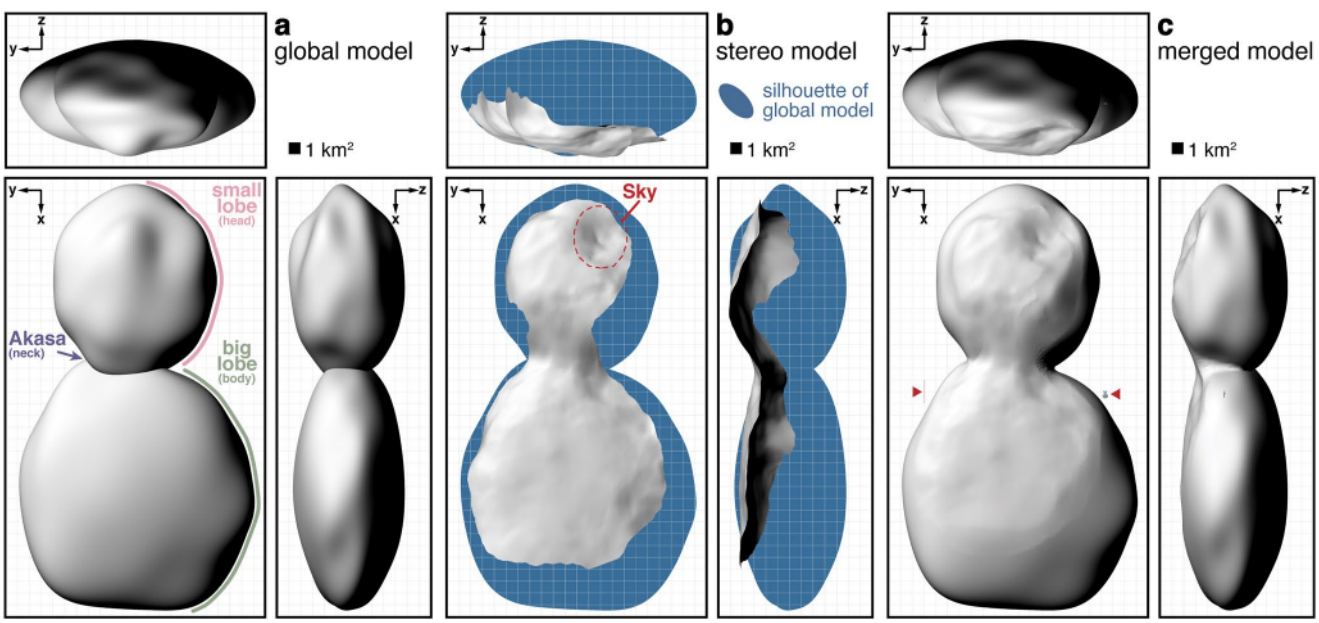

Figure 2. Orthographic views of the three current shape models for (486958) Arrokoth. (a) Global shape model (Section 2.1). (b) Stereo shape model (Section 2.2). The blue shaded region indicates the silhouette of the global shape model, for reference. The red dashed line encloses the putative impact crater, Sky. (c) Merged shape model, created by "stitching" the stereo shape model on the global shape model (Section 2.3). The three shape models are shown in the same reference frame, indicated by the *x*, *y*, and *z* reference vectors, following the preliminary Arrokoth cartographic system (Beyer, Weaver, et al., 2019). The background grid is shown in 1 km increments. In c, red arrows show the Golden Gate Bridge (left arrow, $l = 2$ km) and the USS Enterprise NCC-1701-D (right arrow, $l = 643$ m) for scale.

long axis, with the positive direction pointed toward the larger lobe (Arrokoth's bow), and the negative direction pointed toward the smaller lobe (Arrokoth's stern). The *y*-axis (which is associated with Arrokoth's port and starboard sides) is orthogonal to the *x*- and *y*-axes. The smaller and larger lobes are often colloquially referred to as Arrokoth's "head" and "body," respectively. It is possible to define a latitude/longitude system for Arrokoth based on these axes, although the convex shape of Arrokoth leads to degeneracies in latitude and longitude. Thus, all calculations were performed in a Cartesian reference frame, and we avoid using latitude/longitude when describing locations on the surface—instead favoring qualitative descriptions of locations. The origin of the Arrokoth reference frame is defined to be the center of mass of the body, which is calculated from the shape model and geophysical methods (see Section 4.1).

2.1. The Global Model

The first Arrokoth shape model is a long-wavelength model by Simon Porter and colleagues (Porter, Bierson, et al., 2019; Spencer et al., 2020; Stern et al., 2019), henceforth referred to as the "global model" (Figure 2a). The global model was developed by creating parameterized shape model, photometric function, and rotation state—and then forward modeling every *New Horizons* LORRI (LOng-Range Reconnaissance Imager) image of Arrokoth with the appropriate viewing geometry, illumination conditions, and LORRI point-spread function. These synthetic images were then compared to the actual images, and the model was iterated in order to provide the best fit to the images in a pixel-by-pixel, least-squared fashion fitting observed and modeled flux. The result was a best-fit global shape model, photometric function, rotation pole, rotation rate, and rotation phase. This approach was originally pioneered for modeling the small satellites of Pluto, Nix and Hydra (Porter, Showalter, et al., 2019; Porter et al., 2016), although it was updated to account for the bilobate shape of Arrokoth. The two lobes were parametrized as separate, overlapping "octanoids" (Kaasalainen & Viikinkoski, 2012), with a regularization designed to minimize details in the unimaged areas of Arrokoth. The resulting global model captures the long-wavelength shape of Arrokoth, but does not resolve small-scale structures (e.g., pits or craters), or the neck—which is necessarily v-shaped in this model due to the parameterized construction of the overlapping, dual lobes. At present, this model assumes a uniform albedo, meaning that Arrokoth's observed albedo variations (Hofgartner et al., 2021) may affect the reconstruction. The uncertainties in this global model have not been rigorously calculated, although preliminary estimates indicate that the overall dimensions are accurate to within ±0.5 km in the *x*- and *y*-directions, and ±2 km in the *z*-direction (Porter, Bierson, et al., 2019; Spencer et al., 2020; Stern et al., 2019). While the *z*-axis is the least well constrained, it is important to note that the flatness of the global model is not an artifact of this technique. Arrokoth's flatness can be verified in stereo viewing of successive flyby images, and is conclusively demonstrated by the high-phase image sequence (CA09) that imaged the crescent Arrokoth. Observations of occulted stars in sequential images unambiguously show that Arrokoth is substantially flattened (Spencer et al., 2020; Stern et al., 2019).

Figures S1e–S1h in Supporting Information S1 depict previous, superseded generations of the global model, with progressively higher resolution. Figure S1f in Supporting Information S1 was published in Stern et al. (2019), and the current global model (Figure 2a and Figure S1k in Supporting Information S1) was published in Spencer et al. (2020). The models are available for download in the Supporting Information of those papers.

2.2. The Stereo Model

The second Arrokoth shape model is a high-resolution shape model of the encounter hemisphere from stereo photogrammetry by Ross Beyer and colleagues (Beddingfield et al., 2019; Beyer, Porter, et al., 2019; Spencer et al., 2020), henceforth referred to as the "stereo model" (Figure 2b). The stereo model was constructed by using the two best pairs of LORRI images of Arrokoth. The NASA Ames Stereo Pipeline (Beyer et al., 2018) was used to select reference points, perform bundle adjustments, and then create a stereo point cloud. The resulting stereo model captures smaller scale topographic features better than the global model, but is only capable of constraining the topography on the ventral, fully illuminated and imaged face of Arrokoth. The uncertainties in the resulting stereo model have not been rigorously calculated, although are generally expected to be of-order 100-m.

Figure S1i in Supporting Information S1 depict a previous, superseded generation of the stereo model. The current stereo model (Figure 2b and Figure S1l in Supporting Information S1) was published in Spencer et al. (2020), and is available for download in the supplementary materials of that paper.

2.3. The Merged Model

The third Arrokoth shape model is a merged shape model, created by grafting the stereo model onto the global model (Beyer, Porter, et al., 2019; Spencer et al., 2020), henceforth referred to as the "merged model" (Figure 2c). The merged model leverages the strengths of both the stereo and global models: the global model is best-constrained at the limb of Arrokoth, while the stereo model is best-constrained on the ventral face of Arrokoth. To construct the merged model, Beyer, Porter, et al. (2019) fit the rigid stereo model to the global model using an iterative closest point algorithm (Besl & McKay, 1992; Chen & Medioni, 1992). In many places, the fitted stereo model either hangs above, or dips below, the surface of the global shape model. This can be seen by comparing the stereo model with the silhouette of the global model in Figure 2b. To create the merged model, these global and stereo models are manually trimmed and "stitched" together. In some places, the global model is trimmed to conform to the stereo model (e.g., the ventral face of the small lobe), and in other places, the stereo model is trimmed to conform to the global model (e.g., the distal end of the large lobe).

Figure S1j in Supporting Information S1 depict a previous, superseded generation of the merged model, combining global and stereo models shown in Figures S1h–S1i in Supporting Information S1. The current global model (Figure 2c and Figure S1m in Supporting Information S1) was described in Spencer et al. (2020). The merged shape model will be publicly released as part of a forthcoming *New Horizons* Planetary Data System Small Bodies Node (https://pds-smallbodies.astro.umd.edu/data_sb/missions/nh-kem/index.shtml).

2.4. Caveats and Other Shape Models

It is important to note that while we present results based on three shape models, these three models are not completely independent from one another. The stereo model is iteratively fit and trimmed to the global model to create the merged model. The global model is the only model that constrains the total volume of Arrokoth, which is critical in determining geophysical quantities (e.g., surface gravity). This degeneracy results in some interesting differences and similarities in the derived parameters for each of the three models.

While we focus on these three shape models, additional efforts within the *New Horizons* team have provided insight into other aspects of Arrokoth's topography. Bierson et al. (2019) have measured limb profiles in all flyby images, which provide high-resolution, continuous topographic profiles. Schenk et al. (2021) have used stereo photoclinometry to investigate the topography of small-scale (<1 km) pits and troughs on Arrokoth, which are unresolved in the stereo model considered here. Future work may produce an additional, high-resolution shape models of Arrokoth that merges all of these separate analyses.

2.5. The Rotation of Arrokoth

The rotation rate and spin pole of Arrokoth has been well-characterized by analysis of the entire sequence of *New Horizons* approach images (Buie et al., 2020; Porter, Bierson, et al., 2019; Spencer et al., 2020; Stern et al., 2019). The rotation rate is 15.9380 ± 0.0005 hr (Buie et al., 2020), and the obliquity is 99° ± 1° (Spencer et al., 2020). There is no evidence for non-principal axis rotation. At present, there is no measurement of a center-of-mass–center-of-figure offset.

2.6. The Unknown Density of Arrokoth

At present, there is no direct constraint on Arrokoth's mass or density. The *New Horizons* flyby was sufficiently fast (flyby velocity: 14.43 km/s) and distant (closest approach distance: 3,538.5 km) that traditional gravity science (i.e., measuring the perturbation of *New Horizons*' trajectory due to the mass of Arrokoth) was not feasible. *New Horizons* performed an extensive search for natural satellites around Arrokoth, although none has

been found down to a limiting diameter of 100 m for much of Arrokoth's Hill sphere (about 4 million km radius: Spencer et al., 2020; Stern et al., 2019). In the absence of direct gravity measurements or observations of natural satellites, we are forced to use a combination of geophysical inferences to constrain the density. We considered a broad range of possible densities—from <100 to >1,000 kg/m^3. Unless otherwise specified, we assume that the two lobes of Arrokoth have the same density. For most figures in this work, we assume a nominal density of 235 kg/m^3, which is justified in Sections 7.1.

3. Geophysical Models of Arrokoth

We developed three pipelines for evaluating the geophysical characteristics of Arrokoth: the mascon model (led by James Tuttle Keane, Section 3.1), the column model (led by Orkan Mehmet Umurhan, Section 3.2), and the polyhedron model (led by James Tuttle Keane, Section 3.3). Each approach has different strengths and weaknesses, but were all useful at different stages of the analysis (and at during stages of the Arrokoth encounter). For example: the mascon model is easy to implement (perfect for quick analysis during a flyby), flexible, but computationally inefficient; the polyhedron model is harder to implement but more accurate and efficient; the column model is more calculation-time efficient than the mascon model and easier to implement than the polyhedron model, but it is both less accurate than the polyhedron model and is the least flexible amongst the other two. The mascon model was used in all early geophysical analyses (McKinnon et al., 2020; Spencer et al., 2020; Stern et al., 2019). In this paper, we generally focus on results from the polyhedron model. In all cases, these models were benchmarked against each other, and by duplicating comparable analyses of asteroid (101955) Bennu, which was well-characterized by the *OSIRIS-REx* mission (Scheeres et al., 2016, 2019).

Amarante and Winter (2020) also performed a comparable analysis of the geophysical environment of Arrokoth, although they used an earlier shape model of Arrokoth (Model f in Figure S1 in Supporting Information S1; Stern et al., 2019). Nonetheless, their results are in general agreement with what we present here.

All three of the pipelines described here are numerical. However, in some cases it is possible to analytically derive solutions for the geophysical environment of Arrokoth-like bodies. For example, Dobrovolskis (2021) present analytical solutions for duplexes of spheres (akin to Model a in Figure S1 in Supporting Information S1). These models are particularly useful for building physical intuition about the body. However, owing to the complexity of the present shape model, we do not consider analytical solutions further.

3.1. The Mascon Model

In the mascon model, we approximate the mass distribution of Arrokoth by filling it with spherical test particles, that is, "mascons." The mascons were distributed on an equally spaced, simple cubic lattice. The spacing and size of the mascons was chosen based on a combination of sensitivity tests, and by balancing accuracy with computation time. Through experimentation, we found diminishing returns for mascons less than 50-m in radius (translating to nearly 5 million individual mascons), and that decreasing mascon size did not change the results (e.g., moments of inertia) at an appreciable level.

The mass of each spherical mascon is: $m_i = 4\rho' \pi r_i^3/3$, where ρ' and r_i are the density and radius of the ith mascon. For mascons well within Arrokoth's hull, r_i is one-half the separation of the mascons (i.e., for a 200-m mascon spacing, the radius of each mascons is 100 m). For mascons near the edge of the hull, r_i was set to the distance between the center of mascon and the surface. The simple cubic lattice geometry results in a substantial fraction of void space between the spherical mascons. To achieve the desired density, ρ, we increased the density of each mascon by a correction factor to remove the effect of this porosity: $\rho' = \rho V/V_{mascons}$, where V is the volume of Arrokoth and $V_{mascons}$ is the volume of the ensemble of spherical mascons. The former can be calculated either by summing a higher resolution grid of cubical mascons that lacks void space, or by summing the volumes of the individual tetrahedra making up the shape model. The net result is an ensemble of over-dense mascons that sum to the same total mass as a uniformly dense Arrokoth.

With an ensemble of mascons, the calculation of relevant geophysical quantities is straight-forward (e.g., Taylor, 2005). For example, the gravitational acceleration, $\vec{g}$ can be calculated at any location, $\vec{r}$, by summing over the ensemble of n mascons:

$$\vec{g}(\vec{r}) = -\sum_{i=1}^{n} \frac{Gm_i}{|\vec{r} - \vec{d}_i|^3} \left(\vec{r} - \vec{d}_i\right), \tag{1}$$

where m_i and $\vec{d}_i$ are the mass and position vector of the ith of n mascons, and G is the gravitational constant ($G = 6.67 \times 10^{-11}$ m^3 kg^{-1} s^{-2}). Throughout this work, vectors are indicated by arrows (e.g., $\vec{r} = [r_x, r_y, r_z]$), and vertical bars indicate norms (e.g., $|\vec{r}| = \sqrt{r_x^2 + r_y^2 + r_z^2}$). Similarly, the gravitational potential, $U_G(\vec{r})$ can be calculated:

$$U_G(\vec{r}) = -\sum_{i=1}^{n} \frac{Gm_i}{|\vec{r} - \vec{d}_i|}. \tag{2}$$

3.2. The Column Model

A second approach is to fill Arrokoth with cylindrical columns, or line elements. Like the sphere or point mass based mascon approach (Section 3.1), the gravitational potential and acceleration for a line element can be written simply, and the total potentials and accelerations for the entire body can be approximated by summing over a set of columns or line elements filling Arrokoth. This approach is computationally faster than the mascon approach (because it requires fewer line elements to fill Arrokoth). The column model was used for some interim calculations (e.g., Umurhan et al., 2020) and for bench-marking other models, however we do not consider it further here.

3.3. The Polyhedron Model

In the polyhedron model, we approximate the mass distribution of Arrokoth as a series of constant density polyhedra. This approach, developed by Robert Werner and colleagues in a series of papers (Werner, 1994, 1997; Werner & Scheeres, 1997), is the now the standard approach for modeling the gravity fields around small bodies of irregular shape. Werner's approach uses Gauss' Divergence Theorem to transform the usual volume integrals (e.g., $U_G(\vec{r}) = \iiint_V G\rho/r \, \mathrm{d}V$, where d$V$ is the volume element) into integrals over the surface (e.g., $U_G(\vec{r}) = 1/2 \iint_S \hat{n} \cdot \hat{r} \, \mathrm{d}S$, where d$S$ is the surface element), which in turn can be further simplified into purely geometric calculations. While the equations for gravitational potential, $U_G(\vec{r})$, and acceleration, $\vec{g}(\vec{r})$, are closed-form equations, they are sufficiently complex and lengthy that we omit them here. We refer the reader specifically to Werner (1994) which provides a clearly laid out derivation and system of equations to solve. Despite its complexity, the polyhedron approach is far more accurate and computationally efficient than either the mascon (Section 3.1) or column (Section 3.2) methods. Moreover, the polyhedron approach gives an exact solution.

4. The Geophysical Environment of Arrokoth

4.1. Center of Mass

The center of mass, $\vec{r}_{com}$, for a solid body is computed by integrating over the mass distribution (e.g., Scheeres, 2012; Taylor, 2005). In this work, we calculate the center of mass using the mascon model (Sections 3.1):

$$\vec{r}_{com} = \frac{1}{M} \sum_{i=1}^{n} m_i \vec{d}_i, \tag{3}$$

where m_i and $\vec{d}_i$ are the mass and position vector of the ith of n mascons, and M is the total mass of all of the mascons (i.e., the mass of Arrokoth). While we used the mascon model, we note that this could be done with the polyhedron model, as in Dobrovolskis (1996).

Table 1 lists the calculated centers of mass of Arrokoth, and for each of the two lobes separately, assuming a uniform density. To calculate the center of mass for each lobe, we "sliced" the neck of Arrokoth with a planar slice, manually constructed to minimize the cross-sectional area of the neck (Figures 3a and 3b). With this defi-

Table 1
Derived Bulk Properties of (486958) Arrokoth

Parameter	Entire body	Big lobe	Small lobe
Volume (km^3)	3,185.0	2,088.5	1,096.5
Volume equivalent diameter (km)	18.26	15.86	12.79
Mass (kg)	7.485×10^{14}	4.908×10^{14}	2.577×10^{14}
Bounding box, x	−19.49 to 16.46 km	−4.74 to 16.46 km	−19.49 to −3.74 km
	$\Delta_x = 35.95$ km	$\Delta_x = 21.20$ km	$\Delta_x = 15.75$ km
Bounding box, y	−10.06 to 9.84 km	−10.06 to 9.84 km	−6.91 to 6.94 km
	$\Delta_y = 19.90$ km	$\Delta_y = 19.90$ km	$\Delta_y = 13.85$ km
Bounding box, z	−4.96 to 4.79 km	−4.26 to 4.79 km	−4.96 to 4.79 km
	$\Delta_z = 9.75$ km	$\Delta_z = 9.05$ km	$\Delta_z = 9.75$ km
Center of mass, $\vec{r}_{com}$	$\begin{bmatrix} 0.101 \\ 0.020 \\ 0.079 \end{bmatrix}$ km	$\begin{bmatrix} 6.011 \\ 0.056 \\ 0.125 \end{bmatrix}$ km	$\begin{bmatrix} -11.155 \\ -0.047 \\ -0.010 \end{bmatrix}$ km
Principal moment of inertia, A (kg/m2)	1.57×10^{22}	1.19×10^{22}	3.76×10^{21}
Principal moment of inertia, B (kg/m^2)	6.80×10^{22}	1.39×10^{22}	4.32×10^{21}
Principal moment of inertia, C (kg/m^2)	7.72×10^{22}	2.17×10^{22}	5.68×10^{21}
Principal axis of inertia, $\vec{A}$	$\begin{bmatrix} 0.999985 \\ 0.000305 \\ 0.005556 \end{bmatrix}$	$\begin{bmatrix} 0.995025 \\ -0.099489 \\ -0.005272 \end{bmatrix}$	$\begin{bmatrix} 0.988373 \\ -0.152025 \\ -0.002805 \end{bmatrix}$
Principal axis of inertia, $\vec{B}$	$\begin{bmatrix} -0.000322 \\ 0.999995 \\ 0.003112 \end{bmatrix}$	$\begin{bmatrix} 0.099463 \\ 0.995029 \\ -0.004970 \end{bmatrix}$	$\begin{bmatrix} 0.152000 \\ 0.98739 \\ 0.044125 \end{bmatrix}$
Principal axis of inertia, $\vec{C}$	$\begin{bmatrix} -0.005555 \\ -0.003114 \\ 0.999980 \end{bmatrix}$	$\begin{bmatrix} 0.005740 \\ 0.004421 \\ 0.999974 \end{bmatrix}$	$\begin{bmatrix} -0.003939 \\ -0.044038 \\ 0.999022 \end{bmatrix}$

Note. Properties are calculated from analysis of the merged shape model of Arrokoth (Sections 2.3). Mass and principal moments of inertia assume a nominal density of 235 kg/m^3 (Sections 7.1). Principal axes of inertia are normalized (i.e., $|\vec{A}| = 1$). Δ indicates the length of the edge of the bounding box. Quantities in brackets indicate vectors. The bounding box, center of mass, and axes of inertia are reported in the reference frame for the underlying merged shape model, that is, the reference frame of the.OBJ shape file produced by Beyer, Porter, et al. (2019). This reference frame is similar to the principal axis reference frame, but not exactly identical. The merged shape model will be publicly released as part of a forthcoming *New Horizons* Planetary Data System Small Bodies Node (https://pds-smallbodies.astro.umd.edu/data_sb/missions/nh-kem/index.shtml).

nition of a neck "slice," the surface area of the neck interface is approximately 30.5 km^2. (In the reference frame of the merged model, this plane can be described by the equation: $-0.13y + 0.06z - 4.18 = x$.) We then can calculate the center of mass of each lobe separately by summing over the ensemble of mascons on one side of the neck or the other. The center of masses of the two lobes are separated by 17.157 km, with the center of mass of the entire body located 5.910 km away from the center of mass of the big lobe (or 35% of the distance between the two center of masses), and located well within the big lobe. The center of mass of the entire body is very nearly on the line joining the centers of mass of the two lobes—only offset by 80 m.

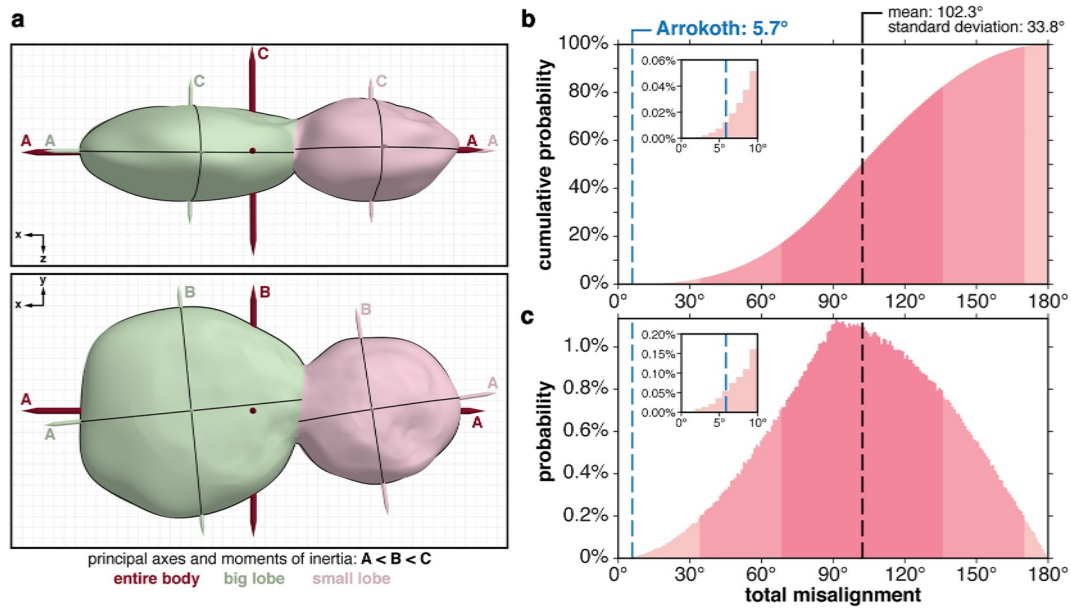

Figure 3. Principal axes of inertia of (486958) Arrokoth. (a) Two orthographic views of the global shape model of Arrokoth (Sections 2.1). Red, green, and pink vectors correspond to the principal axes of inertia ($\vec{A}$, $\vec{B}$, and $\vec{C}$) for the entire body, big lobe, and small lobe, respectively. Black lines show the planes orthogonal to the principal axes for each of the separate lobes (effectively the equators and "meridians" of each lobe). Background grid and symbols are described in Figure 2. (b) Cumulative probability of two randomly oriented reference frames being aligned as a function of total misalignment. (c) Probability of two randomly oriented reference frames being aligned as a function of total misalignment.

4.2. Inertia Tensor and Principal Axes of Inertia

The rotational dynamics of any object is governed by its inertia tensor, I, which describes the distribution of mass within the body (e.g., Scheeres, 2012; Taylor, 2005). The complete inertia tensor is:

$$\boldsymbol{I} = \begin{bmatrix} I_{xx} & I_{xy} & I_{xz} \\ I_{yx} & I_{yy} & I_{yz} \\ I_{zx} & I_{zy} & I_{zz} \end{bmatrix}. \tag{4}$$

Throughout this work, tensors are indicated in bold. We calculate the inertia tensor using the mascon model (Sections 3.1), which enables the rapid calculation of the inertia tensor by summing over mascons. The diagonal terms are given by:

$$I_{xx} = \sum_{i=1}^{n} m_i \left(y_i^2 + z_i^2\right), \tag{5}$$

and similarly for I_{yy} and I_{zz}. The off-diagonal terms are given by:

$$I_{xy} = -\sum_{i=1}^{n} m_i x_i y_i, \tag{6}$$

and so on for the other terms. We calculate the inertia tensor with respect to the center of mass (i.e., $[x_i, y_i, z_i] = \vec{d}_i - \vec{r}_{com}$). Note that the inertia tensor is a symmetric matrix (e.g., $I_{xy} = I_{yx}$), so there are only six independent components in the tensor.

For any real objects, there exists a coordinate system where all off-diagonal terms go to zero, and the inertia tensor is completely described by a diagonal tensor with three principal moments of inertia: $A \leq B \leq C$. This coordinate system is defined by three principal axes of inertia: $\vec{A}$, $\vec{B}$, and $\vec{C}$. These principal moments and principal axes of

inertia can be determined by calculating the eigenvalues and eigenvectors of $\boldsymbol{I}$. For most objects with uniform densities, the maximum (minimum) principal axis of inertia correspond to the short (long) axis of the object.

Table 1 lists the calculated principal moments and axes of inertia of Arrokoth, and for each of the two lobes separately, assuming a uniform density. Figure 3a shows the principal axes of inertia for each lobe and the entire body.

Curiously, the principal axes of inertia of Arrokoth's two lobes are very nearly parallel to one another, and of the body as whole. For example, the maximum principal axis of inertia of Arrokoth is very nearly parallel to both the maximum principal axis of inertia of the big lobe, and the maximum principal axis of inertia of the small lobe (McKinnon et al., 2020; Spencer et al., 2020; Stern et al., 2019). This alignment is not necessarily an expected outcome for small contact binaries. For example, the principal axes of lobes of 67P/Churyumov-Gerasimenko—the most well-characterized contact binary in the Solar System—are not parallel to one another, nor the principal axes of the entire body, and are misaligned by several 10s of degrees (Jorda et al., 2016). To quantify this misalignment, we define the "total misalignment" as the sum of the rotation angles required to align the two sets of axes of inertia. The total misalignment is the sum of two rotation angles: one angle to align the maximum principal axes, and one to rotate about that principal axis and align the other two principal axes. For Arrokoth's two lobes, the total misalignment is only 5.86°. To evaluate the significance of this misalignment, we created 1 million randomly oriented sets of principal axes, and calculated the distribution of total misalignment angles. The randomly oriented sets of principal axes were generated by first creating a randomly oriented maximum principal axis of inertia—defined by $\vec{r}_{random} = \left[\cos(v)\sqrt{1-u^2}, \sin(v)\sqrt{1-u^2}, u\right]$, where u is a random variate ranging between -1 and 1, and v is a random variate ranging between 0 and 2π—and then calculating a randomized, but orthogonal minimum principal axis of inertia by calculating the cross-product between the random maximum principal axis of inertia and a second randomly oriented vector. Figures 3b and 3c show the resulting probability, and cumulative probability distribution function for these randomly oriented pairs. The mean total misalignment angle between two randomly oriented sets of principal axes is 102.3° ± 33.8°. Arrokoth's total misalignment of 5.86° thus corresponds to a 2.9σ outlier. The cumulative probability of such a small misalignment is 0.01% (Figure 3c). McKinnon et al. (2020) arrived at a similar probability (0.02%) through a more analytic analysis. Such a statistically significant, small total alignment suggests that the alignment of Arrokoth's two lobes is not due to chance, but rather reflects some driving physical process, such as tidal locking of the two lobes prior to merger (e.g., McKinnon et al., 2020; Stern et al., 2019).

4.3. Surface Accelerations

The motion of surface material on Arrokoth is governed by the forces acting on it. The total acceleration experienced by a particle on the surface of Arrokoth, $\vec{a}(\vec{r})$, can be written in the rotating reference frame as (e.g., Scheeres, 2012; Scheeres et al., 2016; Taylor, 2005):

$$\vec{a}(\vec{r}) = \left(\nabla U_G(\vec{r})\right) + \left(\vec{\omega} \times \vec{\omega} \times \vec{r}\right) + \left(2\vec{v} \times \vec{\omega}\right) + \left(\dot{\vec{\omega}} \times \vec{r}\right), \tag{7}$$

where ∇ is the gradient operator, dots indicate time derivatives (e.g., $\dot{\vec{\omega}} = d\vec{\omega}/dt$), and is the velocity vector $\left(\vec{v} = \dot{\vec{r}}\right)$. The first term in Equation 7 is the acceleration due to gravity from Arrokoth, which is written as the gradient of the gravitational potential, $U_G(\vec{r})$. The gravitational potential and acceleration can be calculated from the geophysical model of Arrokoth (Sections 3). The second and third terms in Equation 7 are the centrifugal and Coriolis accelerations, respectively, which arise from the rotating reference frame. When reporting total surface accelerations, we generally assume that we are evaluating accelerations on stationary surface particles (thus $\vec{v} = 0$), so we can omit the Coriolis acceleration—although that assumption is revisited in Section 6. The final term in Equation 7 is the acceleration that arises if the body's rotation rate is changing, which could occur if Arrokoth was in non-principal axis rotation (Scheeres, 2012). At present, there is no evidence for non-principal axis rotation of Arrokoth (Sections 2.5), so we ignore this term as well.

Figure 4 shows the total accelerations across the surface of Arrokoth, assuming a nominal density of 235 kg/m^3 (justified in Section 7.1). For the nominal density (235 kg/m^3), the total accelerations are small, ranging across Arrokoth from 0.18 to 0.53 mm/s^2 (with an area-weighted mean of 0.40 ± 0.07 mm/s^2), with the highest total acceleration on the ±z (ventral and dorsal) faces of the two lobes, and lowest on the equators of the two lobes

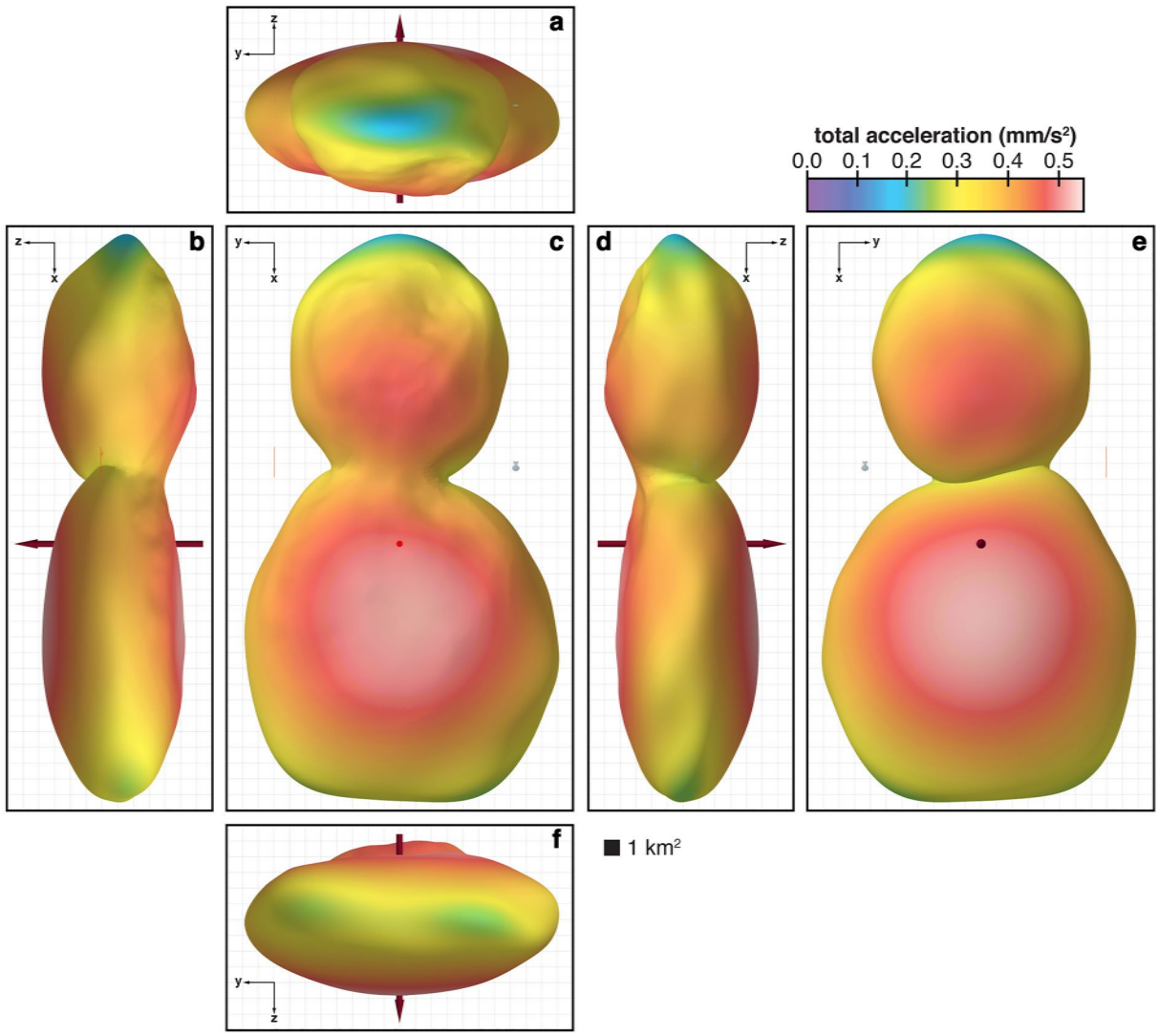

Figure 4. Total accelerations on the surface (486958) Arrokoth. The total acceleration is the magnitude of the sum of the gravitational and rotational accelerations. *x*, *y*, and *z* reference vectors indicate the shape model reference frame, following the preliminary Arrokoth cartographic system (Beyer, Weaver, et al., 2019). Following nautical parlance, (a) shows the stern elevation of Arrokoth, (b) shows the port elevation of Arrokoth, (c) shows the ventral plan of Arrokoth (the *New Horizons* encounter hemisphere), (d) shows the port elevation of Arrokoth, (e) shows the dorsal plan of Arrokoth, and (f) shows the bow elevation of Arrokoth. All views are orthographic. The background grid is shown in 1 km increments, and the Golden Gate Bridge (length: 2 km) and the USS Enterprise NCC-1701-D (length: 643 m) can be seen for scale off the port and starboard sides of Arrokoth, respectively. The red vector indicates Arrokoth's spin axis (which is presumed to be coincident with the calculated maximum principal axis of inertia for Arrokoth, as shown in Figure 3).

(where the centrifugal force is largest, and most directly counteracts the gravity of the body). The total accelerations scale quasi-linearly with bulk density (the gravitational acceleration for a sphere is proportional to density). For a larger density of 500 kg/m^3, the total accelerations would be larger: ranging from 0.59 to 1.12 mm/s^2 (with an area-weighted mean of 0.93 $\pm$ 0.10 mm/s^2).

4.4. Geopotential and Geopotential Elevation

We define the geopotential, U, at an arbitrary location, $\vec{r}$, as the sum of the gravitational potential, U_G, and rotational potential, U_R (e.g., Scheeres, 2012; Scheeres et al., 2016):

$$U(\vec{r}) = U_G(\vec{r}) + U_R(\vec{r}) . \quad (8)$$

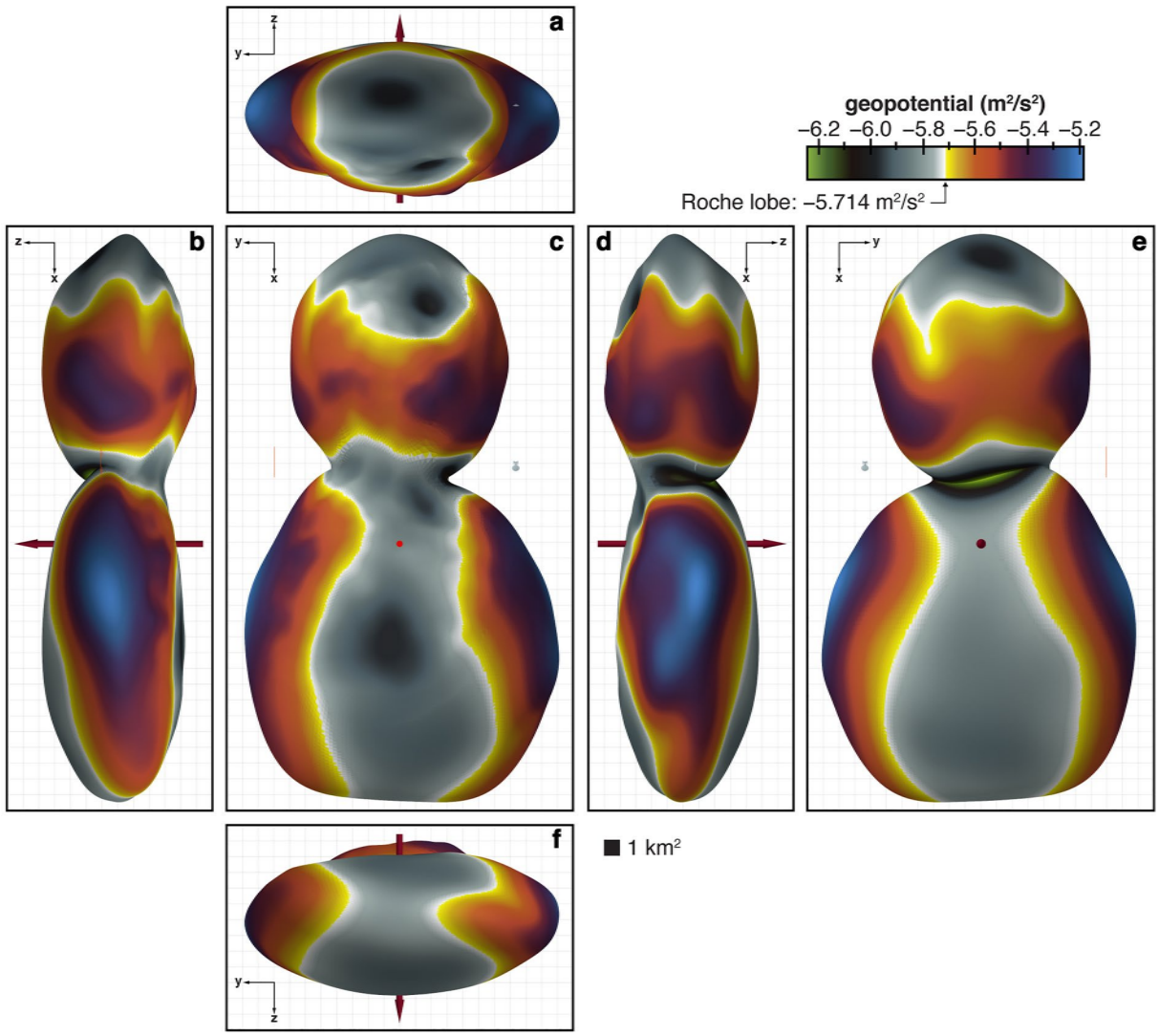

Figure 5. Geopotential on the surface of (486958) Arrokoth. The geopotential is the sum of the gravitational and rotational potential. Views (a–f), the background grid, and symbols are described in Figure 4.

The gravitational potential can be calculated from the geophysical model of Arrokoth (Sections 3). The rotational potential in the rotating reference frame can be written as:

$$U_R(\vec{r}) = -\frac{1}{2}\omega^2 r_\perp^2 \tag{9}$$

where ω is the rotation rate ($\omega = 2\pi/P$, where P is the rotation period), and $r_\perp$ is the perpendicular distance from the point of interest, $\vec{r}$, to the spin axis, $\vec{\omega}$.

Figure 5 shows the geopotential evaluated across the surface of Arrokoth, assuming a uniform density of 235 kg/m^3 (our nominal Arrokoth density, justified in Section 7.1). The geopotential ranges from −6.3 to −6.2 m^2/s^2, with an area-weighted mean of −5.7 ± 0.2 m^2/s^2. On Arrokoth, the geopotential lows are on the $\pm z$ (ventral and dorsal) faces of the two lobes and in the neck, while the geopotential highs are on the equators of the two lobes, and on the $\pm y$ (port and starboard) edges of the large lobe in particular. For a larger density of 500 kg/m^3, the geopotential would be more negative (as the gravitational potential becomes deeper): ranging from −13.2 to −9.9 m^2/s^2 (with an area-weighted mean of −11.2 ± 0.7 m^2/s^2).

On large, quasi-spherical planetary bodies, the distance from the center of the body to the surface—that is, the radius, topography, or geometric elevation—is often an important, meaningful geophysical measurement since it is correlated with changes in the geopotential. For example, the top of a terrestrial mountain is a topographic and geopotential high, and landslides on that mountain will flow into the surrounding topographic and geopotential lows. However, on small bodies with irregular shapes and mass distributions, topography and geopotential are not always so interchangeable. Instead, it is more appropriate to consider elevation with respect to the geopotential. We define the geopotential elevation, $h(\vec{r})$ (Scheeres, 2012; Scheeres et al., 2016):

$$h(\vec{r}) = \frac{U(\vec{r}) - U_0}{a(\vec{r})} \tag{10}$$

where $U(\vec{r})$ is the geopotential (Equation 8), U_0 is a reference geopotential value, and $a(\vec{r})$ is the magnitude of the local total acceleration ($a(\vec{r}) = |\vec{a}(\vec{r})|$; Sections 4.3). We opted to define geopotential elevations with respect to the geopotential low across its whole surface (i.e., U_0 is the global minimum value of $U(\vec{r})$), which occurs in the neck of Arrokoth (Figure 5).

Figure 6 shows the geopotential elevation on Arrokoth, assuming a uniform density of 235 kg/m^3 (Sections 7.1). This figure contains much of the same information as in Figure 5, but, by virtue of the units, is more intuitive. Again, we see that the geopotential lows are on the $\pm z$ (ventral and dorsal) faces of the two lobes and in the neck, while the geopotential highs are on the equators of the two lobes. Overall, the variations of Arrokoth's geopotential elevation are quite small—never exceeding 2.9 km, with an area-weighted mean of 1.5 $\pm$ 0.6 km. For a larger density of 500 kg/m^3, the geopotential elevations would be larger: peaking at 5.05 km (with an area-weighted mean of 2.24 $\pm$ 0.95 km). The small variations in geopotential elevation stand in stark contrast to the variations on Arrokoth's geometric elevation (i.e., radius) shown in Figure 7, which range between 3.6 and 19.7 km, reiterating the importance of considering the geopotential when investigating geophysical processes.

4.5. Surface Slopes

The surface slope, θ, is defined as the angle between the total acceleration vector, $\vec{a}(\vec{r})$ (Sections 4.3), and the surface normal at some location on Arrokoth's surface, $\vec{n}(\vec{r})$:

$$\theta = 180° - \cos^{-1}\left(\frac{\vec{a}(\vec{r})}{a(\vec{r})} \cdot \vec{n}(\vec{r})\right). \tag{11}$$

The surface normals are defined by the shape model [Sections 2, and are defined to be unit vectors $(|\vec{n}(\vec{r})| = 1)$]. (The 180° in Equation 11 comes about because surface normals are defined to be pointing outward, whereas most of the time the acceleration is pointing inward.) Slopes are equal to 0° if the normal and total acceleration are aligned (corresponding to a "flat" surface with respect to the geopotential), and equal to 90° if the normal and acceleration are orthogonal (corresponding to a "vertical" cliff with respect to the geopotential). Slopes can also be thought of as the gradient of the geopotential elevation (Sections 4.4, Figure 6).

Figure 8 shows the surface slopes on Arrokoth, assuming a uniform density of 235 kg/m^3 (our nominal Arrokoth density, justified in Section 7.1). In general, the slopes of Arrokoth are expected to be low (area-weighted mean of 10.4 $\pm$ 7.5°), with the highest slopes located in the neck and in the large depression on the small lobe. The distribution of slopes is discussed in more detail in Section 7.1.

4.6. Jacobi Speed

In addition to quantifying the overall character of Arrokoth, the geopotential can be be directly related to the dynamical motion of particles across its surface. For particle motion, we can define a conserved quantity in the rotating reference frame—the Jacobi integral—that bounds possible motion (e.g., Scheeres, 2012; Scheeres et al., 2016):

$$J = \frac{1}{2}v^2 + U(\vec{r}), \tag{12}$$

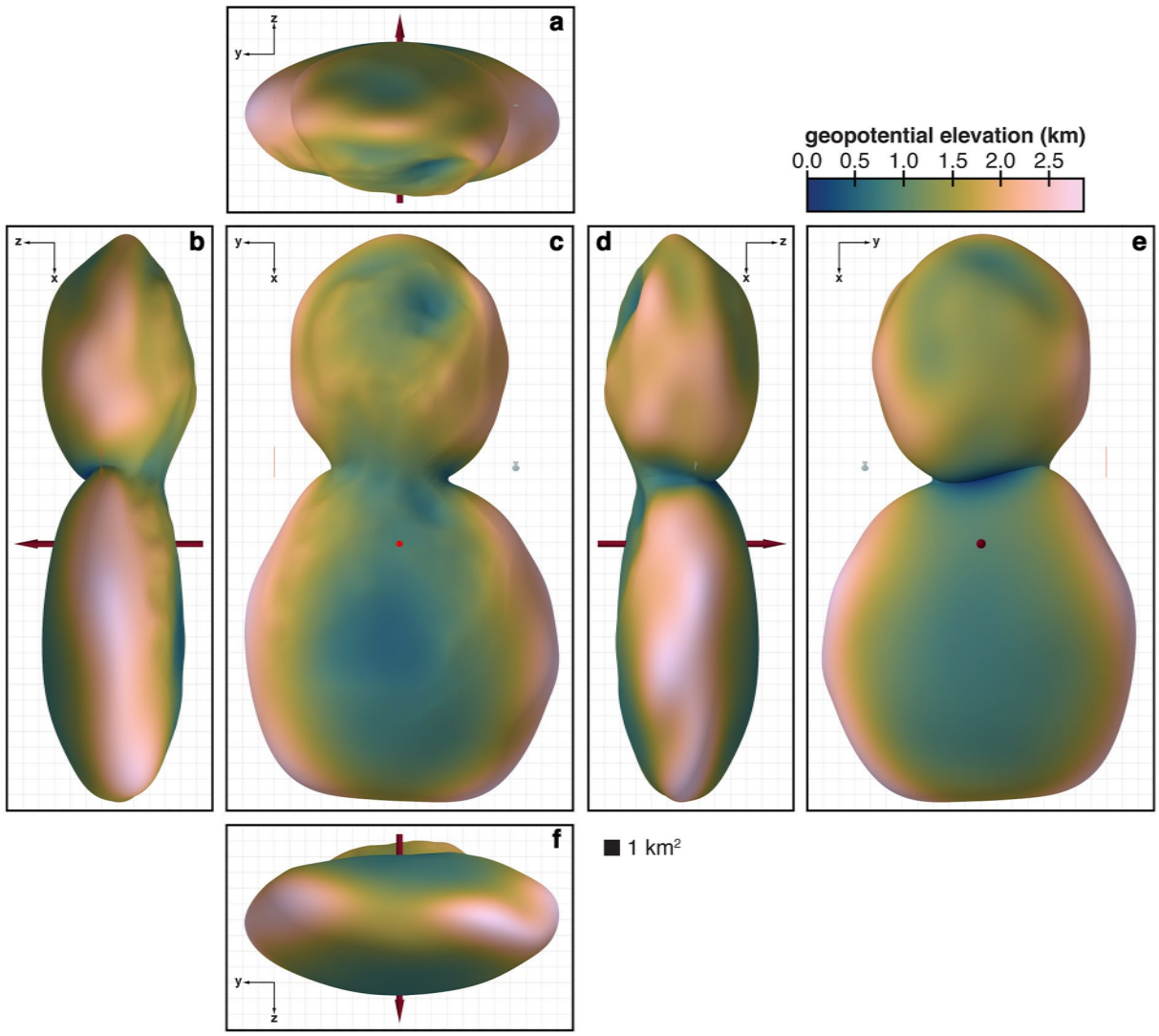

Figure 6. Geopotential elevation of the surface of (486958) Arrokoth. Geopotential elevation is elevation measured with respect to the geopotential (Figure 5). Views (a–f), the background grid, and symbols are described in Figure 4.

where v is the magnitude of the particle velocity in the rotating reference frame (i.e., its speed), and $U(\vec{r})$ is the geopotential (Equation 8). (This is simply conservation of energy in a rotating reference frame.) If we consider a particle starting at location $\vec{r}_1$ with speed v_1, moving to location $\vec{r}_2$, we can determine the speed that the particle would need to gain or lose in transit by equating the Jacobi integral at the start and end of its journey:

$$v = \sqrt{v_1^2 - 2\left(U(\vec{r}_2) - U(\vec{r}_1)\right)}. \tag{13}$$

This speed is independent of the exact path (or even the existence of a path) between $\vec{r}_1$ and $\vec{r}_1$, and thus could apply to either ballistic flight above the surface or frictionless sliding across the surface. We define the Jacobi speed, v_J, as the speed a particle would achieve if moving from the highest point in the geopotential, $U_{\max}$, to an arbitrary location on Arrokoth, $\vec{r}$ (or equivalently, the speed required to move from arbitrary location $\vec{r}$ to the highest point in the geopotential):

$$v_J = \sqrt{-2\left(U(\vec{r}) - U_{\max}\right)}. \tag{14}$$

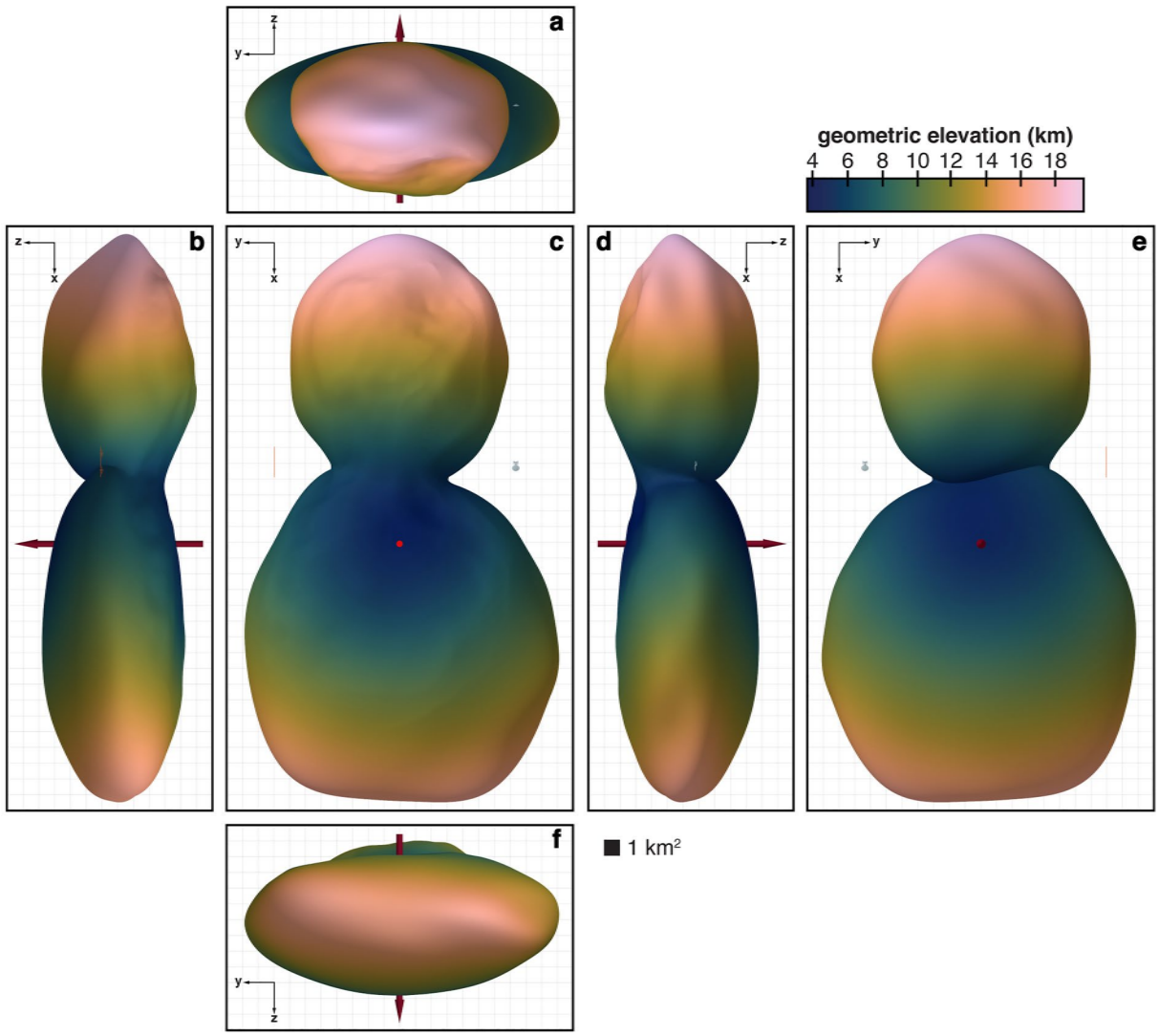

Figure 7. Geometric elevation of the surface of (486958) Arrokoth. Geometric elevation is the distance from the surface to the center of mass (i.e., the radius). Views (a–f), the background grid, and symbols are described in Figure 4.

Figure 9 shows the Jacobi speed evaluated across the surface of Arrokoth, assuming a uniform density of 235 kg/m^3 (our nominal Arrokoth density, justified in Section 7.1). This figure (unsurprisingly) shares many similarities with plots of the geopotential and geopotential elevation (Figures 5 and 6). The Jacobi speed is defined to be zero at the highest geopotential, which is on the equator of the big lobe (Figures 9b and 9d), and maximizes in the neck with speeds of ∼1.45 m/s (with an area-weighted mean Jacobi speed is 0.95 ± 0.21 m/s). In other words, a particle traveling freely without friction from the geopotential high on the large lobe would arrive at the neck with a speed of 1.45 m/s. The Jacobi speed would be the exact arrival speed if the particle traveled ballistically (i.e., was launched from the initial starting position and landed at the neck), and an upper limit if the particle traveled across the surface by sliding or rolling (as friction would remove energy). For a larger density of 500 kg/m^3, the Jacobi speeds would be larger: peaking at 2.56 m/s (with an area-weighted mean of 1.52 ± 0.47 m/s).

4.7. The Roche Lobe

The gravitational influence of Arrokoth extends beyond its surface, and investigation of the geopotential surrounding Arrokoth can provide important insight about particle motion around the body including defining the speed

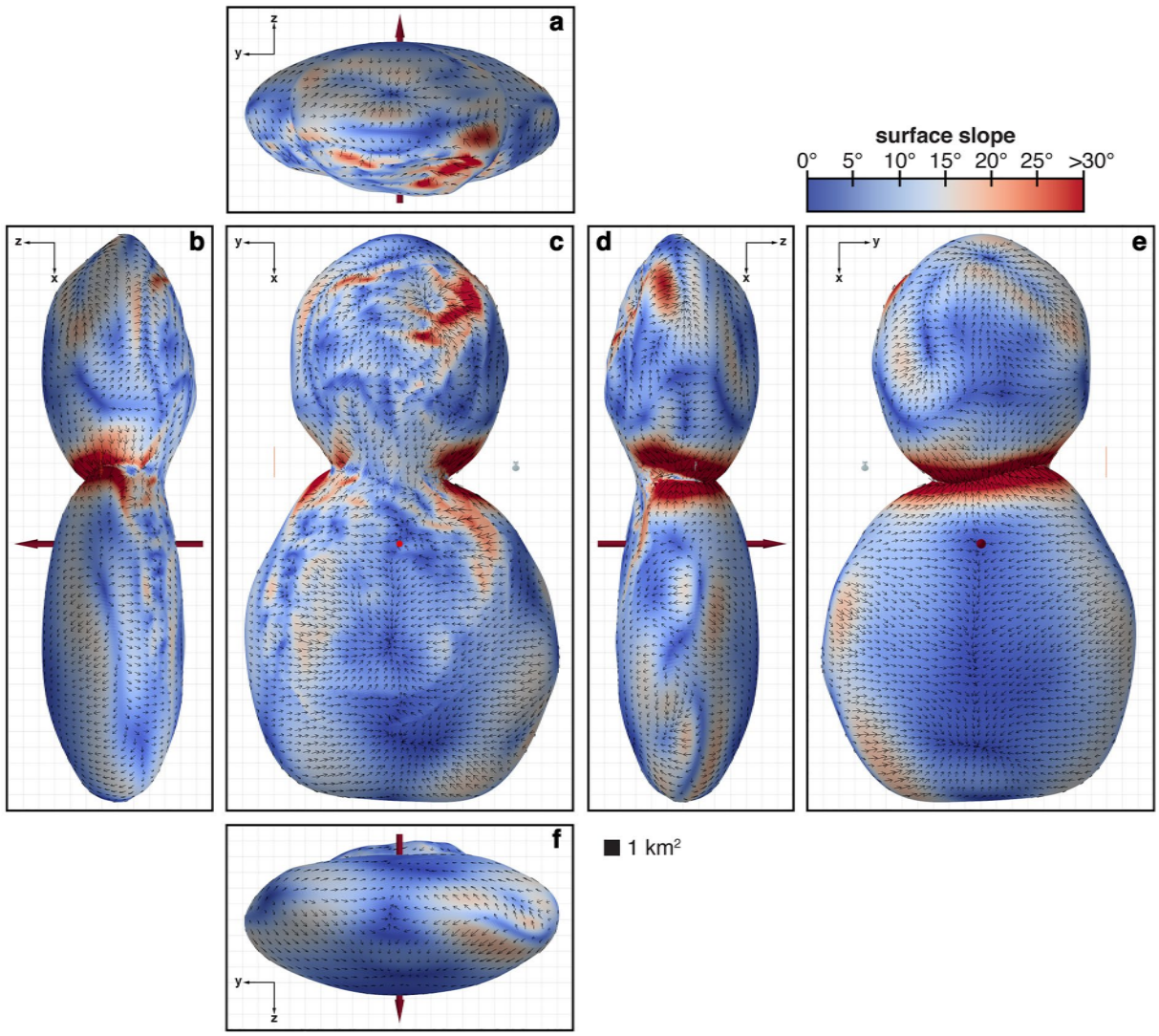

Figure 8. Surface slopes across the surface of (486958) Arrokoth. Vectors indicate the downslope direction. Views (a–f), the background grid, and symbols are described in Figure 4.

limits for particles impacting or escaping Arrokoth's surface. Figure 10a shows contours of the geopotential (Equation 8, Sections 4.4) evaluated in the space around Arrokoth. Equilibrium points—places where the gravitational and centrifugal accelerations balance—can be identified by solving $\nabla U(\vec{r}) = \vec{0}$. For the Arrokoth shape model, four equilibrium points exist above the surface: two saddle points off the bow and stern of Arrokoth ("x" and square symbols in Figure 10), and two center points off of the port and starboard sides of Arrokoth (triangle symbols in Figure 10). Equilibrium points are often critical for understanding orbital motion about small bodies, and equilibrium points can either be stable or unstable (Scheeres, 2012). We leave the investigation of orbital stability around Arrokoth for future work.

The Roche lobe is defined as the geopotential that has the same energy as the minimum geopotential equilibrium point ("x" in Figure 10). The Roche lobe separates the space where particles are bound to Arrokoth: particles initially at rest on the surface of Arrokoth, but outside of the Roche lobe have sufficient potential energy to reach the equilibrium point and escape Arrokoth, while particles within the Roche lobe do not and are trapped on Arrokoth unless they are provided additional energy to reach the Roche lobe and escape (Sections 4.8).

For the nominal density of Arrokoth (235 kg/m^3, justified in Section 7.1), the Roche lobe intersects the surface of Arrokoth. This behavior is not uncommon for small bodies, and small, rapidly rotating asteroids in particular—

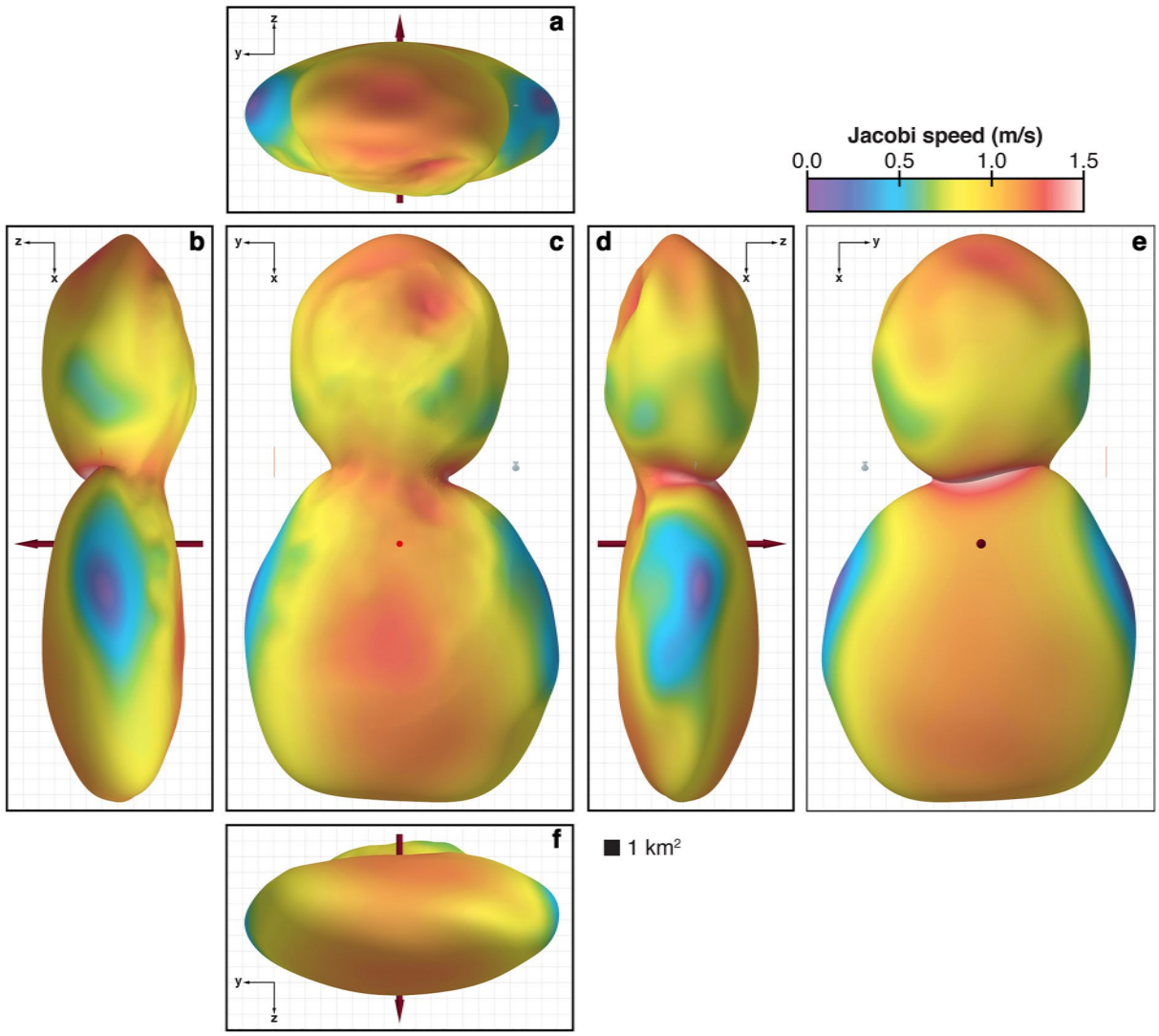

Figure 9. Jacobi speed across the surface of (486958) Arrokoth. Views (a–f), the background grid, and symbols are described in Figure 4.

like (101955) Bennu (Scheeres et al., 2016, 2019) and (66391) Moshup (provisional designation: 1994 KW4; Scheeres, 2015). Regions enclosed by the Roche lobe are natural places for trapping mobile surface material. On Bennu, the regions within the Roche lobe have a characteristically lower slope (11.7° within the Roche lobe, compared to 18.4 outside of the Roche lobe), which has been interpreted to reflect mass wasting (Scheeres et al., 2019). This is *not* observed on Arrokoth for the nominal density of 235 kg/m^3; the mean slopes within the Roche lobe are 10.1 ± 9.9°, compared to 10.6 ± 5.1° outside of the Roche lobe, and 10.4 ± 7.5° for the entire body. However, as described in Section 5, there may be some interesting correlations between the Roche lobe and surface features.

Arrokoth's unique bilobate shape complicates interpretation of the Roche lobe. It is possible to have particles sitting on the surface of the big lobe, with a geopotential equal to (over even exceeding) the Roche lobe energy, but are nonetheless trapped on Arrokoth because the small lobe physically obstructs the pathway to the minimum geopotential equilibrium point and subsequent escape from Arrokoth. For example, consider point "P" identified in Figure 10a. Point "P" lies on the traditional Roche lobe (the pink envelope in Figure 10a). If a particle at "P" was dislodged, it would have sufficient energy to travel anywhere within the Roche lobe—theoretically including the minimum geopotential equilibrium point (the "x" in Figure 10a) where it could escape the body. However, the Roche lobe intersects the surface of the small lobe, meaning that there is no real path for that particle to actually

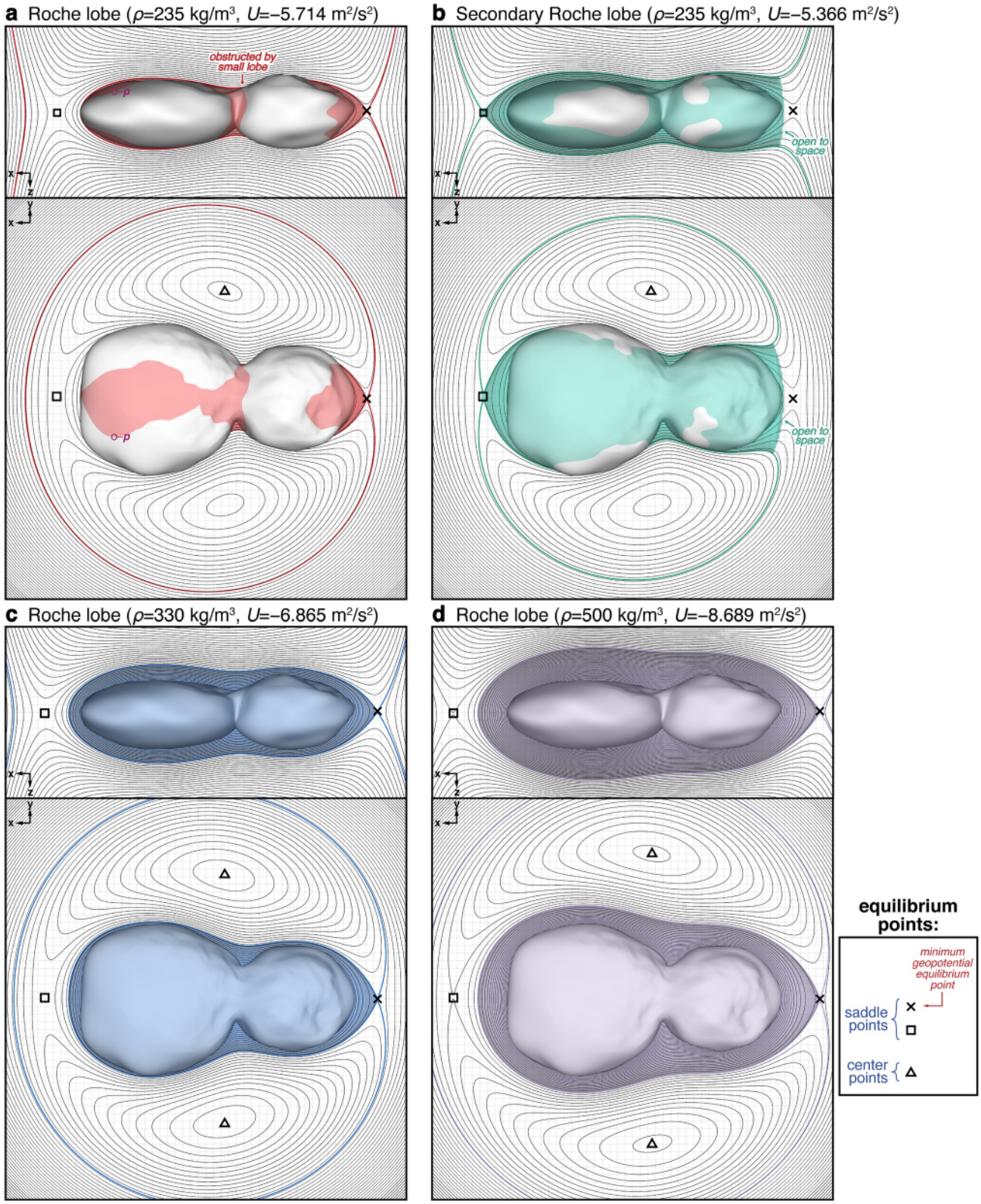

Figure 10.

reach the equilibrium point. Thus, a particle from "P" would require additional energy to escape than what is predicted from the classic Roche lobe calculation. The configuration of Arrokoth means that particles on the big lobe would require additional energy to clear the small lobe and escape—and even then, the pathways past the small lobe are restricted. Instead, what may be more likely, is that particles with sufficient energy would escape via the second lowest geopotential equilibrium point. We define the geopotential surface with this energy as the "secondary" Roche lobe (Figure 10b). The net result of this unusual bilobate shape is that particles on the big lobe require more energy to leave Arrokoth than those on the small lobe. This could result in each lobe having different histories of mass transport and loss. These peculiarities only occur if Arrokoth has a low density (as inferred in Sections 7.1). If Arrokoth has a density above 330 kg/m^3, the Roche lobe moves further away from the surface of Arrokoth, and completely encloses it—often hugging within 1 km of the surface (Figure 10c). For yet higher densities, like 500 kg/m^3 (Figure 10d), the Roche lobe encloses Arrokoth at greater and greater distances.

As shown in Figure 10, the geophysical environment of Arrokoth extends into the surrounding space—and would play a critical role in dynamics of possible dust and satellites in the vicinity of Arrokoth. We do not consider orbital dynamics of such hypothetical objects further, although other groups have performed preliminary analyses (e.g., Rollin et al., 2021).

4.8. Escape Speed

To understand the conditions under which material may leave Arrokoth, it is useful to consider two end-members: the minimum escape speed (v_{me}), and the guaranteed escape speed (v_{ge}).

As discussed in Section 4.7, particles outside of Arrokoth's Roche lobe have sufficient potential energy to reach the lowest energy equilibrium point and escape Arrokoth, while particles within the Roche lobe do not. Following Equation 14, we can calculate the speed necessary for a particle within the Roche lobe to reach the Roche lobe, which we define as the minimum escape speed, v_{me}:

$$v_{me}(\vec{r}) = \sqrt{-2\left(U(\vec{r}) - U_{Roche}\right)}, \tag{15}$$

where U_{Roche} is the geopotential of the Roche lobe (-5.714 m^2/s^2 for the nominal density; Figure 10). Figure 11 shows the minimum escape speed across the surface of Arrokoth. The minimum escape speed is defined as zero outside of the Roche lobe, because particles outside of the Roche lobe have sufficient potential energy to escape without any additional energy. The minimum escape speed is also sometimes referred to as the return speed (Scheeres, 2012; Scheeres et al., 2016), as it also represents the minimum speed at which a particle falling from infinity can hit the surface. For the nominal density of 235 kg/m^3, the minimum escape speeds peaks at 1.03 m/s (with an area-weighted mean of 0.46 ± 0.17 m/s, within the region where the minimum escape speed is greater than zero). For this density, only 42.5% of the surface is within the Roche lobe and has a non-zero minimum escape speed (Figure 10a). For a larger density of 500 kg/m^3, the entire surface is within the Roche lobe (Figure 10d) and has a non-zero minimum escape speed ranging from 2.11 to 3.31 m/s (with an area-weighted mean of 2.62 ± 0.27 m/s).

While the minimum escape speed is a threshold required for escape, it is not guaranteed that particles launched with the minimum escape speed will escape Arrokoth. For example, a particle launched off the surface with the minimum escape speed could still be placed on a trajectory where it re-impacts the surface before making it to the minimum geopotential equilibrium point. Additionally, as discussed in Section 4.7 (and the case of point "P" in Figure 10), being outside of the Roche lobe does not guarantee the existence of a path off the body.

Figure 10. Roche lobes of (486958) Arrokoth. Contours indicate surfaces of constant geopotential in 0.1 m^2/s^2 intervals. Colored contours and surfaces correspond to the Roche lobe. "x," square, and triangle symbols correspond to equilibrium points. Triangles correspond center equilibrium points. The point "P" identified in panel (a) is an example point on the surface, and is discussed in the text. Top panels shows a starboard elevation of Arrokoth, with contours evaluated in the $x-z$ plane at $y = 0$; bottom panels shows a ventral plan of Arrokoth, with contours evaluated in the $x-y$ plane at $z = 0$. (a) Geopotential and Roche lobe assuming a uniform density of 235 kg/m^3. (b) The secondary Roche lobe (the geopotential surface that intersects the second-lowest geopotential equilibrium point) assuming a uniform density of 235 kg/m^3. (c) The Roche lobe assuming a uniform density of 330 kg/m^3—which is the density at which the Roche lobe completely encloses Arrokoth. (d) The Roche lobe assuming a uniform density of 500 kg/m^3. Views (a–f), the background grid, and symbols are described in Figure 4.

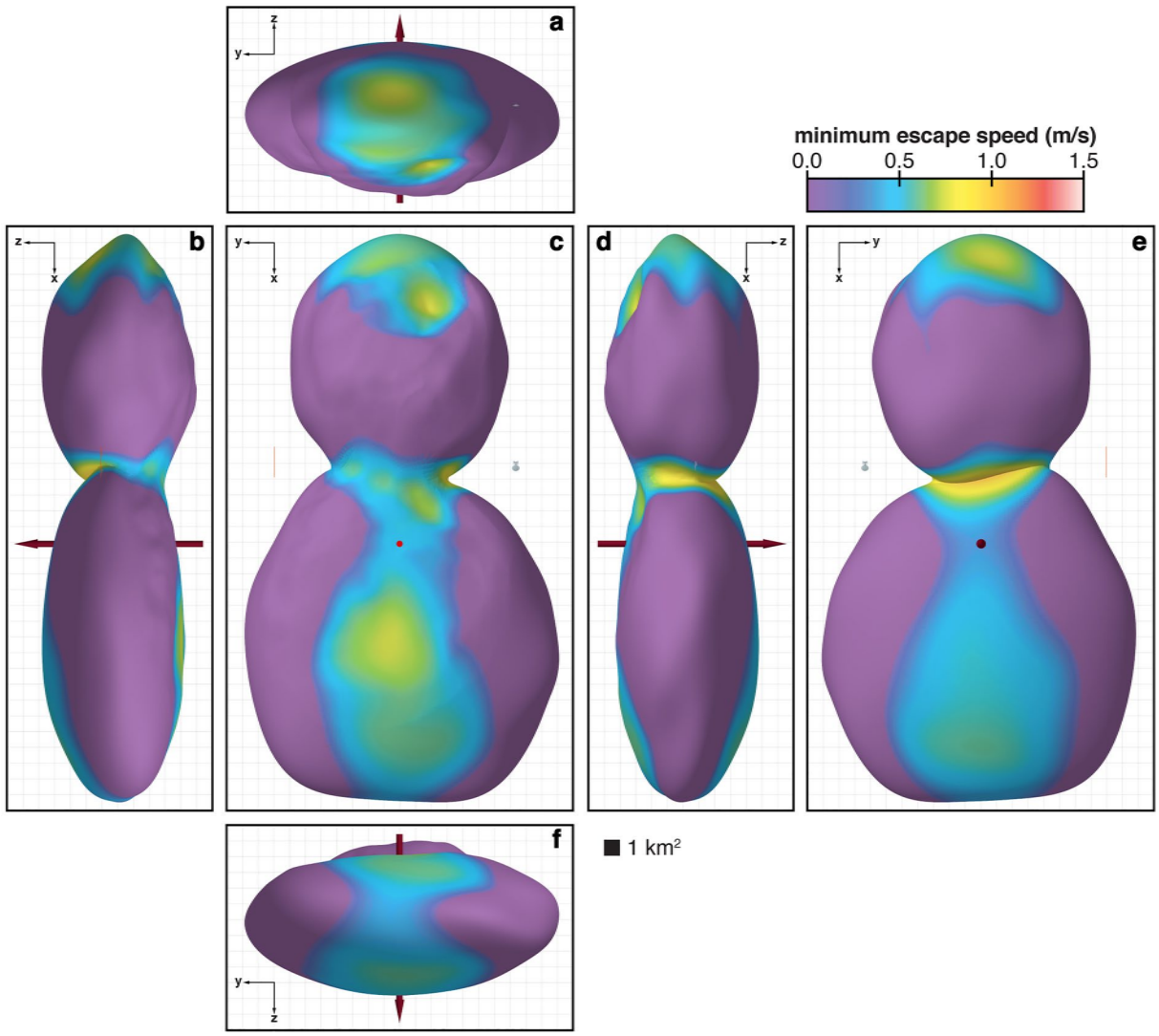

Figure 11. Minimum escape speed (or return speed) across the surface of (486958) Arrokoth. Views (a–f), the background grid, and symbols are described in Figure 4.

A more practical approach to determine the escape speed is to calculate the velocity required for a particle launched with an energy greater than or equal to $\sqrt{U(\vec{r})}$—which guarantees that it has sufficient energy to leave Arrokoth's geopotential well. Accounting for the inertial rotational speed of the asteroid ($\vec{v}_{inertial} = \vec{\omega} \times \vec{r}$, the guaranteed escape speed, v_{ge}, can be written (Scheeres, 2012)):

$$v_{ge}(\vec{r}) = -\vec{n}(\vec{r}) \cdot (\vec{\omega} \times \vec{r}) + \sqrt{(\vec{n}(\vec{r}) \cdot (\vec{\omega} \times \vec{r}))^2 + 2U(\vec{r}) - (\vec{\omega} \times \vec{r})^2}. \quad (16)$$

Figure 12 shows the guaranteed escape speed across the surface of Arrokoth. For the nominal density of 235 kg/m^3, the guaranteed escape speeds across the surface of Arrokoth range from 1.1 to 4.2 m/s (with an area-weighted mean of 2.9 ± 0.6 m/s). For a higher density of 500 kg/m^3, the guaranteed escape speeds across the surface of Arrokoth increase, ranging from 2.6 to 5.6 m/s (with an area-weighted mean of 4.4 ± 0.6 m/s). Figure 12 highlights the importance of Arrokoth's rotation in escape of material; particles from Arrokoth's leading side (where surface normals, $\vec{n}(\vec{r})$, are more closely aligned with the inertial rotational speed, $\vec{v}_{inertial}$) benefit from Arrokoth's rotation an have lower guaranteed escape speeds than on the trailing side.

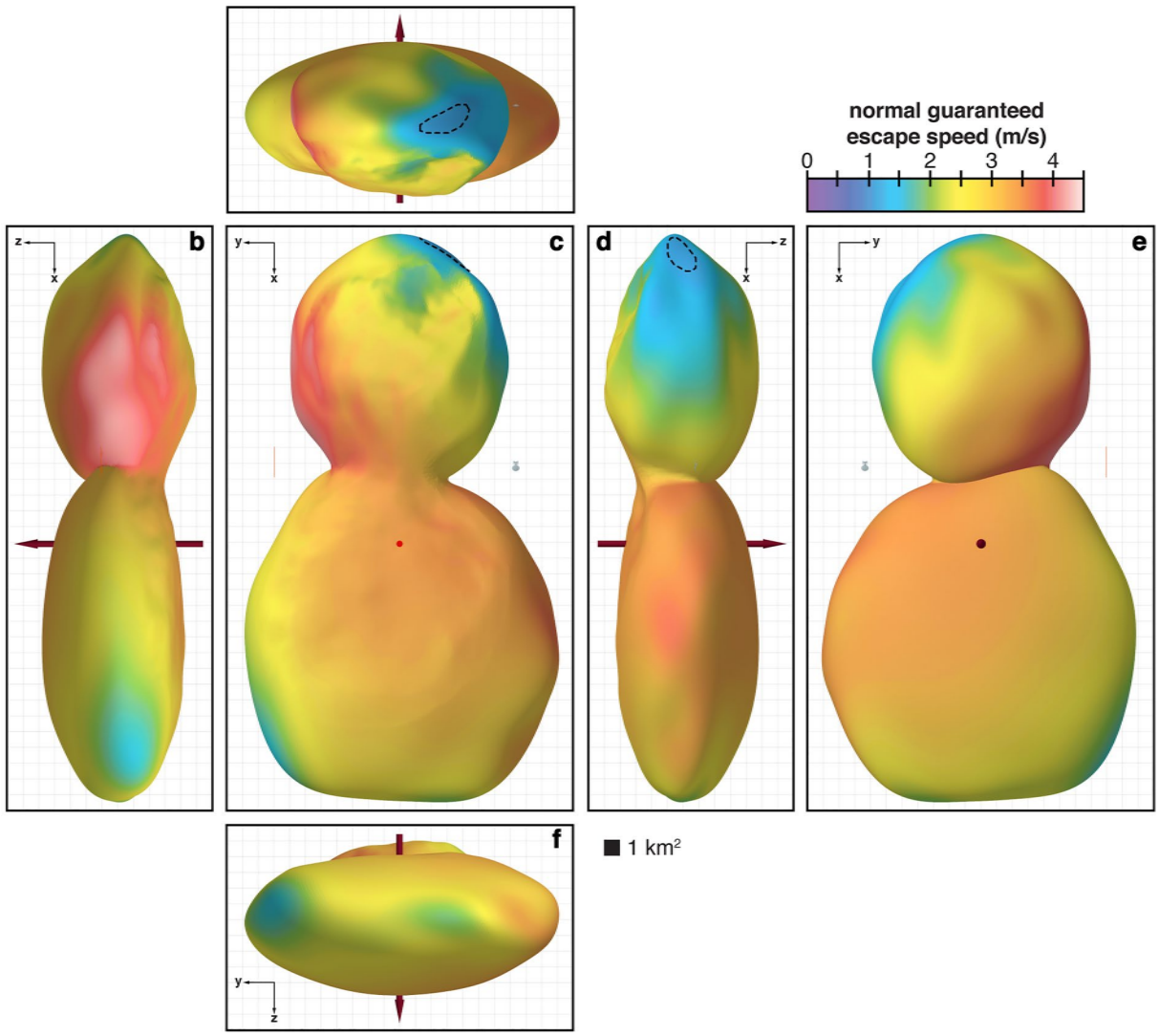

Figure 12. Normal guaranteed escape speed across the surface of (486958) Arrokoth. The dashed contour indicates the region where the Jacobi speed exceeds the normal guaranteed escape speed, as described in the text. Views (a–f), the background grid, and symbols are described in Figure 4.

It is interesting to compare the guaranteed escape speed with the Jacobi speed, which describes the maximum speed a particle could achieve if sliding (or flying) across the surface of Arrokoth (Section 4.6, Figure 9). Across most of the surface of Arrokoth, the Jacobi speed is less than the guaranteed escape speed—except on the leading distal edge of the small lobe (a region enclosed by a dashed contour in Figure 12, best visible in Figure 12a). At first glance, the existence of a region where the Jacobi speed exceeds the guaranteed escape speed may suggest that particles sliding across the surface may be ejected if they reach this region. However, there are multiple reasons to disregard this. First, the Jacobi speed is calculated with reference to the maximum geopotential on Arrokoth—which occurs on the port and starboard sides of the large lobe (Figure 6). Thus, particles can only achieve the Jacobi speed if they start at these specific locations. For a particle to reach the putative ejection zone in Figure 11a, they would need to traverse almost the entire length of Arrokoth without losing energy—which is implausible. (Such a scenario would either require sliding with near zero friction, or bouncing with very high coefficient of restitution with a minimal loss of energy. Both of these scenarios are highly contrived.) Second, and more subtly, the guaranteed escape speed is calculated assuming particle velocities are normal to the surface, whereas particles sliding down the surface at the Jacobi speed would necessarily have their particle motions more closely parallel to the surface. While there may be scenarios where the Jacobi speed could be translated from being surface-parallel to surface normal (e.g., if the sliding particle bounces or ramps off the surface), this makes

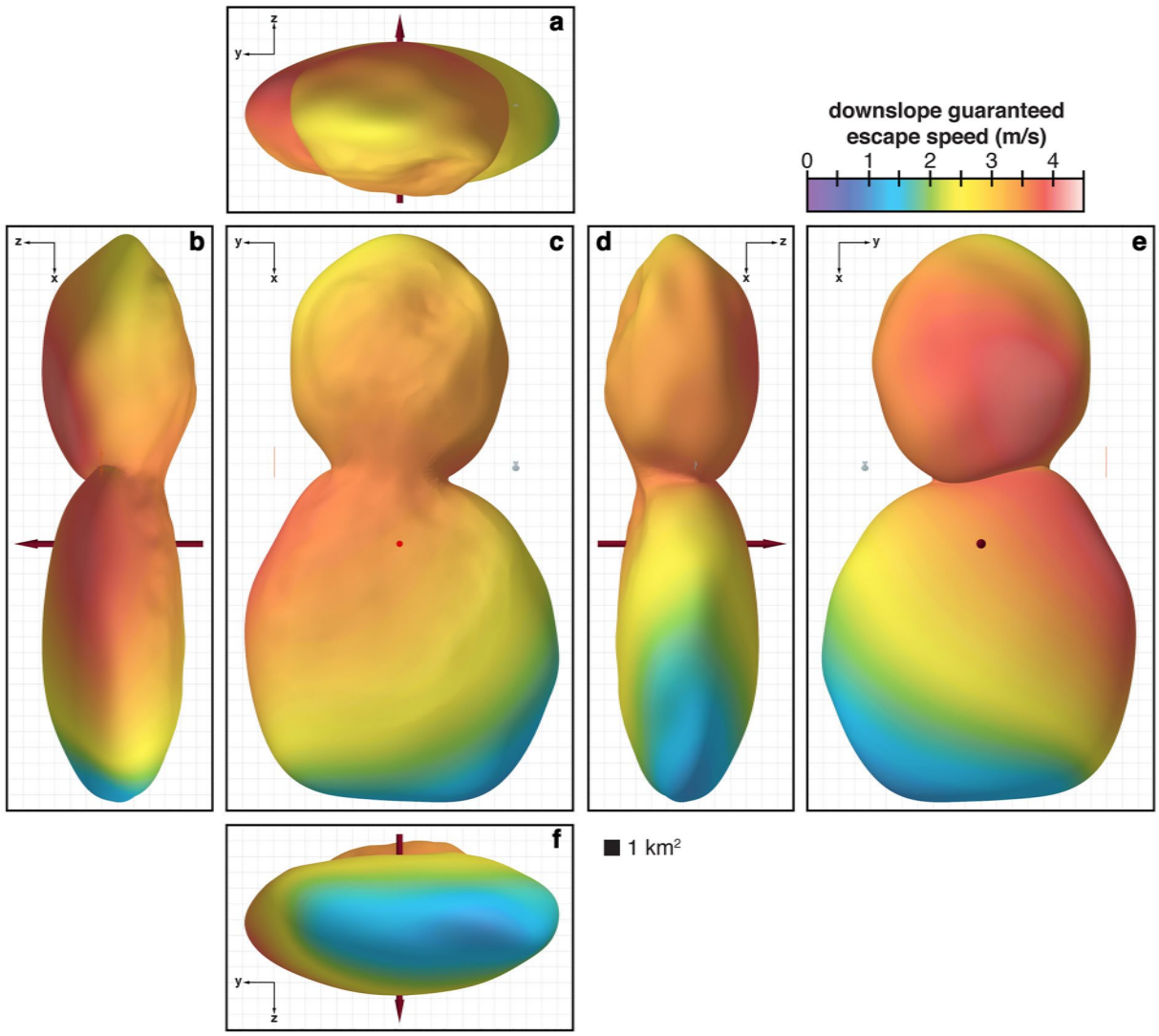

Figure 13. Downslope guaranteed escape speed across the surface of (486958) Arrokoth. Views (a–f), the background grid, and symbols are described in Figure 4.

the comparison not completely appropriate. To demonstrate this effect, we recalculated the guaranteed escape velocity assuming that the velocity would be aligned with the downslope direction, $\vec{s}(\vec{r}) = \vec{a}(\vec{r}) - \vec{a}(\vec{r}) \cdot \vec{n}(\vec{r})$, instead of the surface normal, $\vec{n}(\vec{r})$. This downslope guaranteed escape speed is shown in Figure 13. The downslope guaranteed escape speed has a characteristically different, almost mirrored pattern compared to the (normal) guaranteed escape speed because the downslope directions $\vec{s}(\vec{r})$ and normal directions $\vec{n}(\vec{r})$ are orthogonal to each other. Most importantly the downslope guaranteed escape speeds on Arrokoth are always less than the Jacobi speeds—never exceeding 90% of the Jacobi speed at any given location. For the nominal density of 235 kg/m^3, the downslope guaranteed escape speeds across the surface of Arrokoth range from 1.1 to 4.0 m/s (with an area-weighted mean of 3.0 $\pm$ 0.7 m/s). For a higher density of 500 kg/m^3, the downslope guaranteed escape speeds across the surface of Arrokoth increase, ranging from 2.4 to 5.5 m/s (with an area-weighted mean of 4.4 $\pm$ 0.7 m/s). In both the normal and downslope guaranteed escape speed calculations, we do not consider whether the resulting escape trajectory would re-impact Arrokoth—which it almost certainly would in the convex regions of the neck. Downslope movement is treated in slightly more detail in Section 6. We do not consider orbital dynamics in the vicinity of Arrokoth, although other groups have performed preliminary investigations of such behavior (e.g., Rollin et al., 2021).

5. Implications for Arrokoth's Geology

The geophysical quantities described in Section 4 likely play a role in the wide array of geologic processes on Arrokoth. In this section, we describe the relationships between features observed on the surface of Arrokoth, and the inferred geophysical environment. These relationships can be best appreciated by viewing the geophysical model of Arrokoth in the same geometry as the highest resolution *New Horizons* image of Arrokoth, as shown in Figure 14. Throughout this section, we will refer to geologic units described in Spencer et al. (2020) and select locations of interest (L1–L11), both shown in Figure 14b. At present, there are three officially named features on Arrokoth (Figure 1): (a) Sky (formerly, informally named "Maryland"), which is the large, putative impact crater on the small lobe; (b) Akasa is the bright neck region; and (c) Ka'an is the quasi-circular annulus of bright material on the face of the large lobe.

5.1. Bright Material

The surface of Arrokoth is mottled by complex albedo patterns (Hofgartner et al., 2021; Spencer et al., 2020; Stern et al., 2019, 2021)—the most conspicuous of which are bright materials (unit *bm*), including Arrokoth's bright neck (L1) and the two bright spots on the small lobe (L2) located within Sky. These were among the first albedo features identified during the approach imaging. It should be noted that these terrains are only bright in a relative sense; the average reflectance of Arrokoth is ∼25%, while the brightest material has a reflectance of ≲45% (Hofgartner et al., 2021).

As shown in Figure 14, the neck (L1) and bright materials within Sky (L2) correspond to geopotential lows (Spencer et al., 2020; Stern et al., 2019, 2021). The brightest material on Arrokoth is within its neck (Hofgartner et al., 2021; Stern et al., 2021), which corresponds to some of the lowest geopotentials on Arrokoth. However, not all bright materials are located in geopotential lows. For example, small (≲1 km) circular bright spots are observed across the entire surface of Arrokoth (Schenk et al., 2021), including in geopotential highs (e.g., L3). The bright spots may represent pits like those observed near the terminator of Arrokoth at lower phase angles (unit *sp*; e.g., L4; Schenk et al., 2021)—just appearing different due to the different illumination conditions across Arrokoth (pits are predominantly observed near the terminator where the insolation angle is high and surface relief is accentuated, and bright spots are found in regions where the insolation angle is low and surface albedo contrasts are accentuated). Unfortunately, none of the bright spots or pits are well-resolved in the merged shape model (Figure 14c), although they are resolved in some stereo analyses (Schenk et al., 2021). If the bright spots are indeed unresolved pits, they would correspond to *local* geopotential lows, again supporting the inference that bright material tends to be found in geopotential lows.

While the most notable bright materials on Arrokoth are associated with geopotential lows (the neck and bright spots in Sky), not all geopotential lows are associated with bright material. The central "face" of the large lobe (unit *sm*, L5 in Figure 14b) represents a global geopotential low (Figures 5, 6 and 14d), yet it is not brighter than the surrounding terrains. Additionally, while the bright spots within Sky (L2) are closely associated with a geopotential low, the bright spots are not associated with the lowest geopotentials within Sky—but are instead on the interior slopes of the putative crater. In fact, the dark crater material within Sky (unit *dc*) is more closely associated with the geopotential low. Unlike the small pits and bright spots, these regions (the face of the large lobe and Sky) are large and well-resolved features in the merged shape model, so the lack of correlation likely cannot be explained by inadequate resolution. Thus, whatever process that results in bright materials being found in geopotential lows does not operate uniformly across Arrokoth. These correlations are discussed further in Section 5.4.

5.2. Arrokoth's "Hat"

The distal end of Arrokoth's small lobe is characterized by unique rough terrain (unit *rm*, L11 in Figure 14b), surrounded by darker, mottled terrain (unit *mm*; Spencer et al., 2020). This region is colloquially referred to as Arrokoth's "hat" or "skull cap," and is rough and pitted at the scale of a few hundred meters. Spencer et al. (2020) described this region as a "facet" on the small lobe, although this is not reflected in the merged shape model (Figure 14c). Nonetheless, this region has an interesting relationship with Arrokoth's modeled geophysical quantities. The hat is a local geopotential high (Figure 14d), but surrounded by a geopotential low "moat." This region

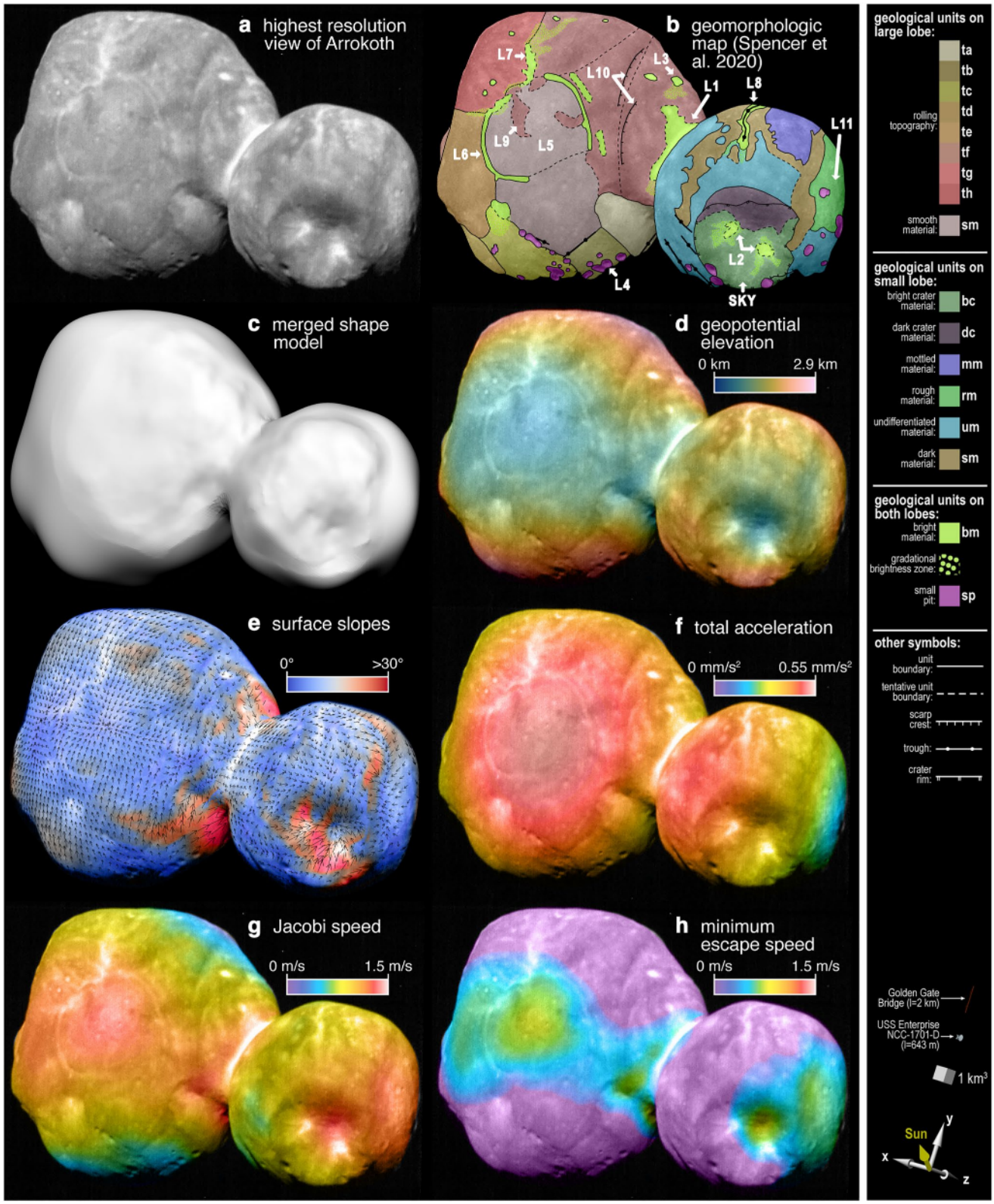

Figure 14.

is also one of the areas enclosed within Arrokoth's Roche lobe (Figure 10a), meaning that this region may naturally trap loose, bright material, as discussed further in Sections 5.4 and 6.

5.3. Curvilinear Features

Arrokoth's surface is also bisected by networks of narrow ($\lesssim$0.5 km wide) curvilinear features (Schenk et al., 2021; Spencer et al., 2020; Stern et al., 2019, 2021). In some cases, these curvilinear features are associated with bright materials (unit *bm*, L6–L8 in Figure 14b), dark materials (L9), and in other cases these features appear to represent structural features (i.e., scarps) rather than distinct albedo features (L10). These curvilinear features have complicated and inconsistent relationships to geophysical quantities: some curvilinear features appear well-aligned with the downslope direction (L7 and L9); some curvilinear features appear orthogonal to the downslope direction, roughly tracing contours of equipotential (L6); and other curvilinear features appear at breaks in slope (L8). It is unclear if these patterns arise from a single process, or multiple processes, as discussed in Section 5.4.

5.4. What Causes the Correlations (and Anti-Correlations) Between Observed Geology and Geophysical Environment?

The peculiar and sometimes inconsistent correlations between observed geology and inferred geophysical environment are challenging to explain.

The simplest hypothesis is that bright material represents mobilized surface material that has moved downslope and collected in geopotential lows (i.e., mass wasting; Grundy et al., 2020; Spencer et al., 2020; Stern et al., 2019, 2021). This hypothesis readily explains the occurrence of bright material within geopotential lows (e.g., L1, L2, and L3 if it represents an unresolved pit), material aligned with downslope directions (e.g., L7, and the more diffuse deposits around L2), and potential material orthogonal to downslope directions—if they represent regions where downslope-moving material piles up, akin to a debris-fan (L6). While this hypothesis may explain several observed phenomena, it does not explain them all. For example, L9 is a *dark* patch that may be consistent with a down-slope deposit. It remains unclear why these patterns are not observed globally. Perhaps downslope movement is triggered by stochastic processes (e.g., small impacts, seismic shaking) that do not uniformly affect the body. Alternatively, perhaps Arrokoth's surface properties (e.g., regolith thickness, composition, etc.) vary across the body.

Thermal processes, including sublimation, may also play a role in shaping Arrokoth's geology (Grundy et al., 2020; Katz & Wang, 2021; Lisse et al., 2021; Spencer et al., 2020; Steckloff et al., 2021; Stern et al., 2019; Umurhan et al., 2022; Zhao et al., 2021). Since thermal processes also depend sensitively on shape and spin, there is some ambiguity between whether geophysical or thermophysical processes control Arrokoth's geology. For example, Arrokoth's bright neck is not only a geopotential low, but it is also a place on Arrokoth that sees less sky—reducing the incident flux of solar photons and cosmic rays (but also increasing the flux of re-radiated photons from the surrounding terrain), which may affect surface processes (Umurhan et al., 2022). The alignment of some of Arrokoth's pits in pit chains is reminiscent of pit chains like those seen on Pluto's Sputnik Planitia, which may be formed by sublimation or surface collapse (Moore et al., 2017). Some of the "crenulated" textures on Arrokoth's small lobe may be indicative of scarp retreat via sublimation (Moore et al., 2020; Spencer et al., 2020). At present, the relative balance between these processes is uncertain. Lisse et al. (2021) and Steckloff et al. (2021) suggest that sublimation was most important in the first 10–100 Myr of Arrokoth's existence, very early in its history.

Figure 14. Geophysical environment of Arrokoth through the lens of *New Horizons*. Orthographic views of Arrokoth in the same viewing and illumination geometry as the highest-resolution *New Horizons* image of Arrokoth (LORRI CA06; Figure 1). In the Arrokoth reference frame (Section 2), this viewing geometry corresponds to a sub-spacecraft latitude and longitude of 51.0°S, −176.7°E, and a subsolar latitude and longitude of 61.9°S, 125.2°E. In panels (b and d–h), the data set is draped over the image of Arrokoth. (a) The highest resolution *New Horizons* view of Arrokoth (CA06 LORRI, processed by Tod Lauer). (b) Geomorphologic map of Arrokoth, as described in Spencer et al. (2020). Locations of interest describe in the text are indicated by labels L1–L11. Colors and symbols for the geologic map are shown on the right. (c) The merged shape model of Arrokoth. While the illumination geometry is accurate, Arrokoth's reflectance properties (e.g., phase function) are not intended to be accurate. (d) Geopotential elevation (as in Figure 6). e, surface slopes and downslope vectors (as in Figure 8). (f) Total accelerations on the surface (as in Figure 4). (g) Jacobi speed (as in Figure 9). (h) Minimum escape speed (as in Figure 11). Regions with non-zero minimum escape speed are within the Roche lobe (as in Figure 10).

The partial annulus of bright material on the "face" of the large lobe, Ka'an (L6), is a particularly intriguing case study for evaluating different hypotheses. Spencer et al. (2020) speculated that Ka'an may represent the "suture" of the original building blocks of Arrokoth, surficial mass wasting deposits (as hypothesized above), or structural features. Our new calculations of Arrokoth's geophysical environment provide critical new context for this feature. First, the Ka'an annulus partially encloses the geopotential low on the face of the large lobe (Figure 14d). Second, the Ka'an annulus is largely orthogonal to the downslope direction, nearly tracing an equipotential surface (Figure 14e). Third, the Ka'an annulus shares some similarities to the intersection of the Roche lobe with the surface of Arrokoth for the nominal density (Figure 10a), corresponding to the location where the minimum escape speed is 0 m/s (Figures 9 and 14h). The first two observations are consistent with the basic downslope mass-wasting hypothesis described above: bright material slides downslope from the distal ends of Arrokoth (producing downslope features like L7), but then stop moving downslope as they reach the geopotential low and the slope decreases below some threshold. Details of this downslope motion are discussed in more detail in the following section (Section 6). The third observation, however, presents a new twist on this hypothesis. When the Roche lobe intersects the surface of the body, it can result in peculiar geology—as best demonstrated by asteroid (101955) Bennu. Bennu is a small (0.52 km diameter), rapidly rotating, top-shaped asteroid explored by the *OSIRIS-REx* mission. Bennu's Roche lobe intersects its surface: its equatorial region is enclosed within the Roche lobe, while the polar regions are outside of the Roche lobe. The equatorial regions of Bennu have lower slopes, and are thought to represent regions where down-slope moving material is trapped, unable to escape the body (Scheeres et al., 2016, 2019). Perhaps similar behavior occurs on Arrokoth–where material flows "down" from the distal ends of the large lobe and then is trapped within the Roche lobe. Not only does this material deposit in this region, but it becomes dynamically trapped, unable to escape Arrokoth. Barring other processes, material would naturally accumulate in this region, smoothing it out (although, as noted in Section 4.5, the slopes in this region are not distinct from slopes elsewhere on Arrokoth). Perhaps Ka'an is a physical demarcation of this boundary, although it is unclear what would create such a sharp boundary. In addition to controlling motion of material across the surface of Arrokoth, the Roche lobe is also critical for determining the orbital dynamics of material around Arrokoth. Perhaps impacts and other processes launch Arrokoth material on suborbital trajectories that are then focused in certain regions related to observed surface features. While intriguing, it is important to note that the Roche lobe only intersects the surface of Arrokoth for densities less than 330 kg/m^3 (Figure 10); at higher densities, Arrokoth is fully enclosed by the Roche lobe. Moreover, while Ka'an is reminiscent of the intersection of the Roche lobe, it is not a perfect match. As shown in Figure 14h, the Roche lobe generally only conforms to part of the Ka'an annulus. To create a better match would require decreasing the density of Arrokoth even further. While this potential connection between surface features and Arrokoth's Roche lobe are intriguing, it may be simply coincidence.

Arrokoth's hat (Section 5.2) has a similar relationship to the Roche lobe as Ka'an, meaning that many of the same hypotheses may extend to this feature as well. However, the "hat" has a different geologic expression. It is unclear whether these different expressions are the result of observing similar features at different viewing geometries (the hat is viewed at higher phase angle than Ka'an), or if these are truly different features.

In summary, Arrokoth's surface markings are complicated, and while many are associated with the geophysical environment, the exact relationship and geologic mechanisms at play remain elusive. It is curious to note that Arrokoth's albedo patterns and geologic units are more discrete (i.e., possessing sharper boundaries) than geophysical quantities derived from the merged shape model, like geopotential or slope. It is possible this complex correlation may be an artifact of the finite resolution of the shape model, and that unresolved topography may lead to sharper boundaries. For example, Arrokoth's pits are not well-resolved in these shape models (although they are resolvable in other topography analyses; Schenk et al., 2021), and there may be other sub-kilometer-scale features affecting what we see. However, it is also possible that there are other geologic processes are at play. Most notably, thermal processes—including the sublimation sculpting of the surface—may play an important role in shaping Arrokoth. Interpretation of these features on Arrokoth are challenging since it remains unclear what the bright material represents, be it freshly exposed and un-weathered material, material with a different composition, or something else entirely (Grundy et al., 2020; Spencer et al., 2020; Stern et al., 2021). This analysis is further complicated, as the available color imaging data is insufficient to conclusively determine if the bright material is associated with a different composition (Grundy et al., 2020).

5.5. What Causes Arrokoth's Principal Axes to Be Aligned?

One of the most curious results from the *New Horizons* flyby of Arrokoth was that not only is Arrokoth a contact binary, but that the principal axes of inertia of the two lobes (and the overall body) are very nearly parallel to one another (Section 4.2; Figure 3; McKinnon et al., 2020; Stern et al., 2019). Our analysis of the merged shape model confirms previous analyses focusing solely on the global shape model (McKinnon et al., 2020), including that the probability of such alignment from chance is exceptionally low (0.01% chance; Section 4.2).

The alignment of principal axes is a natural hallmark of tidal locking, as this configuration reduces the total energy in an orbiting binary. The general hypothesis is that Arrokoth started as a separated binary, where the two components became tidally locked, and then slowly spiraled together and merged (Grishin et al., 2020; McKinnon et al., 2020). Alternatively, even if the two components weren't tidally locked before merger, this aligned configuration is the lowest energy configuration for two bodies if they are close spinning apart (Hirabayashi et al., 2020). One could imagine the two lobes merging in some other configuration (say, with the small lobe sitting "on top" of the large lobe), but then reorienting to adjust to the lowest energy configuration. The configuration of Arrokoth's two lobes (and the fact that it is in this lowest energy configuration) can be used to constrain the density of Arrokoth (Section 7; Hirabayashi et al., 2020).

5.6. Arrokoth's Flattening

Another striking feature of Arrokoth is the overall flattening of the body and the individual lobes (McKinnon et al., 2020; Spencer et al., 2020; Stern et al., 2019). This flattening can be quantified by the ratio between the polar and equatorial radius, ϵ, which can be estimated from the dimensions of the bounding box enclosing each lobe of Arrokoth: $\epsilon \approx \Delta_z/\Delta_x$ (where Δ_z and Δ_x are reported in Table 1). For the large lobe, $\epsilon \sim 1/2$; for the small lobe, $\epsilon \sim 2/3$ (McKinnon et al., 2020).

The smooth, flattened, lenticular shape of Arrokoth's two lobes has led to speculation that Arrokoth's shape may represent some equilibrium figure (i.e., the shape a strengthless, fluid body responding solely to self-gravity, rotation, and tides would take). Equilibrium figures have a rich history of study (e.g., Chandrasekhar, 1969), and there has been substantial work in recent decades to extend this work with additional physics (e.g., internal strength), and apply it to small Solar System bodies, including asteroids, comets, and small satellites (e.g., Descamps, 2008, 2010, 2015; Gnat & Sari, 2010; Holsapple, 2001, 2004; Minton, 2008; Sharma, 2015, 2016). If the shape of Arrokoth (or its lobes) were consistent with an equilibrium figure, it may suggest that this unusual shape is the result of its formation—particularly its bulk properties, spin, and potential evolution as a separated binary that ultimately merged. McKinnon et al. (2020) note that that the overall shape of Arrokoth is not consistent with an equilibrium figure (particularly Roche ellipsoids), but the individual lobes could be consistent with strengthless oblate bodies (Maclaurin spheroids), if their shape records a slight faster spin periods between 12 and 14 hr. While Arrokoth's shape is reminiscent of an equilibrium figure, it is important to note that its surface does not conform to an equipotential (McKinnon et al., 2020). This is well-demonstrated in Figure 10, where equipotential contours (including the Roche lobe) can be seen to intersect the body.

An alternative hypothesis for the origin of Arrokoth's shape is that it originated from sublimative sculpting of the body (Zhao et al., 2021). Zhao et al. (2021) modeled the loss of volatile ices (e.g., CH_4) from Arrokoth, assuming that Arrokoth formed initially as a contact binary with more spherical components, and that it maintained its orbital and spin state over Solar System history. They found that erosion from sublimation can naturally yield flattened, Arrokoth-like objects—as long as the body's obliquity remains near ~90°. The efficacy of this process depends on the stability of Arrokoth's spin and orbit configuration, and the composition of Arrokoth, including the abundance, properties, and condition of dust and ice.

One approach for exploring the enigmatic origin of Arrokoth's flatness is to determine if this flattening is characteristic of other small KBOs. As *New Horizons* leaves the Solar System, it is observing and characterizing a variety of other KBOs. Thus far, these observations have revealed previously unseen close binaries (Weaver et al., 2022), characterized their orbits (Porter, Spencer, et al., 2022), photometric properties (Verbiscer et al., 2022), spins and shapes (Porter, Verbiscer, et al., 2022). These new observations, coupled with models, may shed light on the origin of Arrokoth's flatness.

6. Sliding on Arrokoth

The calculations described above only represent a static "snapshot" of the forces and accelerations acting on the surface of Arrokoth. Particle motion on the surface of small, irregular bodies is notoriously complex and non-intuitive. To explore this behavior, we developed a simple model for particle motion on the surface of Arrokoth. Utilizing a simple Eulerian integration scheme, the equations of motion for a particle sliding across the surface of Arrokoth are:

$$\begin{aligned} \vec{v}_1 &= \vec{v}_0 + \vec{a}_p(\vec{r}_0)\ dt \\ \vec{r}_1 &= \vec{r}_0 + \vec{v}_1\ dt, \end{aligned} \tag{17}$$

where 0 and 1 indicate an subsequent time-steps separated by time dt, $\vec{r}$ is the location of the test particle, $\vec{v}$ is velocity of the particle (equivalent to $\vec{v}$ in Equation 7 and elsewhere), and $\vec{a}_p(\vec{r})$ is the acceleration acting on the particle in the plane of the surface:

$$\vec{a}_p(\vec{r}) = \vec{a}_\star(\vec{r}) - \left(\vec{a}_\star(\vec{r}) \cdot \vec{n}(\vec{r})\right) \vec{n}(\vec{r}), \tag{18}$$

where $\vec{a}_\star(\vec{r})$ is the total acceleration acting on the sliding particle and $\vec{n}(\vec{r})$ is the local surface normal. The total acceleration acting on the sliding particle, $\vec{a}_\star(\vec{r})$, is similar to the total acceleration previously written as $\vec{a}(\vec{r})$ (Equation 7), although it is modified with an additional frictional drag term appropriate for sliding across the surface:

$$\vec{a}_\star(\vec{r}) = \left(\nabla U_G(\vec{r})\right) + \left(\vec{\omega} \times \vec{\omega} \times \vec{r}\right) + \left(2\vec{v} \times \vec{\omega}\right) + \left(\dot{\vec{\omega}} \times \vec{r}\right) + \left(\vec{a}_f\right). \tag{19}$$

The five terms in large parentheses correspond to the gravitational acceleration, centrifugal acceleration, Coriolis acceleration, acceleration due to changes in the Arrokoth's rotation rate, and acceleration due to frictional sliding. Here, we neglect any changes of Arrokoth's rotation with time (i.e., $\dot{\vec{\omega}} = 0$), so we set the fourth term to zero. The frictional drag term, $\vec{a}_f$, is defined as:

$$\vec{a}_f(\vec{r}, \vec{v}) = \mu\, |\vec{a}_n(\vec{r})|\, \frac{\vec{v}}{|\vec{v}|}, \tag{20}$$

where $\vec{a}_n$ is the component of the total acceleration normal to the surface (i.e., the weight: $\vec{a}_n(\vec{r}) = \vec{a}_\star(\vec{r}) - \vec{a}_p(\vec{r})$), and μ is the coefficient of kinetic friction. In this formulation, we assume that particle motion is confined to the surface of the Arrokoth shape model, and never leave the surface—precluding hopping motion. Velocities are conserved as particles move between facets of the shape model. With the inclusion of modest amounts of friction ($\mu = 0.1$), particles never reach escape velocities.

This model has a number of simplifying assumptions that could be debated, including the use of an Eulerian integration scheme, the lack of hopping or rolling motion, assumptions about surface friction and long-range transport of material, and the basic assumption that mass wasting can be treated by looking at the motion of individual particles across a rigid surface. Nonetheless, this approach does provide a useful, exploratory first look at motion across the surface of Arrokoth that can be later investigated using more robust methodologies.

Figure 15 shows two example outputs from this simple model for sliding motion across the surface of Arrokoth. At first glance, these models reinforce the knowledge gained from looking at the surface slopes of Arrokoth (Figures 8 and 14e): material is expected to move from the geopotential highs (low latitudes) to the geopotential lows (high-latitudes, including the face of the large lobe, the neck, Sky, and near the "hat" on the small lobe). However, these more detailed models also reveal interesting phenomena not captured in the static slope calculation. First, Figures 15a and 15b reveal that the Coriolis force may be important for understanding particle motion on Arrokoth. When neglecting the Coriolis force (Figures 15a and 15d), material slides straight to the geopotential lows, including the central "face" of the large lobe. When accounting for the Coriolis force (Figures 15b and 15e), material can be deflected eastward (clockwise in the view of Figure 15b)—just like the winds of a cyclone on Earth (it is tempting to call this phenomenon a "regolith cyclone."). A similar effect has been proposed to explain some features (4) Vesta. Otto et al. (2016) proposed that curved radial ridges within the south polar Rheasilvia impact structure formed by Coriolis force acting on mass wasting during the initial Rheasilvia crater collapse. For this process to work on Arrokoth, the material moving downslope would need to

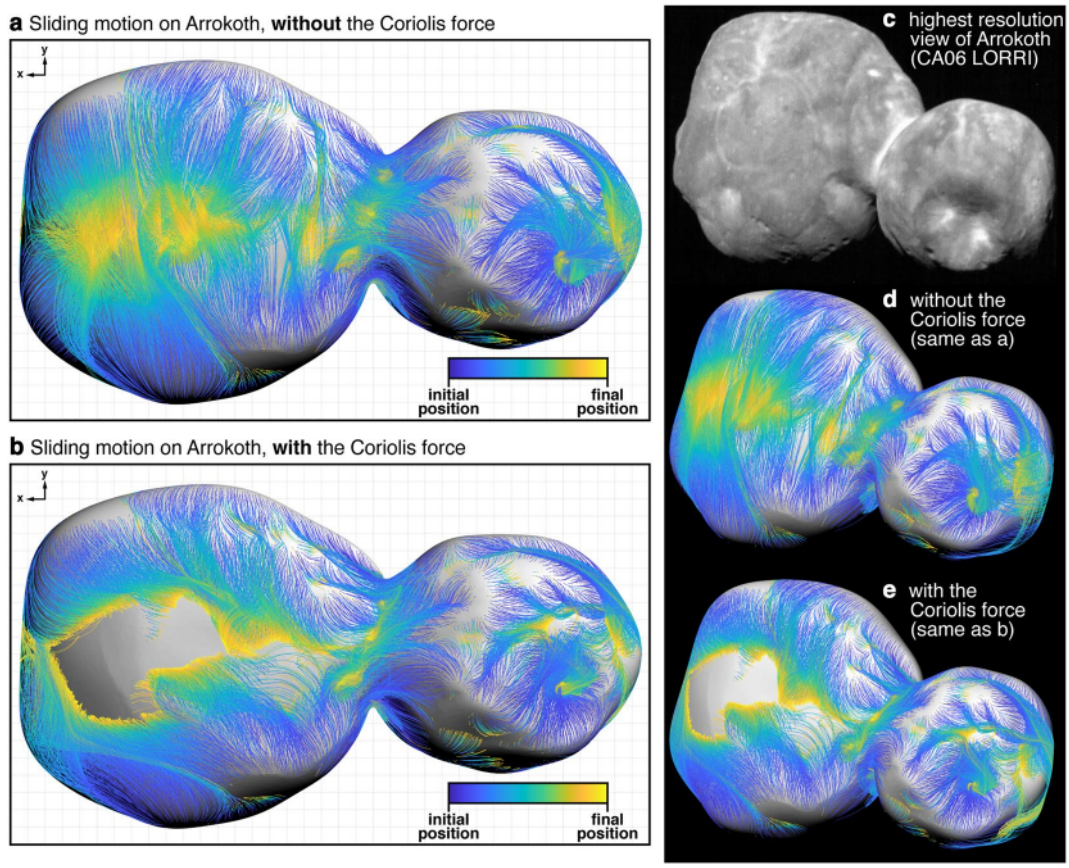

Figure 15. Sliding motion across the surface of (486958) Arrokoth. (a) Orthographic view of the ventral (*New Horizons* encounter) side of Arrokoth, showing the trajectories of particles moving across the surface of Arrokoth. Particles initially start at rest, and move in response to the gravitational, centrifugal, and frictional forces ($\mu = 0.1$). This calculation omits the Coriolis force. Initial starting positions are uniformly spaced on an 200-m x–y grid across the surface of Arrokoth. Trajectories are colored by the normalized distance from the starting point (blue indicates initial location and yellow indicates final location). Background grid and other symbols are described in Figure 2. Panle (b) same as panel (a), but including the Coriolis force. Panels (c–e) shows the highest resolution image of Arrokoth (CA06 LORRI), and the results from panels (a) to (b) in the same viewing geometry.

travel large distances at moderate speeds—such that the Coriolis accelerations (which is proportional to velocity, $\vec{v}$, in Equations 7 and 19) are comparable to other accelerations. While intriguing, it is not obvious (and perhaps unlikely) that this would occur on Arrokoth.

Even though this process is speculative, deflection of downslope material by the Coriolis force provides an intriguing explanation to some of Arrokoth's surface features—particularly the anomalous partial annulus of bright material, Ka'an, on the face of the large lobe (L6 in Figure 14, described in Section 5). If material moved downslope toward the central "face" of the large lobe with sufficient speed, the Coriolis force would deflect the material, conceivably confining mass-wasting in an annulus. For this process to occur, material would need to move at relatively high velocities (comparable to, but not above, the Jacobi speed) over long distance. Such speeds would only be feasible if there was very low friction between the sliding material and the surface. We performed qualitative tests and found that such long-range, deflected motion would only occur for very low coefficients of friction ($\mu \lesssim 0.2$). While a low coefficient of friction is conceivable (e.g., Perinotto et al., 2015), the plausibility depends sensitively on material properties—which are generally uncertain for Arrokoth. This type of behavior may be important for understanding mass wasting on other small bodies where travel distances are large compared to the size of the body, and the Coriolis and gravitational forces can be comparable. A more thorough investigation of this behavior is left to future work.

Despite the potential complexity and assumptions of this model, this analysis demonstrates that static quantities, like slope, do not completely capture the full range of regolith processes on small bodies. Complex downslope movement can change where material is deposited (and how much material is deposited there). A simple calculation of mass flux (discharge) based on hill slopes alone would not capture this behavior.

7. Arrokoth's Density

7.1. Inferring Arrokoth's Density

All of our inferences about Arrokoth's geophysical environment (Sections 4) depend critically on the assumed density of Arrokoth. As discussed in Sections 2.6, *New Horizons* did not directly measure the mass or density of Arrokoth. In this section, we examine the different constraints on Arrokoth's density, and why we favor our nominal density of $\rho = 235$ kg/m^3.

7.1.1. Density Constraints From Assumptions of Arrokoth's Strength

Since the *New Horizons* flyby, there have been multiple attempts to use different assumptions of Arrokoth's mechanical strength to constrain its density. These approaches generally rely on the assumption that material strengths of comets are an appropriate analog to Arrokoth. Stern et al. (2019), Spencer et al. (2020), and McKinnon et al. (2020) placed a lower-bound on Arrokoth's density of $\rho \gtrsim 250$ kg/m^3 by assuming that the neck is under compression and not tension. (The argument is equivalent to saying that the two lobes are only *barely* bound, with a rotational velocity just below the mutual orbital velocity if they two lobes were barely separated and orbiting a common center of mass.) Lower densities could be allowed if the neck has some tensile strength; however, tensile strengths for comets are generally very low, and do not greatly increase the plausible density range. McKinnon et al. (2020) additionally placed an upper-bound for the density based on the structural integrity of Arrokoth's neck. Assuming the typical inferred strengths of comets, Arrokoth's density would need to be $\rho \lesssim 500$ kg/m^3 to prevent faulting and collapse of the neck. For even the largest inferred cometary strengths, this density limit increases to $\rho \lesssim 1{,}250$ kg/m^3. While these constraints are important, it is important to note that the mechanical properties of comets are poorly constrained, and it is unclear how analogous Arrokoth is to the comets studied in detail in the inner solar system, which are presumably highly processed.

7.1.2. Density Constraints From the Configuration of Arrokoth's Lobes

Hirabayashi et al. (2020) placed an additional constraint on the density of Arrokoth by investigating how the formation of the Sky impact crater would affect Arrokoth's structure. Again assuming cometary strengths, Hirabayashi et al. (2020) concluded that the Sky impact would likely break Arrokoth's neck, resulting in the reconfiguration of Arrokoth. Based on the configuration of the two lobes of Arrokoth, and Arrokoth's present rotation rate, they found that Arrokoth's density must be between between $300 \lesssim \rho \lesssim 500$ kg/m^3. At higher densities (or slower rotation rates), Arrokoth would have reconfigured to place the small lobe on the short axis of the large lobe, rather than long axis as observed today (Figure 3). While this density constraint is motivated by considerations of the strength of Arrokoth's neck (like those in McKinnon et al., 2020; Spencer et al., 2020; Stern et al., 2019), it is important to note that Hirabayashi et al.'s ultimate density constraint is independent from the strength estimates; instead relying solely on the configuration of Arrokoth's two lobes and arguments based on conservation of angular momentum and minimization of rotational kinetic energy.

7.1.3. Density Constraints From the Distribution of Arrokoth's Slopes

The final method for constraining Arrokoth's density comes from analysis of its geopotential and slopes. On some small bodies, it is reasonable to assume that certain geologic features conform to equipotentials, and use that knowledge to infer the density of the body. For example, the density of comet 103P/Hartley was estimated by assuming that the smooth "waste" between its two lobes conformed to an equipotential surface (A'Hearn et al., 2011). Similar methods have been used to infer the different densities of the two lobes of asteroid (25143) Itokawa from analysis of its smooth terrains (Kanamaru et al., 2019). However, there are no features or regions on Arrokoth that unambiguously trace equipotential surfaces. Nonetheless, even in the absence of clear slope indicators, the distribution of modeled surface slopes across the entire body can provide useful constraints on Arrokoth's density. Richardson and Bowling (2014) and Richardson et al. (2019) have shown that the shapes of many asteroids and cometary nuclei conform to configurations of maximum topographic stability and minimum internal stress. It is hypothesized that these configurations result

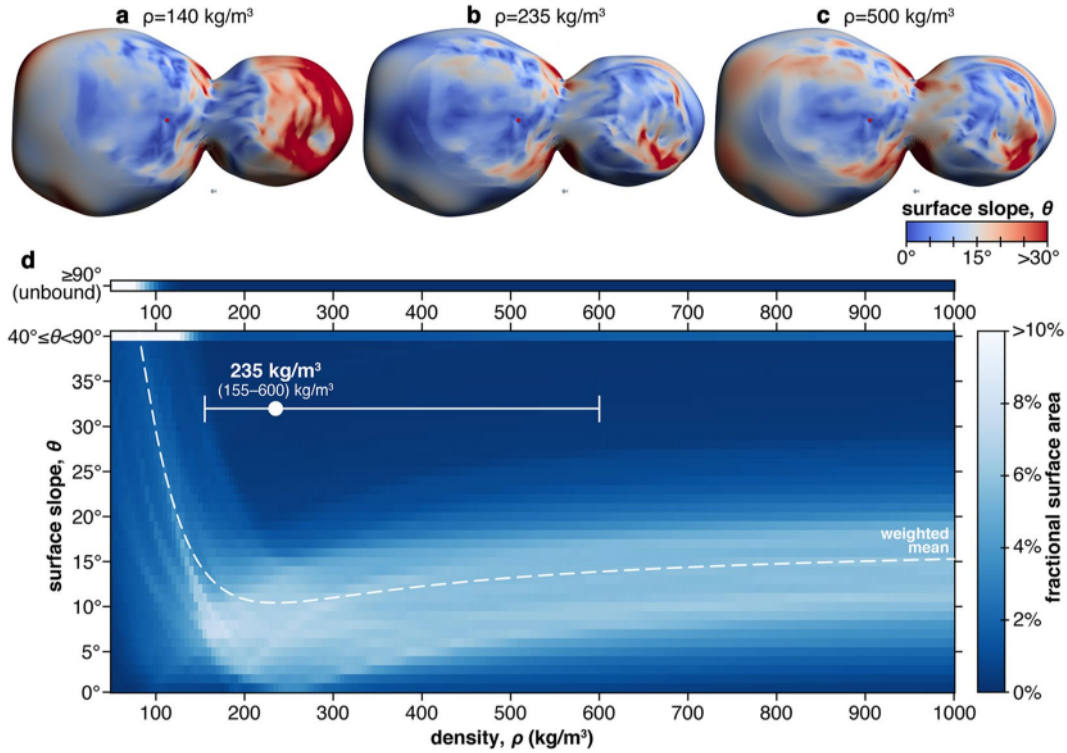

Figure 16. Inferring the density of (486958) Arrokoth from the distribution of surface slopes. Panels (a–c) show orthographic views of the *New Horizons* encounter side (ventral side) of Arrokoth, colored by surface slope, for three different densities: 140, 235, and 500 kg/m^3, respectively. Panel (b) is identical to Figure 8c. Panel (d) shows the fraction of Arrokoth's surface as a function of slope and the assumed density. Each column can be thought of as a histogram of slopes across the entire surface of Arrokoth for a different density. The white dashed line shows the mean of the slope (weighted by surface area), which minimizes at a density of 235 kg/m^3, corresponding to the inferred density of Arrokoth. Additional plots of slopes and geopotential as a function of density can be found in Figure S2 in Supporting Information S1.

from a self-correcting feedback where downslope movement of regolith (triggered by impacts, outgassing, and other processes) works to erode topography on small bodies toward equipotential surfaces, although this process rarely runs to completion since erosion rates decrease as slopes decrease. The practical result of this feedback is that it minimizes the distribution of the surface slopes and variations of geopotential on the object. Moreover, the exact state is sensitive to the rotation rate and density of the body, such that any increase or decrease of its density or rotation rate increases the variations in the surface slopes and geopotential. If we assume that Arrokoth is subject to these same feedbacks as other small bodies, we can use its shape model to constrain its density. This method was first applied to Arrokoth in Spencer et al. (2020) and (McKinnon et al., 2020), and we investigate it in more detail here.

Figures 16a–16c shows the slopes across the surface of Arrokoth for three different assumed bulk densities: 190 and 235 kg/m^3 (the nominal density, shown in more detail in Figure 8), and 500 kg/m^3 (the assumed density in McKinnon et al., 2020; Spencer et al., 2020; Stern et al., 2019). From inspection of Figures 16a–16c, it is clear that that the slopes tend to be higher in both the low density (190 kg/m^3) and high density (500 kg/m^3) cases. This relationship can be explored in more detail by examining the distribution of slopes for a range of different densities, as shown in Figure 16d. The mean slope is minimized for a density of $\rho = 235$ kg/m^3, and the mean slope increase for both higher and lower densities. This behavior can be understood qualitatively: at low densities, rotational accelerations (which are orthogonal to the spin vector of Arrokoth) dominate over gravitational accelerations, resulting in steep slopes and even mass loss on the distal edges of Arrokoth (where slopes can exceed 90°); at high densities, gravitational accelerations dominate over rotational accelerations, and the small deviation from an ideal bilobate equipotential shape (e.g., Descamps, 2015) manifest as steeper slopes. Following the hypothesis of Richardson and Bowling (2014) and Richardson et al. (2019), this minimum in the slope distribution corresponds to the actual density of Arrokoth. While we highlight trends between mean slope and density, similar patterns are observed in the distribution of other geophysical quantities (Figure S2 in Supporting

Information S1). Richardson and Bowling (2014) have demonstrated that this approach is capable of retrieving the densities for the small number of asteroids and comets for which we posses both shape models and direct measurements of density from gravity measurements.

While the analysis of Arrokoth's slopes clearly indicates the optimal density of Arrokoth (ρ = 235 kg/m^3, Figure 16), it is less clear how to determine the uncertainty of the density. Richardson and Bowling (2014) determined error ranges using a modified full-width at half-maximum approach: they identified the asymptote of the function at high density (red lines in Figure S2 in Supporting Information S1), and define the error-bounds as the densities halfway between that asymptote and the minimum of the quantity in question. Applying this method to Arrokoth's slope distribution yields a density of ρ = 235 (155–600) kg/m^3, where the quantity in parentheses corresponds to the 1σ uncertainty range. This optimal density is largely independent of whether it is derived from the mean slope or other geophysical quantities (Figure S2 in Supporting Information S1). While we use this method for determining uncertainties, we note that this approach may not be statistically rigorous. The quantities used (e.g., mean slope) are not probability distribution functions, and thus cannot strictly be used in this way. A more rigorous investigation of this methodology is warranted in future work.

If this slope-adjusting feedback is indeed active on Arrokoth, it has some interesting implications for Arrokoth's geologic history. This process is dynamic, meaning that reaching the present configuration of Arrokoth may involve substantial material transport, which in turn alters the body's shape, gravity field, and inertia tensor. While it remains unclear how extensive this process was for Arrokoth, this emphasizes the need for more detailed investigations of the dynamic feedbacks that may shape small KBOs.

7.1.4. Summary of Density Constraints

In summary, despite the lack of direct measurements of Arrokoth's density, different methods for inferring Arrokoth's density suggest a low density—with estimates ranging between 155 and 1,250 kg/m^3, with a preference for densities between 200 and 500 kg/m^3. Each of these different estimates are based on different assumptions which may or may not be appropriate to Arrokoth, for example, that it possesses comet-like material properties (Section 7.1.1), or has regolith behavior similar to comets and asteroids (Section 7.1.3). Throughout this paper, we opt to use the density derived from the analysis of Arrokoth's slopes, 235 (155–600) kg/m^3, as our nominal density of Arrokoth. While the amplitudes of many derived geophysical quantities depend on the density, the qualitative trends of most geophysical quantities discussed in this paper are largely independent of density variations within this range. The only notable exception is that higher densities move the Roche lobe further from the surface of Arrokoth (Figure 10d), making it harder for material to leave Arrokoth (as discussed in Section 4.7).

While at least three different methods suggest an low density for Arrokoth, it is important to note that these approaches are not completely independent. All three are dependent on the shape model. Densities derived from assumptions about Arrokoth's strength (Section 7.1.1) depend on the cross-sectional area Arrokoth's neck and the relative volumes of the two lobes. Densities derived from the configuration of Arrokoth's (Section 7.1.2) depend on being able to determine the principal axes of the two lobes. Densities derived from surface slopes (Section 7.1.3) depend explicitly on the shape model. Because of this degeneracy, if the shape model were to change, the densities derived from these techniques would also change.

7.2. Arrokoth's Inferred Low Density in Context

The inferred density of Arrokoth, 235 (155–600) kg/m^3, is very low. For comparison, this inferred density is comparable to freshly fallen snow (10–260 kg/m^3; Judson & Doesken, 2000) or snowpack (310 kg/m^3; King et al., 2020). If accurate, this density would be one of the lowest densities measured for a planetary body, and it would have important implications for the formation and evolution of small bodies across the solar system. Figure 17 and Table S1 in Supporting Information S1 show the density of Arrokoth compared to the densities of a variety of potential solar system analogs.

The pre-encounter assumption was that Arrokoth would have a density comparable to comets—between 500 and 1,000 kg/m^3—owing to their presumed similar origin and composition (Moore et al., 2018). This assumption led to the fiducial density of 500 kg/m^3 used in Stern et al. (2019), Spencer et al. (2020), and McKinnon et al. (2020). While comets have a mean density of ∼500 kg/m^3, they are generally associated with large uncertainties (green points in Figure 17; Table S1 in Supporting Information S1). Only one comet density has been precisely determined

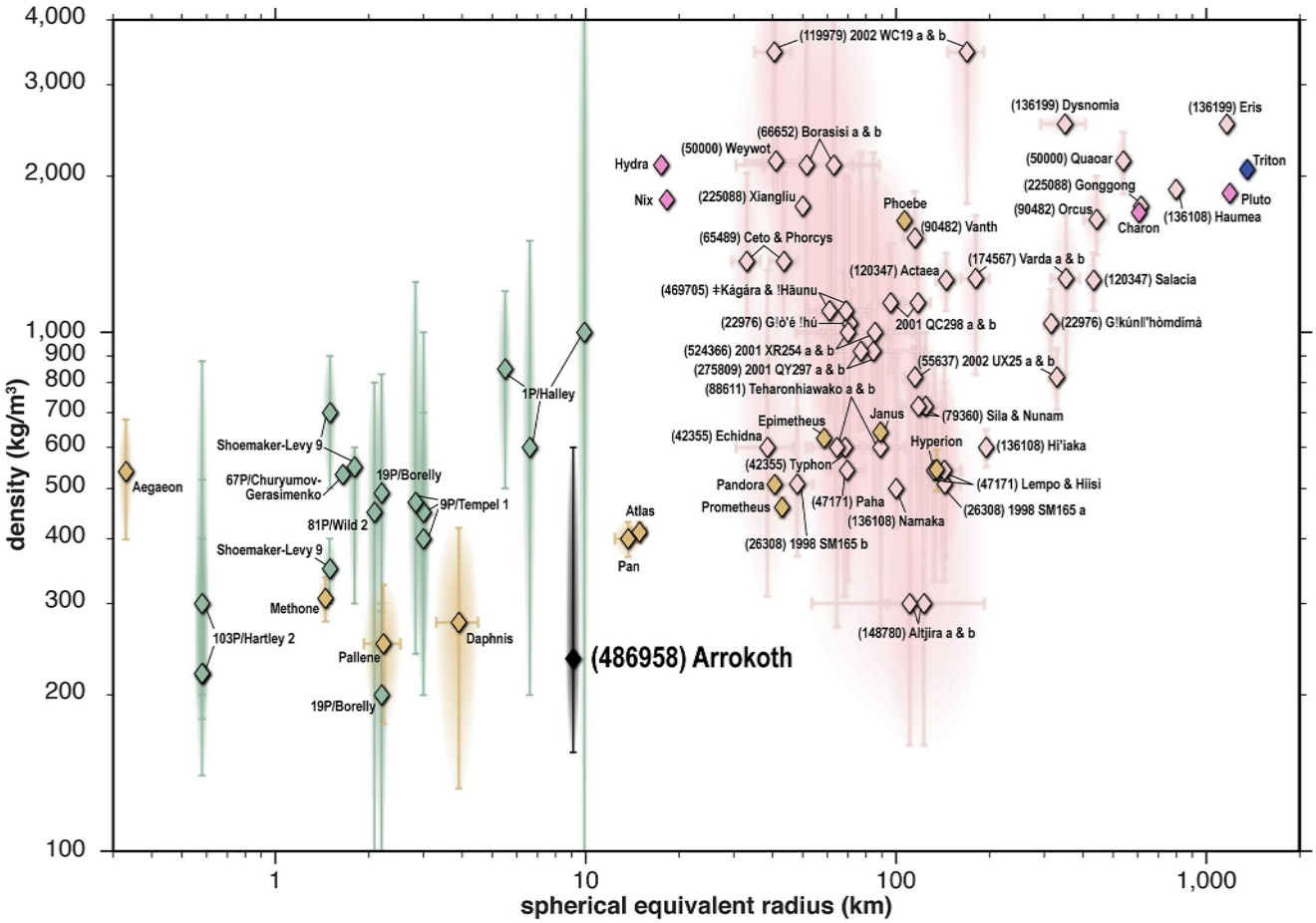

Figure 17. Sizes and densities of icy bodies across the solar system. Data values are from Table S1 in Supporting Information S1. Points are colored by object type: Kuiper Belt Objects are pink (objects in the Pluto system are dark pink, and Neptune's moon Triton—likely a captured Kuiper Belt Object—is purple), comets are green, Saturn's small ring moons are yellow, and Arrokoth is black. Error bars and the semi-transparent ellipses indicate 1σ uncertainties. The density estimate for Arrokoth is based on the analysis of its slopes (Section 7.1.3).

by gravity science measurements: 67P/Churyumov-Gerasimenko by the *Rosetta* mission (ρ = 532 (525–539) kg/m^3; Jorda et al., 2016; Pätzold et al., 2016). The densities of all other comets have been inferred from less direct means. The most common method for measuring comet densities is from measuring how non-gravitational forces and outgassing perturb the comet's motion, although some cometary densities have been constrained by using the same slope and geopotential minimization method we use for Arrokoth (Section 7.1.3), including 9P/Tempel (P. C. Thomas, A'Hearn, Belton, et al., 2013), 19P/Borrelly (Farnham & Cochran, 2002), and 103P/Hartley (A'Hearn et al., 2011; P. C. Thomas, A'Hearn, Veverka, et al., 2013; Richardson & Bowling, 2014). Overall, cometary densities range from as low as 200 kg/m^3 (19P/Borrelly) to 1,000 kg/m^3 (1P/Halley), although the distribution is dominated by inferences, assumptions, and uncertainties. While Arrokoth's inferred density is consistent with the lower end of the distribution of comet densities, the associated uncertainties make it challenging to make meaningful comparisons. Additionally, there may be other reasons that comets have different densities than Arrokoth. First, all comets with density constraints are smaller than Arrokoth (the one outlier in Figure 17 is an early estimate for the size of 1P/Halley; Peale, 1989). For smaller objects, with lower gravity ($g \propto r\rho$), other forces can play an important role in shaping their geology and interior structure, and it is unclear what processes should overlap (or not overlap) between small comets in the inner Solar System and KBOs like Arrokoth. Second, all comets with density constraints are Jupiter family comets or Halley-type comets, which have been traveling through the inner solar system for potentially millions of years. Their time in the inner Solar System subjects them to a myriad of processes that would not affect the primordial Arrokoth—particularly the sublimation and loss of many abundant volatile species (e.g., Grundy et al., 2020; Lisse et al., 2021) which may substantially alter their structure and density.

Arrokoth represents the smallest KBO with a density constraint. Amongst the thousands of known KBOs, only 24 systems have density constraints—all determined from astrometric observations of the orbits of binary (or multiple) systems, which yield the system mass which can be combined with measurements of object sizes (frequently determined from infrared measurements) to determine density. The lone exception is Neptune's moon, Triton, which we include in Figure 17 and Table S1 in Supporting Information S1 as it is likely a captured KBO; Triton's mass was determined from the flyby of *Voyager 2*. In most cases, these analyses yield the total mass of the multiple system, meaning it is only possible to determine an average density for the objects within. The mean density for these KBOs is 1,300 kg/m^3, although there is substantial spread. The only KBO with an Arrokoth like density is (148780) Altjira—a binary with two similarly sized objects (radii of 123 and 111 km)—and a density of 300 (160–800) kg/m^3 (Vilenius et al., 2014).

Arrokoth's inferred low density reinforces and extends the previously recognized trend that smaller KBOs to have lower densities (Bierson et al., 2019; Brown, 2012). Multiple hypotheses have been suggested to explain this trend, including (1) the presence of higher density ice phases in larger bodies, (2) compositional differences between small bodies and large bodies, and (3) the presence of substantial porosity in small bodies. High-pressure ice phases (Hypothesis 1) may contribute to the densities of the largest KBOs (although even i.e., debated; e.g., McKinnon et al., 2017), but certainly cannot explain the density variations for objects smaller than several hundred kilometers in radius, where internal pressures are too low for high-pressure ice phases (e.g., Journaux et al., 2020). Compositional variations (Hypothesis 2) may be produced by impact processes (e.g., the stripping of icy mantles of differentiated KBOs), loss of volatiles due to internal heating, or primordial variations in disk composition—although for various reasons, these hypotheses are not satisfactory (Bierson et al., 2019; Brown, 2012). Variations in porosity (Hypothesis 3) remain a plausible explanation. At larger sizes, radiogenic heating naturally leads to the loss of pore space, compaction, and higher densities (Bierson et al., 2019). However, Arrokoth's low density would imply one of the largest porosities for a solid Solar System body. The porosity of a body, ϕ, is related to the ratio between its observed density, ρ, and the density of the constituent grains, ρ_{grain}:

$$\phi = 1 - \rho/\rho_{grain}. \tag{21}$$

Assuming a grain density consistent with water ice, $\rho_{grain} = \rho_{ice} = 930$ kg/m^3, the porosity of Arrokoth would be 75% (spanning 35%–83% for the 1σ density range). This porosity would need to be higher if there was any rock component within Arrokoth—which should be expected. Assuming a rock density of $\rho_{rock} = 3{,}500$ kg/m^3 and rock mass fraction of 75% (consistent with Pluto, Charon, and many other KBOs; Bierson et al., 2019), the effective grain density is ∼2,154 kg/m^3, which would require Arrokoth to have a porosity of Arrokoth of 89% (spanning 72%–93% for the 1σ density range). While these inferred porosities are large, it is not atypical for small bodies to have substantial porosities. For example, the porosity of comet 67P/Churyumov–Gerasimenko has been inferred to be as large as 65%–79% (Pätzold et al., 2018), and the densities of asteroids (and particularly primitive, carbonaceous asteroids) are frequently observed to lie in the range of ∼50% to ∼70% (e.g., Baer et al., 2011; Barnouin et al., 2019; Okada et al., 2020).

An intriguing density analog comes from an unexpected place: Saturn. Orbiting amongst the rings of Saturn are small (r < 100 km) ring-moons (yellow points in Figure 17; Table S1 in Supporting Information S1), including Methone, Atlas, Pan, etc. Over the course of the *Cassini* mission (and during the proximal, ring-grazing orbits in particular), *Cassini* made several close flybys and detailed observations of these small moons—revealing incredibly varied, unique small worlds, ranging from the "ravioli"-shaped Pan and Atlas, "egg"-shaped Methone, and "sponge"-like Hyperion (e.g., Buratti et al., 2019; Charnoz et al., 2007; P.C. Thomas et al., 2019; Spilker, 2019). For many of these moons, *Cassini* was able to directly measure their masses through traditional radio science methods (where the gravitational perturbation of the moon is directly measured by its effect on *Cassini*'s trajectory, determined from the Doppler-shift of its radio link with Earth). Curiously, many of these moons also have low densities, with an average density of ∼450 kg/m^3 (when neglecting Phoebe), with Pallene having the lowest measured density: 251 (176–326) kg/m^3 (P. Thomas, Burns, et al., 2013; P. C. Thomas et al., 2019). Even lower densities have been inferred for Methone (307 (277–337) kg/m^3) and Pallene (251 (176–326) kg/m^3) based on assuming that their round shapes represent equilibrium figures (P. Thomas, Burns, et al., 2013)—which is effectively similar to the slope-minimization technique described previously. Independently, the *Cassini* Cosmic Dust Analyzer characterized the velocity distribution of dust around several of these moons, and found that the surfaces must be incredibly porous and dissipative to explain the low kinetic energy of ring particles ejected/bounced off the surfaces. The small ring moons of Saturn are composed primarily of water ice (Buratti et al., 2019). When

taken together, the similar densities between Saturn's ring moons and Arrokoth are suggestive. Perhaps the two share similar origins via gentle accretion of ice grains in a relatively quiescent environment—be it Saturn's rings, or the early Kuiper Belt. Most Arrokoth formation scenarios favor a very low-speed (~m/s) accretion (McKinnon et al., 2020; Stern et al., 2019), although they may still be orders of magnitude higher than typical collision speeds in the Saturn's rings (~mm/s), and in a different thermal environment. The constituent materials may also differ.

8. Summary and Outlook

In this work, we present a detailed analysis of the geophysical environment of the small KBO (486958) Arrokoth, based on available *New Horizons* shape models and other data. This work supports and expands upon the work published immediately after the *New Horizons* flyby (e.g., McKinnon et al., 2020; Spencer et al., 2020; Stern et al., 2019), and represents the first complete, detailed investigation of the geophysical environment of a small KBO. The key, *new* results include:

1. We confirm the alignment of Arrokoth's principal axes that was first reported in Stern et al. (2019) and McKinnon et al. (2020) with the latest shape model. The two lobes are misaligned by only 5.86°. For randomly oriented lobes, the probability of having two lobes so closely aligned is ~0.01%. This probability strongly suggest that some physical process, like tidal-locking, led to their current configuration. (See Sections 4.2, 5.5 and 7.1.2, Figure 3.)
2. Despite Arrokoth's bilobate shape, its surface is generally smooth at the resolution of the current shape models. The surface slopes are generally small ($10.4 \pm 7.5°$), and the geopotential elevation variations are small (1.5 ± 0.6 km). Surface accelerations are low (0.40 ± 0.07 mm/s^2). The exact values depend on the assumed density of Arrokoth, although the qualitative relationships between geophysical environment and geology are robust to changes in density. (See Section 4, Figures 4–8.)
3. Arrokoth's Roche lobe intersects it surface, meaning that regolith on some regions of Arrokoth have sufficient potential energy to slide off the surface and escape. However, the predicted trajectories of mass wasting do not suggest that mass is actually lost by this mechanism (in contrast to worlds like (101955) Bennu; Scheeres et al., 2019)—in part due to the bilobate shape of Arrokoth, which physically obstructs the pathways by which material would escape. (See Sections 4.7, 4.8 and 6 and Figures 10–13.)
4. Arrokoth exhibits a variety of surface markings, which have a complicated association with Arrokoth's geophysical environment. Bright material tends to be found in geopotential lows (as first reported in Stern et al., 2019)—although not all geopotential lows are associated with bright material, and bright material often exhibits more complex patterns than the predicted gravity would suggest (although that may be hindered by the limited resolution of the shape model). The basic trends are well-explained by mass-wasting of bright material down slopes, although alternate hypotheses exist. (See Sections 5, Figure 14.)
5. In some cases, the Coriolis force may play a role in mass-wasting processes on Arrokoth, and cause deflection of downslope movement that reflected in some observed surface markings on Arrokoth. The importance of the Coriolis force depends on the details of mass wasting on Arrokoth, which are largely unknown. (See Section 6, Figure 15.)
6. Multiple lines of evidence suggest that Arrokoth has a low density: $\rho = 235$ kg/m^3 (1σ range: 155–600 kg/m^3). Arrokoth's inferred low density was first reported in Spencer et al. (2020) and McKinnon et al. (2020), although explored with more rigor here—particularly with regards to the slope-minimization technique. Arrokoth's inferred density is low compared to the densities of well-characterized objects (e.g., comet 67P/Churyumov-Gerasimenko), but may be consistent (within the large uncertainties) with the ensemble of comets, some KBO binaries, and ring-moons of Saturn. For water ice bulk composition, this low density would imply a porosity of nearly 75%—and higher if there is any rock component. (See Sections 2.6 and 7, Figures 16 and 17.)

Despite the wealth of data produced by the *New Horizons* flyby of Arrokoth, the flyby has generated almost as many new questions as it has answered:

1. **What are the densities of small KBOs?** Our nominal density for Arrokoth, $\rho = 235$ kg/m^3, is incredibly low—lower than the vast majority of KBO densities (Figure 17). However, Arrokoth is a much smaller object than these other characterized KBOs (it is the smallest KBO with an inferred density). All other characterized KBOs are binary or multiple systems with individual components at least 3× larger than Arrokoth. It is

widely recognized that KBO densities decrease with decreasing size, however it is unclear how far that trend goes (and it clearly cannot go to zero density at zero size). Without a more complete sample, it is unclear if Arrokoth's inferred low density is (a) representative of other small KBOs, (b) an outlier, or (c) simply incorrect due to some flawed assumption(s) used in inferring its density. Better understanding the densities of small KBOs would shed light on how these planetesimals were formed in the early Solar System. Expanded telescope surveys searching for smaller binaries, and subsequent characterization campaigns (including occultation campaigns), may help address this question. *New Horizons* can also contribute to this by continuing to observe KBOs from within the Kuiper Belt during its extended mission. Future missions to small KBOs (like the *Persephone* mission concept to return to Pluto and explore the Kuiper Belt; Howett et al., 2021) could also address question, especially if the mass and density of targets can be directly measured with gravity science investigations. Similar investigations of the small irregular satellites of the gas giants may also be informative, since these populations are likely captured KBOs. Proposed missions to Uranus and Neptune, including *Neptune Odyssey* (Rymer et al., 2020), could support these investigations.

2. **What are the densities of comets?** Our expectations for Arrokoth were heavily based on intuition gained from exploration of comets, which were likely formed in the same regions of the Solar System (Moore et al., 2018). However, the densities of comets are poorly known. We only have precisely and unambiguously measured the density for a single comet, 67P/Churyumov-Gerasimenko (ρ = 532 kg/m^3; Jorda et al., 2016) from gravity measurements by the *Rosetta* mission. Continued observations of comets and determination of their densities—either through future missions or inferences from remote sensing—are warranted. While all comets would be informative, density determination of more pristine comets and related bodies (e.g., Centaurs) would be particularly informative, as they may be less affected by inner Solar System processes and more representative of their Kuiper Belt progenitors.
3. **How well can we infer the densities of small bodies without direct gravity measurements?** With the absence of direct gravity science measurements of Arrokoth's density (Section 2.6), we are forced to infer its density from a combination of different geophysical analyses (Section 7). Similar methods have been used to infer the densities of a wide number of small bodies, including asteroids, comets, and small planetary satellites (Section 7.1.3)—however, it is unclear how well these methods work, and whether the underlying assumptions are appropriate for a small KBO like Arrokoth. It would be beneficial to continue to test these methodologies with a combination of theoretical experiments, and analyses of the small subset of worlds where we have sufficient data to compare geophysical inferences with geophysical measurements.
4. **Are planetary rings (and ring moons) an analog for the formation of planetesimals?** The only objects in the Solar System with consistently low, Arrokoth-like, measured densities are Saturn's ring moons. These small worlds are thought to form from the gentle accretion of icy ring particles—which may not be unlike the formation of planetesimals via streaming instability and other processes in the early Kuiper Belt, although this comparison requires more investigation. Expanded models of ring and planetesimal dynamics may partially support testing this hypothesis, as could continued analysis of *Cassini* data. New, ultra-high-resolution observations of dense rings around gas giants (like those proposed by the *Saturn Ring Skimmer* mission concept; Tiscareno et al., 2021) may be particularly illustrative of how these small, low-density worlds form and evolve.
5. **What are the rotational and orbital dynamics of small Kuiper Belt binaries and contact binaries?** The remarkable alignment of Arrokoth's lobes with one another remains one of the most intriguing results of the *New Horizons* flyby of Arrokoth (Sections 4.2, 5.5; Stern et al., 2019; McKinnon et al., 2020). The simplest explanation for this observation is that the two lobes tidally locked and slowly spiraled together before gently merging. However, the details therein uncertain. For example: What was the original orbital configuration of the system? How was angular momentum drained from the system to let it merge? How did the merger actually happen, and what effects did it have on the resulting body? How long did this process take, and has Arrokoth remained in this configuration since its initial formation? Did the Sky impact occur before or after merger, and how did it affect the dynamics? Theoretical work is already beginning to address some of these problems (e.g., Hirabayashi et al., 2020; Lyra et al., 2021; Mao et al., 2021; Marohnic et al., 2021), although more work is necessary. Additionally, telescopic surveys for Kuiper Belt binaries and multiple systems at smaller sizes, along with follow-up characterization, would provide critical context for understanding the tidal evolution of small KBOs.
6. **What geologic processes shape the surfaces of small KBOs?** Arrokoth displays complex surface markings, which frequently appear related to the local geophysical environment, perhaps indicating the importance of mass wasting (Section 5). However, this is but one hypothesis, and the relative balance between mass wast-

ing and other effects—including impacts, thermophysical processes (i.e., sublimation), and tectonics—are unknown. Here, we favor mass wasting, but other groups have explained major aspects of Arrokoth, including its bilobate shape, with solely thermophysical processes (Zhao et al., 2021). It is also unclear whether these processes are active today, or predominantly active early in Arrokoth's history. This problem may be addressed with continued analysis of the *New Horizons* flyby data and modeling efforts. In particular, comparative planetology studies between Arrokoth and other small bodies—including asteroids, comets, and small moons of the gas giants (e.g., Helene, Calypso, Telesto; Umurhan et al., 2021)—may be particularly informative.

Data Availability Statement

The stereo and global shape models of Arrokoth are available in McKinnon et al. (2020) and Spencer et al. (2020). The merged shape model of Arrokoth will be formally released as part of a forthcoming *New Horizons* Planetary Data System Small Bodies Node (https://pds-smallbodies.astro.umd.edu/data_sb/missions/nh-kem/index.shtml). The merged shape model, along with an example MATLAB script for calculating the derived parameters presented in this paper are archived on Zenodo/GitHub: https://doi.org/10.5281/zenodo.6423483.

Acknowledgments
The authors thank the NASA for support of the *New Horizons* project, and the authors thank the entire *New Horizons* team for making the flyby possible. J. T. Keane acknowledges partial support from the Caltech Joint Center for Planetary Astronomy (JCPA) postdoctoral fellowship, and thanks Alan Stern for facilitating his participation in the Arrokoth flyby. A portion of this research was carried out at the Jet Propulsion Laboratory, California Institute of Technology, under a contract with the National Aeronautics and Space Administration (80NM0018D0004). This research has made use of NASA's Astrophysics Data System. The authors thank David Minton and one anonymous reviewer for their very thorough, insightful, and thought-provoking reviews which resulted in a more compelling manuscript.

References

A'Hearn, M. F., Belton, M. J. S., Delamere, W. A., Feaga, L. M., Hampton, D., Kissel, J., et al. (2011). EPOXI at comet Hartley 2. *Science*, *332*(6036), 1396–1400. https://doi.org/10.1126/science.1204054

Amarante, A., & Winter, O. C. (2020). Surface dynamics, equilibrium points and individual lobes of the Kuiper Belt Object (486958) Arrokoth. *Monthly Notices of the Royal Astronomical Society*, *496*(4), 4154–4173. https://doi.org/10.1093/mnras/staa1732

Baer, J., Chesley, S. R., & Matson, R. D. (2011). Astrometric masses of 26 asteroids and observations on asteroid porosity. *The Astronomical Journal*, *141*(5), 143. https://doi.org/10.1088/0004-6256/141/5/143

Barnouin, O. S., Daly, M. G., Palmer, E. E., Gaskell, R. W., Weirich, J. R., Johnson, C. L., et al. (2019). Shape of (101955) Bennu indicative of a rubble pile with internal stiffness. *Nature Geoscience*, *12*(4), 247–252. https://doi.org/10.1038/s41561-019-0330-x

Beddingfield, C. B., Beyer, R., Schenk, P., Moore, J., Weaver, H. A., Olkin, C. B., et al. (2019). Deriving an Ultima Thule Digital Shape Kernel. In *Lunar and Planetary Science Conference* (p. 1901).

Benecchi, S. D., Porter, S. B., Buie, M. W., Zangari, A. M., Verbiscer, A. J., Noll, K. S., et al. (2019). The HST lightcurve of (486958) 2014 MU_{69}. *Icarus*, *334*, 11–21. https://doi.org/10.1016/j.icarus.2019.01.023

Besl, P. J., & McKay, N. D. (1992). Method for registration of 3-D shapes. In P. S. Schenker (Ed.), *Sensor fusion IV: Control paradigms and data structures* (Vol. 1611, pp. 586–606). https://doi.org/10.1117/12.57955

Beyer, R. A., Alexandrov, O., & McMichael, S. (2018). The Ames Stereo Pipeline: NASA's open source software for deriving and processing terrain data. *Earth and Space Science*, *5*(9), 537–548. https://doi.org/10.1029/2018EA000409

Beyer, R. A., Porter, S., Schenk, P., Spencer, J., Beddingfield, C., Grundy, W., et al. (2019). Stereo topography of KBO (486958) 2014 MU69. In *EPSC-DPS Joint Meeting 2019* (Vol. 2019, p. EPSC-DPS2019-849).

Beyer, R. A., Weaver, H. A., Porter, S. B., Grundy, W. M., Moore, J. M., Beddingfield, C. B., et al. (2019). Potential mapping schemes and reference systems for MU69. In *Lunar and Planetary Science Conference* (p. 2258).

Bierson, C. J., Umurhan, O. M., Robbins, S. J., Lisse, C., Nimmo, F., Beyer, R. A., et al. (2019). Limb topography of 2014 MU69: First results from the New Horizons flyby. In *Lunar and Planetary Science Conference* (p. 1944).

Brown, M. E. (2012). The compositions of Kuiper Belt Objects. *Annual Review of Earth and Planetary Sciences*, *40*(1), 467–494. https://doi.org/10.1146/annurev-earth-042711-105352

Buie, M. W., Porter, S. B., Tamblyn, P., Terrell, D., Parker, A. H., Baratoux, D., et al. (2020). Size and shape constraints of (486958) Arrokoth from stellar occultations. *The Astronomical Journal*, *159*(4), 130. https://doi.org/10.3847/1538-3881/ab6ced

Buie, M. W., Porter, S. B., Verbiscer, A., Leiva, R., Keeney, B. A., Tsang, C., et al. (2018). Pre-encounter update on (486958) 2014MU69 and occultation results from 2017 and 2018. *AAS/Division for Planetary Sciences Meeting Abstracts #50* (Vol. 50, p. 509.06).

Buratti, B. J., Thomas, P. C., Roussos, E., Howett, C., Seiß, M., Hendrix, A. R., et al. (2019). Close Cassini flybys of Saturn's ring moons Pan, Daphnis, Atlas, Pandora, and Epimetheus. *Science*, *364*(6445). https://doi.org/10.1126/science.aat2349

Chandrasekhar, S. (1969). *Ellipsoidal figures of equilibrium*. Yale University Press.

Charnoz, S., Brahic, A., Thomas, P. C., & Porco, C. C. (2007). The equatorial ridges of Pan and Atlas: Terminal accretionary ornaments? *Science*, *318*(5856), 1622–1624. https://doi.org/10.1126/science.1148631

Chen, Y., & Medioni, G. (1992). Object modelling by registration of multiple range images. *Image and Vision Computing*, *10*(3), 145–155. (Range Image Understanding). https://doi.org/10.1016/0262-8856(92)90066-C

Descamps, P. (2008). Roche figures of doubly synchronous asteroids. *Planetary and Space Science*, *56*(14), 1839–1846. https://doi.org/10.1016/j.pss.2008.02.040

Descamps, P. (2010). Equilibrium figures of inhomogeneous synchronous binary asteroids. *Icarus*, *207*(2), 758–768. https://doi.org/10.1016/j.icarus.2009.12.011

Descamps, P. (2015). Dumb-bell-shaped equilibrium figures for fiducial contact-binary asteroids and EKBOs. *Icarus*, *245*, 64–79. https://doi.org/10.1016/j.icarus.2014.08.002

Dobrovolskis, A. R. (1996). Inertia of any polyhedron. *Icarus*, *124*(2), 698–704. https://doi.org/10.1006/icar.1996.0243

Dobrovolskis, A. R. (2021). Surface potential of a rotating duplex consisting of two conjoined spheres. *Icarus*, *358*, 114061. https://doi.org/10.1016/j.icarus.2020.114061

Farnham, T. L., & Cochran, A. L. (2002). A McDonald observatory study of comet 19P/Borrelly: Placing the deep space 1 observations into a broader context. *Icarus*, *160*(2), 398–418. https://doi.org/10.1006/icar.2002.6969

Gnat, O., & Sari, R. (2010). Equilibrium configurations of synchronous binaries: Numerical solutions and application to Kuiper Belt Binary 2001 QG_{298}. *The Astrophysical Journal*, *719*(2), 1602–1618. https://doi.org/10.1088/0004-637X/719/2/1602

Grishin, E., Malamud, U., Perets, H. B., Wandel, O., & Schäfer, C. M. (2020). The wide-binary origin of (2014) MU_{69}-like Kuiper belt contact binaries. *Nature*, *580*(7804), 463–466. https://doi.org/10.1038/s41586-020-2194-z

Grundy, W. M., Bird, M. K., Britt, D. T., Cook, J. C., Cruikshank, D. P., Howett, C. J. A., et al. (2020). Color, composition, and thermal environment of Kuiper Belt Object (486958) Arrokoth. *Science*, *367*(6481), aay3705. https://doi.org/10.1126/science.aay3705

Hirabayashi, M., Trowbridge, A. J., & Bodewits, D. (2020). The mysterious location of Maryland on 2014 MU69 and the reconfiguration of its bilobate shape. *The Astrophysical Journal*, *891*(1), L12. https://doi.org/10.3847/2041-8213/ab3e74

Hofgartner, J. D., Buratti, B. J., Benecchi, S. D., Beyer, R. A., Cheng, A., Keane, J. T., et al. (2021). Photometry of Kuiper Belt Object (486958) Arrokoth from New Horizons LORRI. *Icarus*, *356*, 113723. https://doi.org/10.1016/j.icarus.2020.113723

Holsapple, K. A. (2001). Equilibrium configurations of solid cohesionless bodies. *Icarus*, *154*(2), 432–448. https://doi.org/10.1006/icar.2001.6683

Holsapple, K. A. (2004). Equilibrium figures of spinning bodies with self-gravity. *Icarus*, *172*(1), 272–303. https://doi.org/10.1016/j.icarus.2004.05.023

Howett, C. J. A., Robbins, S. J., Holler, B. J., Hendrix, A., Fielhauer, K. B., Perry, M. E., et al. (2021). Persephone: A Pluto-system Orbiter and Kuiper Belt Explorer. *Planetary Science Journal*, *2*(2), 75. https://doi.org/10.3847/PSJ/abe6aa

Jorda, L., Gaskell, R., Capanna, C., Hviid, S., Lamy, P., Ďurech, J., et al. (2016). The global shape, density and rotation of Comet 67P/Churyumov-Gerasimenko from preperihelion Rosetta/OSIRIS observations. *Icarus*, *277*, 257–278. https://doi.org/10.1016/j.icarus.2016.05.002

Journaux, B., Kalousová, K., Sotin, C., Tobie, G., Vance, S., Saur, J., et al. (2020). Large ocean worlds with high-pressure ices. *Space Science Reviews*, *216*(1), 7. https://doi.org/10.1007/s11214-019-0633-7

Judson, A., & Doesken, N. (2000). Density of freshly fallen snow in the central rocky mountains. *Bulletin of the American Meteorological Society*, *81*(7), 1577–1588. https://doi.org/10.1175/1520-0477(2000)081<1577:DOFFSI>2.3.CO;2

Kaasalainen, M., & Viikinkoski, M. (2012). Shape reconstruction of irregular bodies with multiple complementary data sources. *Astronomy and Astrophysics*, *543*, A97. https://doi.org/10.1051/0004-6361/201219267

Kanamaru, M., Sasaki, S., & Wieczorek, M. (2019). Density distribution of asteroid 25143 Itokawa based on smooth terrain shape. *Planetary and Space Science*, *174*, 32–42. https://doi.org/10.1016/j.pss.2019.05.002

Katz, J. I., & Wang, S. (2021). Arrokoth's necklace. *Monthly Notices of the Royal Astronomical Society*, *504*(1), 601–609. https://doi.org/10.1093/mnras/stab718

Kinczyk, M. J., Runyon, K., Robbins, S. J., Keane, J. T., Grundy, W. M., Throop, H. B., et al. (2019). Generating a 3D shape model of 2014 MU69 for scientific visualization and public outreach. In *Lunar and Planetary Science Conference* (p. 2456).

King, J., Howell, S., Brady, M., Toose, P., Derksen, C., Haas, C., & Beckers, J. (2020). Local-scale variability of snow density on Arctic sea ice. *The Cryosphere*, *14*(12), 4323–4339. https://doi.org/10.5194/tc-14-4323-2020

Lisse, C. M., Young, L. A., Cruikshank, D. P., Sandford, S. A., Schmitt, B., Stern, S. A., et al. (2021). On the origin & thermal stability of Arrokoth's and Pluto's ices. *Icarus*, *356*, 114072. https://doi.org/10.1016/j.icarus.2020.114072

Lyra, W., Youdin, A. N., & Johansen, A. (2021). Evolution of MU69 from a binary planetesimal into contact by Kozai-Lidov oscillations and nebular drag. *Icarus*, *356*, 113831. https://doi.org/10.1016/j.icarus.2020.113831

Malhotra, R. (1993). The origin of Pluto's peculiar orbit. *Nature*, *365*(6449), 819–821. https://doi.org/10.1038/365819a0

Mao, X., McKinnon, W. B., Singer, K. N., Keane, J. T., Robbins, S. J., Schenk, P. M., et al. (2021). Collisions with small classical Kuiper Belt Objects are not sufficient to cause substantial spin changes to Arrokoth. In *Lunar and Planetary Science Conference* (p. 2415).

Marohnic, J. C., Richardson, D. C., McKinnon, W. B., Agrusa, H. F., DeMartini, J. V., Cheng, A. F., et al. (2021). Constraining the final merger of contact binary (486958) Arrokoth with soft-sphere discrete element simulations. *Icarus*, *356*, 113824. https://doi.org/10.1016/j.icarus.2020.113824

McKinnon, W. B., Richardson, D. C., Marohnic, J. C., Keane, J. T., Grundy, W. M., Hamilton, D. P., et al. (2020). The solar nebula origin of (486958) Arrokoth, a primordial contact binary in the Kuiper Belt. *Science*, *367*(6481), aay6620. https://doi.org/10.1126/science.aay6620

McKinnon, W. B., Stern, S., Weaver, H., Nimmo, F., Bierson, C., Grundy, W., et al. (2017). Origin of the Pluto–Charon system: Constraints from the New Horizons flyby. *Icarus*, *287*, 2–11. (Special Issue: The Pluto System). https://doi.org/10.1016/j.icarus.2016.11.019

Minton, D. A. (2008). The topographic limits of gravitationally bound, rotating sand piles. *Icarus*, *195*(2), 698–704. https://doi.org/10.1016/j.icarus.2008.02.009

Moore, J. M., Howard, A. D., Umurhan, O. M., White, O. L., Schenk, P. M., Beyer, R. A., et al. (2017). Sublimation as a landform-shaping process on Pluto. *Icarus*, *287*, 320–333. (Special Issue: The Pluto System). https://doi.org/10.1016/j.icarus.2016.08.025

Moore, J. M., McKinnon, W. B., Cruikshank, D. P., Gladstone, G. R., Spencer, J. R., Stern, S. A., et al. (2018). Great expectations: Plans and predictions for New Horizons encounter with Kuiper Belt Object 2014 MU_{69} ("Ultima Thule"). *Geophysical Research Letters*, *45*(16), 8111–8120. https://doi.org/10.1029/2018GL078996

Moore, J. M., Umurhan, O. M., White, O. L., McKinnon, W. B., Spencer, J. R., Stern, S. A., et al. (2020). Scarp retreat on (486958) Arrokoth: Evidence and implications for composition and structure. In *Lunar and Planetary Science Conference* (p. 1691).

Nesvorný, D. (2018). Dynamical evolution of the early solar system. *Annual Review of Astronomy and Astrophysics*, *56*(1), 137–174. https://doi.org/10.1146/annurev-astro-081817-052028

Okada, T., Fukuhara, T., Tanaka, S., Taguchi, M., Arai, T., Senshu, H., et al. (2020). Highly porous nature of a primitive asteroid revealed by thermal imaging. *Nature*, *579*(7800), 518–522. https://doi.org/10.1038/s41586-020-2102-6

Otto, K. A., Jaumann, R., Krohn, K., Spahn, F., Raymond, C. A., & Russell, C. T. (2016). The Coriolis effect on mass wasting during the Rheasilvia impact on asteroid Vesta. *Geophysical Research Letters*, *43*(24), 12340–12347. https://doi.org/10.1002/2016GL071539

Pätzold, M., Andert, T., Hahn, M., Asmar, S. W., Barriot, J. P., Bird, M. K., et al. (2016). A homogeneous nucleus for comet 67P/Churyumov-Gerasimenko from its gravity field. *Nature*, *530*(7588), 63–65. https://doi.org/10.1038/nature16535

Pätzold, M., Andert, T. P., Hahn, M., Barriot, J.-P., Asmar, S. W., Häusler, B., et al. (2018). The Nucleus of comet 67P/Churyumov–Gerasimenko – Part I: The global view – Nucleus mass, mass-loss, porosity, and implications. *Monthly Notices of the Royal Astronomical Society*, *483*(2), 2337–2346. https://doi.org/10.1093/mnras/sty3171

Peale, S. J. (1989). On the density of Halley's comet. *Icarus*, *82*(1), 36–49. https://doi.org/10.1016/0019-1035(89)90021-3

Perinotto, H., Schneider, J.-L., Bachèlery, P., Le Bourdonnec, F.-X., Famin, V., & Michon, L. (2015). The extreme mobility of debris avalanches: A new model of transport mechanism. *Journal of Geophysical Research*, *120*(12), 8110–8119. https://doi.org/10.1002/2015JB011994

Porter, S. B., Bierson, C. J., Umurhan, O., Beyer, R. A., Lauer, T. A., Buie, M. W., et al. (2019). A contact binary in the Kuiper Belt: The shape and pole of (486958) 2014 MU69. In *Lunar and Planetary Science Conference* (p. 1611).

Porter, S. B., Buie, M. W., Parker, A. H., Spencer, J. R., Benecchi, S., Tanga, P., et al. (2018). High-precision orbit fitting and uncertainty analysis of (486958) 2014 MU69. *The Astronomical Journal*, *156*(1), 20. https://doi.org/10.3847/1538-3881/aac2e1

Porter, S. B., Showalter, M. R., Weaver, H. A., Spencer, J. R., Binzel, R. P., Hamilton, D. P., et al. (2016). Shapes and poles of the small satellites of Pluto. In *Lunar and Planetary Science Conference* (p. 2402).
Porter, S. B., Showalter, M. R., Weaver, H. A., Spencer, J. R., Lauer, T. R., Verbiscer, A. J., et al. (2019). The shapes and poles of Nix and Hydra from New Horizons. In *Pluto system after new horizons* (Vol. 2133,p. 7038).
Porter, S. B., Spencer, J. R., Verbiscer, A., Benecchi, S., Weaver, H. A., Wen Lin, H., et al. (2022). Orbits and occultation opportunities of 15 TNOs observed by New Horizons. *Planetary Science Journal*, *3*(1), 23. https://doi.org/10.3847/PSJ/ac3491
Porter, S. B., Verbiscer, A. J., Keane, J. T., Weaver, H. A., Singer, K. N., Brandt, P. C., et al. (2022). The poles and shapes of seven Kuiper Belt Objects as measured from New Horizons. In *53rd Annual Lunar and Planetary Science Conference* (p. 2170).
Richardson, J. E., & Bowling, T. J. (2014). Investigating the combined effects of shape, density, and rotation on small body surface slopes and erosion rates. *Icarus*, *234*, 53–65. https://doi.org/10.1016/j.icarus.2014.02.015
Richardson, J. E., Graves, K. J., Harris, A. W., & Bowling, T. J. (2019). Small body shapes and spins reveal a prevailing state of maximum topographic stability. *Icarus*, *329*, 207–221. https://doi.org/10.1016/j.icarus.2019.03.027
Rollin, G., Shevchenko, I. I., & Lages, J. (2021). Dynamical environments of MU69 and similar objects. *Icarus*, *357*, 114178. https://doi.org/10.1016/j.icarus.2020.114178
Rymer, A. M., Clyde, B., & Runyon, K., & Neptune-Odyssey team. (2020). Neptune Odyssey: Mission to the Neptune-Triton system. *LPI Contribution*, *2547*, 6031.
Scheeres, D. J. (2012). *Orbital motion in strongly perturbed environments: Applications to asteroid, comet and planetary satellite orbiters*. Springer-Verlag Berlin Heidelberg. https://doi.org/10.1007/978-3-642-03256-1
Scheeres, D. J. (2015). Landslides and mass shedding on spinning spheroidal asteroids. *Icarus*, *247*, 1–17. https://doi.org/10.1016/j.icarus.2014.09.017
Scheeres, D. J., Hesar, S. G., Tardivel, S., Hirabayashi, M., Farnocchia, D., McMahon, J. W., et al. (2016). The geophysical environment of Bennu. *Icarus*, *276*, 116–140. https://doi.org/10.1016/j.icarus.2016.04.013
Scheeres, D. J., McMahon, J. W., French, A. S., Brack, D. N., Chesley, S. R., Farnocchia, D., et al. (2019). The dynamic geophysical environment of (101955) Bennu based on OSIRIS-REx measurements. *Nature Astronomy*, *3*(4), 352–361. https://doi.org/10.1038/s41550-019-0721-3
Schenk, P., Singer, K., Beyer, R., Beddingfield, C., Robbins, S. J., McKinnon, W. B., et al. (2021). Origins of pits and troughs and degradation on a small primitive planetesimal in the Kuiper Belt: High-resolution topography of (486958) Arrokoth (aka 2014 MU69) from New Horizons. *Icarus*, *356*, 113834. https://doi.org/10.1016/j.icarus.2020.113834
Sharma, I. (2015). Stability of binaries. Part 1: Rigid binaries. *Icarus*, *258*, 438–453. https://doi.org/10.1016/j.icarus.2015.05.002
Sharma, I. (2016). Stability of binaries. Part II: Rubble-pile binaries. *Icarus*, *277*, 125–140. https://doi.org/10.1016/j.icarus.2016.04.017
Spencer, J. R., Stern, S. A., Moore, J. M., Weaver, H. A., Singer, K. N., Olkin, C. B., et al. (2020). The geology and geophysics of Kuiper Belt Object (486958) Arrokoth. *Science*, *367*(6481), aay3999. https://doi.org/10.1126/science.aay3999
Spilker, L. (2019). Cassini-Huygens' exploration of the Saturn system: 13 years of discovery. *Science*, *364*(6445), 1046–1051. https://doi.org/10.1126/science.aat3760
Steckloff, J. K., Lisse, C. M., Safrit, T. K., Bosh, A. S., Lyra, W., & Sarid, G. (2021). The sublimative evolution of (486958) Arrokoth. *Icarus*, *356*, 113998. https://doi.org/10.1016/j.icarus.2020.113998
Stern, S. A., Keeney, B., Singer, K. N., White, O., Hofgartner, J. D., & Grundy, W., & The New Horizons Team. (2021). Some new results and perspectives regarding the Kuiper Belt Object Arrokoth's remarkable, bright neck. *Planetary Science Journal*, *2*(3), 87. https://doi.org/10.3847/PSJ/abee26
Stern, S. A., Weaver, H. A., Spencer, J. R., Olkin, C. B., Gladstone, G. R., Grundy, W. M., et al. (2019). Initial results from the New Horizons exploration of 2014 MU_{69}, a small Kuiper Belt Object. *Science*, *364*(6441), aaw9771. https://doi.org/10.1126/science.aaw9771
Taylor, J. R. (2005). *Classical mechanics*. University Science Books.
Thomas, P., Burns, J., Hedman, M., Helfenstein, P., Morrison, S., Tiscareno, M., & Veverka, J. (2013). The inner small satellites of Saturn: A variety of worlds. *Icarus*, *226*(1), 999–1019. https://doi.org/10.1016/j.icarus.2013.07.022
Thomas, P. C., A'Hearn, M., Belton, M. J. S., Brownlee, D., Carcich, B., Hermalyn, B., et al. (2013). The nucleus of Comet 9P/Tempel 1: Shape and geology from two flybys. *Icarus*, *222*(2), 453–466. https://doi.org/10.1016/j.icarus.2012.02.037
Thomas, P. C., A'Hearn, M. F., Veverka, J., Belton, M. J. S., Kissel, J., Klaasen, K. P., et al. (2013). Shape, density, and geology of the nucleus of Comet 103P/Hartley 2. *Icarus*, *222*(2), 550–558. https://doi.org/10.1016/j.icarus.2012.05.034
Thomas, P. C., Tiscareno, M. S., & Helfenstein, P. (2019). The inner small satellites of Saturn and Hyperion. In P. M. Schenk, R. N. Clark, C. J. A. Howett, A. J. Verbiscer, & J. H. Waite (Eds.), *Enceladus and the icy moons of saturn* (pp. 387–408). The University of Arizona Press.
Tiscareno, M., Vaquero, M., Hedman, M. M., Cao, H., Estrada, P. R., Ingersoll, A. P., et al. (2021). The Saturn Ring Skimmer Mission Concept: The next step to explore Saturn's rings, atmosphere, interior and inner magnetosphere. *Bulletin of the American Astronomical Society*, *53*(4), 372. https://doi.org/10.3847/25c2cfeb.82f6e9ff
Umurhan, O. M., Grundy, W. M., Bird, M. K., Beyer, R. A., Keane, J. T., Linscott, I. R., et al. (2022). A Near-surface Temperature Model of Arrokoth. *Planetary Science Journal*, *3*, 110. https://doi.org/10.3847/PSJ/ac5d3d
Umurhan, O. M., Howard, A. D., White, O. L., Schenk, P. M., & Moore, J. M. (2021). Modeling global-scale mass flows on the Lagrangian satellites of Dione and Tethys. *Icarus*, *369*, 114612. https://doi.org/10.1016/j.icarus.2021.114612
Umurhan, O. M., Keane, J. T., Beyer, R. A., Bird, M., Linscott, I., Porter, S. B., et al. (2020). Thermophysical, gravitational, and geomorphology properties of 2014 MU69. In *American Astronomical Society Meeting Abstracts #235*, (Vol. 235, p. 419.05). https://doi.org/10.2458/azu_uapress_9780816540945-ch010
Verbiscer, A. J., Porter, S. B., Kavelaars, J. J., Helfenstein, S. D., Benecchi, S. D., Weaver, H. A., et al. (2022). Putting (486958) Arrokoth in context: New Horizons photometry of other small cold classical Kuiper Belt Objects. In *53rd Annual Lunar and Planetary Science Conference* (p. 2488).
Vilenius, E., Kiss, C., Müller, T., Mommert, M., Santos-Sanz, P., Pál, A., et al. (2014). "TNOs are Cool": A survey of the trans-Neptunian region. X. Analysis of classical Kuiper Belt Objects from Herschel and Spitzer observations. *Astronomy and Astrophysics*, *564*, A35. https://doi.org/10.1051/0004-6361/201322416
Weaver, H. A., Porter, S. B., & Spencer, J. R., & The New Horizons Science Team. (2022). High-resolution search for Kuiper Belt Object Binaries from New Horizons. *Planetary Science Journal*, *3*(2), 46. https://doi.org/10.3847/PSJ/ac4cb7
Werner, R. A. (1994). The gravitational potential of a homogeneous polyhedron or don't cut corners. *Celestial Mechanics and Dynamical Astronomy*, *59*(3), 253–278. https://doi.org/10.1007/BF00692875
Werner, R. A. (1997). Spherical harmonic coefficients for the potential of a constant-density polyhedron. *Computers & Geosciences*, *23*(10), 1071–1077. https://doi.org/10.1016/S0098-3004(97)00110-6

Werner, R. A., & Scheeres, D. J. (1997). Exterior gravitation of a polyhedron derived and compared with harmonic and mascon gravitation representations of asteroid 4769 Castalia. *Celestial Mechanics and Dynamical Astronomy*, *65*(3), 313–344. https://doi.org/10.1007/bf00053511

Zhao, Y., Rezac, L., Skorov, Y., Hu, S. C., Samarasinha, N. H., & Li, J. Y. (2021). Sublimation as an effective mechanism for flattened lobes of (486958) Arrokoth. *Nature Astronomy*, *5*(2), 139–144. https://doi.org/10.1038/s41550-020-01218-7

References From the Supporting Information

A'Hearn, M. F., Belton, M. J. S., Delamere, W. A., Feaga, L. M., Hampton, D., Kissel, J., et al. (2011). Epoxi at comet Hartley 2. *Science*, *332*(6036), 1396–1400. https://doi.org/10.1126/science.1204054

Asphaug, E., & Benz, W. (1996). Size, density, and structure of Comet Shoemaker Levy 9 inferred from the physics of tidal breakup. *Icarus*, *121*(2), 225–248. https://doi.org/10.1006/icar.1996.0083

Benecchi, S. D., Noll, K. S., Grundy, W. M., & Levison, H. F. (2010). (47171) 1999 TC 36, A transneptunian triple. *Icarus*, *207*(2), 978–991. https://doi.org/10.1016/j.icarus.2009.12.017

Brown, M. E., & Butler, B. J. (2017). The density of mid-sized Kuiper Belt Objects from ALMA thermal observations. *The Astronomical Journal*, *154*(1), 19. https://doi.org/10.3847/1538-3881/aa6346

Brozović, M., Showalter, M. R., Jacobson, R. A., & Buie, M. W. (2015). The orbits and masses of satellites of Pluto. *Icarus*, *246*, 317–329. https://doi.org/10.1016/j.icarus.2014.03.015

Davidsson, B. J. R., & Gutiérrez, P. J. (2004). Estimating the nucleus density of Comet 19P/Borrelly. *Icarus*, *168*(2), 392–408. https://doi.org/10.1016/j.icarus.2003.11.009

Davidsson, B. J. R., & Gutiérrez, P. J. (2006). Non-gravitational force modeling of Comet 81P/Wild 2. I. A nucleus bulk density estimate. *Icarus*, *180*(1), 224–242. https://doi.org/10.1016/j.icarus.2005.07.023

Davidsson, B. J. R., Gutiérrez, P. J., & Rickman, H. (2007). Nucleus properties of Comet 9P/Tempel 1 estimated from non-gravitational force modeling. *Icarus*, *187*(1), 306–320. https://doi.org/10.1016/j.icarus.2006.07.022

Farnham, T. L., & Cochran, A. L. (2002). A McDonald observatory study of comet 19P/Borrelly: Placing the deep space 1 observations into a broader context. *Icarus*, *160*(2), 398–418. https://doi.org/10.1006/icar.2002.6969

Grundy, W. M., Noll, K. S., Roe, H. G., Buie, M. W., Porter, S. B., Parker, A. H., et al. (2019). Mutual orbit orientations of transneptunian binaries. *Icarus*, *334*, 62–78. https://doi.org/10.1016/j.icarus.2019.03.035

Grundy, W. M., Stansberry, J. A., Noll, K. S., Stephens, D. C., Trilling, D. E., Kern, S. D., et al. (2007). The orbit, mass, size, albedo, and density of (65489) Ceto/Phorcys: A tidally-evolved binary centaur. *Icarus*, *191*(1), 286–297. https://doi.org/10.1016/j.icarus.2007.04.004

Jacobson, R. A. (1990). The orbits of the satellites of Neptune. *Astronomy and As trophysics*, *231*(1), 241–250.

Jacobson, R. A. (2009). The orbits of the Neptunian satellites and the orientation of the pole of Neptune. *The Astronomical Journal*, *137*(5), 4322–4329. https://doi.org/10.1088/0004-6256/137/5/4322

Jacobson, R. A., Antreasian, P. G., Bordi, J. J., Criddle, K. E., Ionasescu, R., Jones, J. B., et al. (2006). The gravity field of the Saturnian system from satellite observations and spacecraft tracking data. *The Astronomical Journal*, *132*(6), 2520–2526. https://doi.org/10.1086/508812

Jacobson, R. A., Riedel, J. E., & Taylor, A. H. (1991). The orbits of Triton and Nereid from spacecraft and Earth based observations. *Astronomy and Astrophysics*, *247*(2), 565–575.

Jacobson, R. A., Spitale, J., Porco, C. C., Beurle, K., Cooper, N. J., Evans, M. W., & Murray, C. D. (2008). Revised orbits of Saturn's small inner satellites. *The Astronomical Journal*, *135*(1), 261–263. https://doi.org/10.1088/0004-6256/135/1/261

Jorda, L., Gaskell, R., Capanna, C., Hviid, S., Lamy, P., Durech, J., et al. (2016). The global shape, density and rotation of Comet 67P/Churyumov-Gerasimenko from preperihelion Rosetta/OSIRIS observations. *Icarus*, *277*, 257–278. https://doi.org/10.1016/j.icarus.2016.05.002

Kiss, C., Marton, G., Farkas-Takács, A., Stansberry, J., M¨uller, T., Vink´o, J., et al. (2017). Discovery of a satellite of the large trans-Neptunian object (225088) 2007 OR10. *The Astrophysical Journal Letters*, *838*(1), L1. https://doi.org/10.3847/2041-8213/aa6484

Kiss, C., Marton, G., Parker, A. H., Grundy, W. M., Farkas-Tak´acs, A., Stansberry, J., et al. (2019). The mass and density of the dwarf planet (225088) 2007 OR10. *Icarus*, *334*, 3–10. https://doi.org/10.1016/j.icarus.2019.03.013

Kovalenko, I. D., Doressoundiram, A., Lellouch, E., Vilenius, E., M¨uller, T., & Stansberry, J. (2017). "TNOs are Cool": A survey of the trans-Neptunian region. XIII. Statistical analysis of multiple trans-Neptunian objects observed with Herschel space Observatory. *Astronomy and Astrophysics*, *608*, A19. https://doi.org/10.1051/0004-6361/201730588

Lamy, P. L., Toth, I., Fernández, Y. R., & Weaver, H. A. (2019). The sizes, shapes, albedos, and colors of cometary nuclei. In M. Festou, H. U. Keller, & J. H. Waite (Eds.), *Comets II* (pp. 223–264). The University of Arizona Press.

Lellouch, E., Santos-Sanz, P., Lacerda, P., Mommert, M., Duffard, R., Ortiz, J. L., et al. (2013). "TNOs are Cool": A survey of the trans-Neptunian region. IX. Thermal properties of Kuiper Belt Objects and Centaurs from combined Herschel and spitzer observations. *Astronomy and Astrophysics*, *557*, A60. https://doi.org/10.1051/0004-6361/201322047

Movshovitz, N., Asphaug, E., & Korycansky, D. (2012). Numerical modeling of the disruption of Comet D/1993 F2 shoemaker-Levy 9 representing the progenitor by a gravitationally bound assemblage of randomly shaped polyhedra. *The Astrophysical Journal*, *759*(2), 93. https://doi.org/10.1088/0004-637X/759/2/93

Nimmo, F., Umurhan, O., Lisse, C. M., Bierson, C. J., Lauer, T. R., Buie, M. W., et al. (2017). Mean radius and shape of Pluto and Charon from New Horizons images. *Icarus*, *287*, 12–29. https://doi.org/10.1016/j.icarus.2016.06.027

Ortiz, J. L., Santos-Sanz, P., Sicardy, B., Benedetti-Rossi, G., B´erard, D., Morales, N., et al. (2017). The size, shape, density and ring of the dwarf planet Haumea from a stellar occultation. *Nature*, *550*(7675), 219–223. https://doi.org/10.1038/nature24051

Pätzold, M., Andert, T., Hahn, M., Asmar, S. W., Barriot, J. P., Bird, M. K., et al. (2016). A homogeneous nucleus for comet 67P/Churyumov Gerasimenko from its gravity field. *Nature*, *530*(7588), 63–65. https://doi.org/10.1038/nature16535

Peale, S. J. (1989). On the density of Halley's comet. *Icarus*, *82*(1), 36–49. https://doi.org/10.1016/0019-1035(89)90021-3

Porco, C. C., Baker, E., Barbara, J., Beurle, K., Brahic, A., Burns, J. A., et al. (2005). Cassini imaging science: Initial results on Saturn's rings and small satellites. *Science*, *307*(5713), 1226–1236. https://doi.org/10.1126/science.1108056

Porco, C. C., Thomas, P. C., Weiss, J. W., & Richardson, D. C. (2007). Saturn's small inner satellites: Clues to their origins. *Science*, *318*(5856), 1602–1607. https://doi.org/10.1126/science.1143977

Porter, S. B., Showalter, M. R., Weaver, H. A., Spencer, J. R., Lauer, T. R., Verbiscer, A. J., et al. (2019). The shapes and poles of Nix and Hydra from New Horizons. In *Pluto system after New Horizons* (Vol. 2133, p. 7038).

Ragozzine, D., & Brown, M. E. (2009). Orbits and masses of the satellites of the dwarf Planet Haumea (2003 EL61). *The Astronomical Journal*, *137*(6), 4766–4776. https://doi.org/10.1088/0004-6256/137/6/4766

Richardson, J. E., & Bowling, T. J. (2014). Investigating the combined effects of shape, density, and rotation on small body surface slopes and erosion rates. *Icarus*, *234*, 53–65. https://doi.org/10.1016/j.icarus.2014.02.015

Richardson, J. E., Melosh, H. J., Lisse, C. M., & Carcich, B. (2007). A ballistics analysis of the Deep Impact ejecta plume: Determining Comet Tempel 1's gravity, mass, and density. *Icarus*, *190*(2), 357–390. https://doi.org/10.1016/j.icarus.2007.08.001

Sagdeev, R. Z., Elyasberg, P. E., & Moroz, V. I. (1988). Is the nucleus of comet Halley a low density body? *Nature*, *331*(6153), 240–242. https://doi.org/10.1038/331240a0

Sicardy, B., Ortiz, J. L., Assafin, M., Jehin, E., Maury, A., Lellouch, E., et al. (2011). A Pluto-like radius and a high albedo for the dwarf planet Eris from an occultation. *Nature*, *478*(7370), 493–496. https://doi.org/10.1038/nature10550

Skorov, Y. V., & Rickman, H. (1999). Gas flow and dust acceleration in a cometary Knudsen layer. *Planetary and Space Science*, *47*(8–9), 935–949. https://doi.org/10.1016/S0032-0633(99)00008-2

Solem, J. C. (1995). Cometary breakup calculations based on a gravitationally bound agglomeration model: The density and size of shoemaker-Levy 9. *Astronomy and Astrophysics*, *302*, 596.

Spencer, J. R., Stansberry, J. A., Grundy, W. M., & Noll, K. S. (2006). A low density for Binary Kuiper Belt Object (26308) 1998 SM165. In *AAS/Division for Planetary Sciences Meeting Abstracts #38* (Vol. 38, p. 34.01).

Stansberry, J. A., Grundy, W. M., Mueller, M., Benecchi, S. D., Rieke, G. H., Noll, K. S., et al. (2012). Physical properties of trans-neptunian binaries (120347) Salacia-Actaea and (42355) Typhon-Echidna. *Icarus*, *219*(2), 676–688. https://doi.org/10.1016/j.icarus.2012.03.029

Thomas, P., Burns, J., Hedman, M., Helfenstein, P., Morrison, S., Tiscareno, M., & Veverka, J. (2013). The inner small satellites of Saturn: A variety of worlds. *Icarus*, *226*(1), 999–1019. https://doi.org/10.1016/j.icarus.2013.07.022

Thomas, P. C. (2000). NOTE: The shape of Triton from limb profiles. *Icarus*, *148*(2), 587–588. https://doi.org/10.1006/icar.2000.6511

Thomas, P. C., A'Hearn, M., Belton, M. J. S., Brownlee, D., Carcich, B., Hermalyn, B., et al. (2013). The nucleus of Comet 9P/Tempel 1: Shape and geology from two flybys. *Icarus*, *222*(2), 453–466. https://doi.org/10.1016/j.icarus.2012.02.037

Thomas, P. C., A'Hearn, M. F., Veverka, J., Belton, M. J. S., Kissel, J., Klaasen, K. P., et al. (2013). Shape, density, and geology of the nucleus of Comet 103P/Hartley 2. *Icarus*, *222*(2), 550–558. https://doi.org/10.1016/j.icarus.2012.05.034

Thomas, P. C., Armstrong, J. W., Asmar, S. W., Burns, J. A., Denk, T., Giese, B., et al. (2007). Hyperion's sponge-like appearance. *Nature*, *448*(7149), 50–56. https://doi.org/10.1038/nature05779

Thomas, P. C., Tiscareno, M. S., & Helfenstein, P. (2019). The inner small satellites of Saturn and hyperion. In P. M. Schenk, R. N. Clark, C. J. A. Howett, A. J. Verbiscer, & J. H. Waite (Eds.), *Enceladus and the icy moons of saturn* (pp. 387–408). The University of Arizona Press.

Thomas, P. C., Veverka, J., Belton, M. J. S., Hidy, A., A'Hearn, M. F., Farnham, T. L., et al. (2007). The shape, topography, and geology of Tempel 1 from Deep Impact observations. *Icarus*, *187*(1), 4–15. https://doi.org/10.1016/j.icarus.2006.12.013

Vilenius, E., Kiss, C., Müller, T., Mommert, M., Santos-Sanz, P., Pál, A., et al. (2014). "TNOs are Cool": A survey of the trans-Neptunian region. X. Analysis of classical Kuiper Belt Objects from Herschel and spitzer observations. *Astronomy and Astrophysics*, *564*, A35. https://doi.org/10.1051/0004-6361/201322416